



**PHOTON SIEVE BANDWIDTH BROADENING BY REDUCTION OF
CHROMATIC ABERRATION EFFECTS USING SECOND-STAGE
DIFFRACTIVE OPTICS**

THESIS

Christopher M. Tulip, Major, USAF

AFIT-ENP-MS-15-M-086

**DEPARTMENT OF THE AIR FORCE
AIR UNIVERSITY
AIR FORCE INSTITUTE OF TECHNOLOGY**

Wright-Patterson Air Force Base, Ohio

DISTRIBUTION STATEMENT A.
APPROVED FOR PUBLIC RELEASE; DISTRIBUTION UNLIMITED.

The views expressed in this thesis are those of the author and do not reflect the official policy or position of the United States Air Force, Department of Defense, or the United States Government. This material is declared a work of the U.S. Government and is not subject to copyright protection in the United States.

AFIT-ENP-MS-15-M-086

PHOTON SIEVE BANDWIDTH BROADENING BY REDUCTION OF CHROMATIC
ABERRATION EFFECTS USING SECOND-STAGE DIFFRACTIVE OPTICS

THESIS

Presented to the Faculty

Department of Engineering Physics

Graduate School of Engineering and Management

Air Force Institute of Technology

Air University

Air Education and Training Command

In Partial Fulfillment of the Requirements for the

Degree of Master of Science in Applied Physics

Christopher M. Tulip

Major, USAF

March 2015

DISTRIBUTION STATEMENT A.

APPROVED FOR PUBLIC RELEASE; DISTRIBUTION UNLIMITED.

AFIT-ENP-MS-15-M-086

PHOTON SIEVE BANDWIDTH BROADENING BY REDUCTION OF CHROMATIC
ABERRATION EFFECTS USING SECOND-STAGE DIFFRACTIVE OPTICS

Christopher M. Tulip
Major, USAF

Committee Membership:

Lt Col Anthony L. Franz, PhD
Chair

Dr. Michael A. Marciniak
Member

Dr. Michael R. Hawks
Member

Dr. Geoff P. Andersen
Member

Abstract

A photon sieve is a lightweight diffractive optic which can be useful for space-based imaging applications. It is limited by chromatic aberration and a narrow bandwidth. A Fresnel zone plate is used to counteract this effect in a manner similar to that accomplished with a traditional holographic corrector.

First, a radiometric analysis established a target for bandwidth improvement. Next, a sieve was designed, fabricated, and characterized. Third, the bandwidth-broadening correction scheme was developed to correct primary chromatic aberration. Finally, a zone plate was designed, fabricated, and tested. Performance of the corrected system was measured over the target bandwidth.

The corrected system resolved the “3-1” group of a resolution target at the primary wavelength and across an 8-nm bandwidth. The uncorrected system resolved the smaller “6-5” group at the primary wavelength but resolved the “3-1” group over only a 2-nm range. The lower resolution of the corrected system at the primary wavelength is suspected to be a result of corrector design flaws which allowed only the central 2-4 mm to be used. When accounting for this reduced diameter, resolving the “3-1” group does indicate nearly diffraction-limited performance over a bandwidth four times greater than the uncorrected system at the same resolution. This result suggests correction is occurring. A redesign of the corrector may increase performance relative to the primary.

AFIT-ENP-MS-15-M-086

To my loving wife.

Acknowledgments

I would like to thank my advisor Lieutenant Colonel Anthony Franz. He not only provided my foundation for understanding the discipline of optics but also guided me through this project. I would also like to thank my sponsor, Dr. Matthew G. McHarg from the Space Physics and Atmospheric Research Center, United States Air Force Academy, as well as the other members of the Academy team that offered support to this research. In particular, I would like to offer appreciation to Dr. Geoff Andersen from the Laser and Optics Research Center who spent a week personally demonstrating his experimental techniques relevant to my research and helping me characterize my photon sieve. He also provided MATLAB and Zemax guidance and examples for which I am grateful.

Additionally, I would like to thank the members of my committee. Dr. Michael Marciniak reviewed my radiometric analysis and invested time last summer helping me understand the principles of the laser used in my research. Dr. Michael Hawks provided me a working Zemax key (without which I could not have completed my work) and helped me understand the intricacies of MATLAB necessary for my project. Finally, without the assistance, guidance, ingenuity, and creativity of Greg Smith and Mike Ranft, I would not have been able to complete any of my experimental work. Thank you to all who helped and supported me throughout this endeavor.

Christopher M. Tulip

Table of Contents

	Page
Abstract	iv
Acknowledgments.....	vi
List of Figures	x
List of Tables	xiii
I. Introduction	1
Problem Overview.....	1
Photon Sieve Chromatic Aberration.	1
Bandwidth Broadening.	3
Motivation and Implications.....	4
FalconSAT-7.....	4
Secondary Optics.	5
Objectives and Hypothesis	6
Scope and Limitations	7
Thesis Structure and Preview	8
II. Background and Relevant Research.....	9
Diffractive Optics	9
Diffractive Optics Overview.....	9
Diffractive Optics Benefit.....	10
FZP Theory.....	10
FZP Concept.	10
FZP Benefit.....	12
Photon Sieve Theory	13
Fresnel Zone Position.....	14
Fresnel Zone Size.....	16
Photon Sieve Field Theory.....	17
Photon Sieve Hole Size.....	18
Photon Sieve Benefit.....	21
Chromatic Aberration.....	22
Traditional Optics.	22
Diffractive Optics.....	23
Measurement.....	23
Aberration Correction.....	25
Traditional Method.	25
Diffractive Optics Methods.....	26

	Page
Holograms	27
Traditional Holograms.	27
Computer-Generated Holograms.	28
Binary Holograms.	28
FZP or Photon Sieve as a Hologram.	28
Chapter Summary	30
III. Methodology	31
Radiometry	31
USAFA Analysis.	31
Notional Bandwidth Analysis.	32
Design.....	37
Primary.....	37
Secondary.....	44
Considerations and Assumptions.....	44
Zemax Modeling.....	45
Correction Scheme Design.	47
Wavelength Adjustment.	48
Primary and Secondary Characterization	50
Setup.....	50
Focal Spot.	51
Imaging.	53
Interferometry.	54
Correction Effectiveness	55
Chapter Summary	56
IV. Results and Analysis.....	57
Primary Modeling Predictions.....	57
Focal Spot.	57
Chromatic Aberration.	59
Wavefront Error.	60
Primary Experimental Results	61
Focal Spot and Chromatic Aberration.	61
Imaging.	66
Interferometry (Wavefront Error).	70
Efficiency.....	71
Zemax Modeling and Optimization.....	71
Optimization.....	71
Design Comparisons.	72
Final System Design.	74
Secondary Modeling Predictions.....	75

	Page
Wavefront Error.....	75
Focal Spot and Chromatic Aberration.....	77
Secondary Experimental Results.....	79
Zone Plate Characterization.....	79
Corrected Focal Spot and Chromatic Aberration.....	82
Chapter Summary.....	90
V. Conclusion.....	91
Conclusion.....	91
Future Work and Action.....	93
Appendix.....	95
Radiometry MATLAB Code.....	95
Primary Photon Sieve Design MATLAB Code.....	99
High Precision Primary Photon Sieve Design MATLAB Code.....	100
Secondary/Corrector Photon Sieve Design MATLAB Code.....	104
Fresnel Zone Plate Design MATLAB Code.....	107
Sample Gerber Format Photon Sieve Code.....	110
Sample Gerber Format Zone Plate Code.....	111
Sample Zemax Photon Sieve Modeling Code.....	112
ACA Error Propagation Analysis.....	115
Bibliography.....	119

List of Figures

Figure	Page
1. Chromatic Aberration in Imaging..	2
2. Chromatic Aberration Bandwidth Limitations..	3
3. FalconSAT-7 Rendering..	4
4. FZP Zone Geometry..	11
5. Fresnel Zone Plate Rendering..	12
6. FZP Positive and Negative Diffraction Orders..	13
7. Microscopic Image of Photon Sieve Center..	14
8. Fresnel Zone Position Geometry..	15
9. Fresnel Zone Size Geometry.....	16
10. Photon Sieve Efficiency.....	19
11. Hole-Zone Width Comparison.....	19
12. Variation of Field Amplitude as a Function of d/w ..	20
13. Chromatic Aberration.	22
14. Wavelength-Dependent Focal Distance Changes..	24
15. Hologram Recording Geometry.....	27
16. Hologram Modeled by Interference Pattern.	29
17. Radiometric Analysis Geometry.....	32
18. SNR-Bandwidth Correlation.....	36
19. SNR-Bandwidth Correlation across Design Options.....	36
20. Ti:Sapphire Output Power..	38

Figure	Page
21. Radial Hole Spacing..	39
22. Lateral Hole Spacing.....	41
23. Primary Photon Sieve Image..	43
24. Profilometer Images of Photon Sieve Center.....	43
25. Primary Photon Sieve Ray Fan..	45
26. Hologram Geometry..	46
27. Corrected System Ray Fan.....	47
28. Lab Setup for Focal Spot and Imaging Analysis..	51
29. Resolution Chart Image.	53
30. Lab Setup for Interference Pattern Analysis.....	54
31. Off-Wavelength Interferogram.	55
32. Lab Setup with Corrector.....	56
33. Polychromatic Primary Sieve Focal Spot Prediction.....	58
34. Corrected Focal Spot.....	59
35. Primary Wavefront Depiction Prediction at Various Wavelengths.	60
36. Plot of Measured versus Predicted ACA.	62
37. Difference in Measured versus Predicted ACA.....	63
38. Polychromatic Focal Spot Distortion.....	63
39. In-focus Spot Measurement..	65
40. Primary Photon Sieve Spot Image at 731 nm.	66
41. Diffraction-Limited Image of Resolution Chart from Primary Sieve.....	67
42. Image of Resolution Chart with and without Diffuser.....	67

Figure	Page
43. Comparative ACA Measurement.....	69
44. Interferogram of Primary Sieve with a Reference Beam.....	70
45. Corrected Wavefront Depiction at Various Wavelengths.. ..	76
46. Along-Axis Corrected Focal Spot Predictions.....	78
47. Corrector A-FZP Focal Spot.....	79
48. Corrector A-FZP Resolution Chart.....	80
49. Corrector A-FZP Spot Measurement.. ..	81
50. Corrected Focal Spot Location.. ..	83
51. Corrected Spot.. ..	85
52. Corrected Spot Characteristics.....	86
53. Corrected Spot Wavelength Variation.	86
54. Aperture Adjustments to Corrected Image.	87
55. Corrected 3 Comparison.	88
56. Corrected Line Group Comparison.....	88
57. Diffuser Influence on Bandwidth.....	90
58. Zemax Photon Sieve Code.....	114
59. Zemax Corrected System Code.	115

List of Tables

Table	Page
1. Primary Photon Sieve Characteristics.....	42
2. Primary Photon Sieve Chromatic Aberration Focal Spot Measurements.....	61
3. Resolution Chart Data.....	68
4. Primary Photon Sieve Chromatic Aberration Resolution Chart Measurements.....	69
5. Optimized Design Parameters.....	73
6. Corrector Element Comparison	74
7. Predicted Peak-to-Valley Wavefront Error	76
8. Predicted Change in Image Location	78
9. Expected Focal Spot Locations.....	84

PHOTON SIEVE BANDWIDTH BROADENING BY REDUCTION OF CHROMATIC ABERRATION EFFECTS USING SECOND-STAGE DIFFRACTIVE OPTICS

I. Introduction

One major difficulty with polychromatic imaging is wavelength-dependent aberration caused by the optical system. In general, this problem (known as chromatic aberration) is observed when individual colors of a polychromatic light source are independently focused at different locations. Dissimilar optical elements may exhibit differing amounts of this effect. Diffractive optics, for instance, are known to have much greater focus variation than traditional optics (30:76). Common to both traditional and diffractive elements, however, is the necessity to consider this aberration in order to achieve effective imaging. The purpose of this thesis is to address the problem of chromatic aberration that specifically affects photon sieve-based imaging systems and then subsequently to investigate corrective techniques for improving polychromatic applications of these devices. This chapter provides a synopsis of the problem, the research objectives, and expectations.

Problem Overview

Photon Sieve Chromatic Aberration.

A device particularly affected by chromatic aberration is the photon sieve, a diffractive optic that forms an image using the same physical principles as a Fresnel Zone

Plate (FZP). The theory behind this element will be detailed in a subsequent section; however, the main focus of this research can be highlighted by referencing the expression for the focal length of a photon sieve in the paraxial region (1:2976):

$$f = \frac{R_n^2}{2n\lambda}. \quad (1)$$

R_n and n are parameters of the sieve discussed later, but it is clear that the focus varies inversely with respect to the wavelength (λ) of the incident light. A polychromatic source, therefore, will result in chromatic aberration while using this optic (21:496). To illustrate this problem, Fig. 1 depicts magnified images of the number “3” formed at 740 nm, 741 nm, and 744 nm by a photon sieve. Because the sieve was designed to operate at 740 nm, the image formed at this wavelength (Fig. 1, Left) is clear and sharp. As the laser was tuned away from the design wavelength, however, the image quality degraded significantly over only a short bandwidth. Consequently, a sieve used as a primary optic would require substantial correction to be effective in polychromatic imaging.

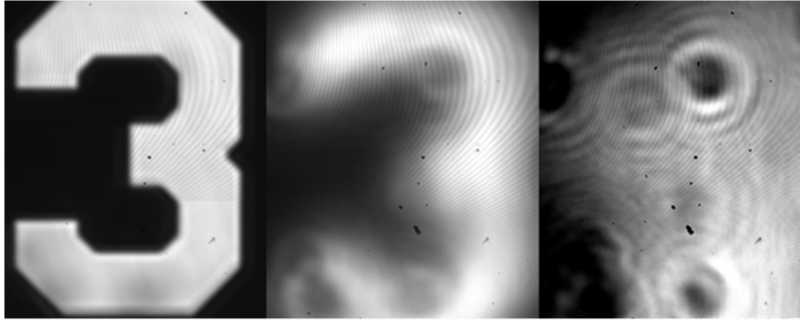


Figure 1. Chromatic Aberration in Imaging. The three images were formed using a 10-cm diameter photon sieve at 740 nm, 741 nm, and 744 nm (left to right). A 20x microscope objective was used to magnify the image from the 740-nm focal plane onto the camera. As the laser was tuned, the image blurred and is unrecognizable only 4 nm from the design wavelength. Another way of viewing the result is to note that the longitudinal position of best focus shifted as the laser was tuned.

Bandwidth Broadening.

One possible method to mitigate the problem of chromatic aberration is to use a filter to limit the bandwidth incident on an optical system. This procedure essentially forces the source to be monochromatic and thus may prevent the effects of chromatic aberration. Andersen and Tullson note that the diffraction-limited “useable bandwidth” ($\Delta\lambda$) of a photon sieve without correction is given by

$$\Delta\lambda \approx \frac{2\lambda^2 f}{D^2}, \quad (2)$$

where f is the focal length of the optic and D is the diameter (5:5). For the particular case of the primary sieve used in this thesis, $\Delta\lambda = 0.055$ nm, indicating that it is effective over an extremely small range on either side of the design wavelength. Thus, in order for a clear image to be produced, the incident light would need to be narrowly filtered to this value. Fig. 2 illustrates the effect of sieve bandwidth limitations. The pictured line group was focused at 740 nm (Left), and the laser was tuned until the features were barely resolvable (Right). Eq. 2 gives the bandwidth required to maintain less than 0.25 waves of error. The bars pictured in Fig. 2 are large enough that exceeding this error does not result in failure to resolve the features. In other words, the effective bandwidth obtained from Fig. 2 represents a much higher error tolerance (approximately 11 waves of aberration) than does that given by Eq. 2 and is therefore much larger than 0.055 nm.

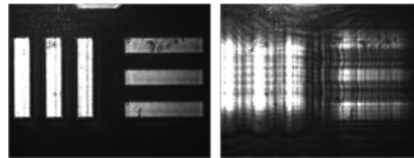


Figure 2. Chromatic Aberration Bandwidth Limitations. Left: The 3-1 line grouping from a Negative USAF 1951 Test Target at 740 nm was imaged by the sieve. Right: The same group was imaged at approximately 742.5 nm. The laser was tuned from 740 nm until the lines were barely resolvable, illustrating a ± 2.5 -nm bandwidth limit for this group (35:3). These images were formed without a diffuser.

While the application of a filter offers a useable solution under certain conditions, the technique does little to enhance the ability to effectively image multiple colors simultaneously. Furthermore, the method also restricts the collected energy. When using a camera to record an image, filtering most of the incident light necessitates a higher integration time in order to gather enough energy for an image. If the optical system is in motion, this longer time can subsequently produce a smeared picture. In other words, a narrow bandwidth not only prevents polychromatic imaging but may also cause distortion during monochromatic imaging (17).

Motivation and Implications

FalconSAT-7.

This thesis research is in conjunction with a space-based imaging project (FalconSAT-7) currently being pursued by the United States Air Force Academy (USAFA). As depicted in Fig. 3, the satellite uses a photon sieve as the primary optical element. The current system filters incident light to a narrow bandwidth limit of 0.01 nm, effectively making the source monochromatic at 656.45 nm (9:5-7).

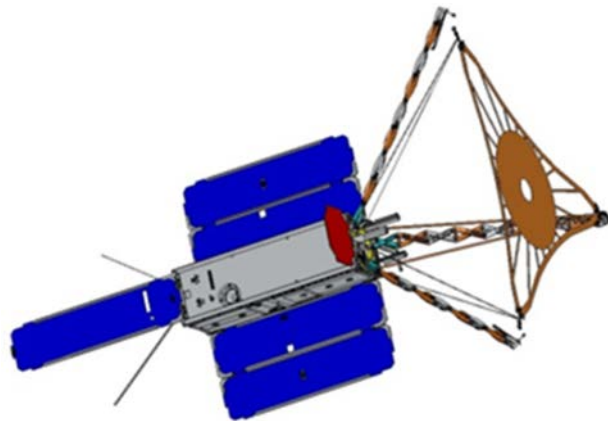


Figure 3. FalconSAT-7 Rendering. The photon sieve is the circular membrane in the center of the retractable arms. Figure used with permission (31).

FalconSAT-7 is designed to test the imaging potential of a novel optical system while viewing the Sun at a highly-specific wavelength (9:1). If successful, this concept could be employed in future satellite design schemes, especially due to its reduced size (the main aperture can be folded) and smaller-mass optical components (the sieve is a lightweight membrane) (9:1). In order to broaden its usefulness, however, the bandwidth limitations would almost certainly need to be relaxed to allow polychromatic imaging of additional sources. This requirement leads to the need for inclusion of corrective optical components to compensate and remove chromatic aberration effects. This thesis examines methods to enable possible future variations of the FalconSAT system to image a broader wavelength with acceptable image quality.

Secondary Optics.

As part of her graduate thesis, United States Air Force (USAF) Captain Sarah Myers explored methods for correcting chromatic aberration in the FalconSAT system by redesigning the photon sieve itself (primary optic). Her results showed some benefit to this technique but pointed toward a focus on adjusting the secondary components to enhance imaging (29:93). The use of a corrector hologram has already been shown to effectively reduce chromatic aberration issues and increase bandwidth in similar systems (4, 22). According to the USAFA, however, the current FalconSAT-7 design is too small to include diffractive optics as part of a bandwidth-broadening scheme (9:6). Because system size is not a primary consideration in this thesis, the efforts to correct chromatic aberration using holography are continued, specifically by employing a FZP or second photon sieve as a holographic-style corrector element.

Objectives and Hypothesis

As previously noted, the main goal of this project is to determine a manner by which to widen the useable bandwidth of a photon sieve imaging system. Achieving this target will both improve data collection (through production of polychromatic images) and also increase the energy gathered during a shorter time period, reducing distortion from satellite motion. This overarching goal can be divided into four distinct objectives:

1. Determine a target bandwidth through radiometric analysis of a typical system;
2. Demonstrate and measure chromatic aberration effects of a photon sieve primary optical element;
3. Develop a secondary system designed to correct chromatic aberration unique to this particular primary element over the target bandwidth; and
4. Demonstrate the possibility of diffraction-limited performance (less than 0.25 waves peak-to-valley wavefront aberration) of the primary sieve over this improved bandwidth while using the secondary corrector (39:26).

Based on previous research detailed in Chapter II, as well as discussions with the USAFA personnel directing the FalconSAT-7 project, it is expected that a holographic-style optic will sufficiently correct the wavefront error to within the diffraction limit over at least the requisite target bandwidth (2). The equivalence of a FZP to a traditional hologram will be noted in the next chapter, and because the FZP structure is the foundation of a photon sieve, it is hypothesized that either a FZP or a second sieve can be used to adequately expand the bandwidth of the primary optic.

Scope and Limitations

This research does not directly investigate the merits and usefulness of the photon sieve as the main imaging element. Also, as already noted, it does not address methods to decrease the aberration by altering the design of the sieve itself (see Ref. 29 for an example of primary sieve modification). The focus is limited to determining a way to utilize second-stage optics to correct the aberration introduced by the primary element. Furthermore, at the direction of the USAFA, this project does not attempt to meet size requirements or other engineering design constraints but rather focuses solely on demonstrating the physical possibility of increasing the system bandwidth in this manner.

Lastly, when determining the target bandwidth (see Chapter III), any energy losses due to the use of a secondary corrector were neglected. In other words, while introduction of a second diffractive optics would undoubtedly decrease the energy incident on the camera (thereby necessitating a larger starting bandwidth), this energy decrease was not considered for several reasons. First, the radiometric analysis requested by the USAFA was for a notional system design and not the particular system used in this thesis. In other words, even if a second element was considered in the analysis, the results would not be directly transferrable to this experiment. Furthermore, the goal of this thesis is to serve as a “proof of concept” for correcting chromatic aberration using a FZP (or second sieve by extension) and consequently needs only to demonstrate possible effectiveness. Third, the target bandwidth given by the radiometric analysis represents the size (order-of-magnitude) of the bandwidth needed to effectively image using this type of system. In essence, it provides a good approximation of the wavelength range

required and therefore a good research target. Lastly, it will be shown in Chapter IV that once a basic corrector design scheme is adopted, simply changing parameters of this template results in an increase or decrease in system bandwidth. In this way, if it is later determined that too much energy is lost because of the corrector optic, the final design can simply be altered slightly to gather more energy while the fundamental design scheme remains the same.

Thesis Structure and Preview

The following portion of the thesis is organized into three major sections and concluding remarks. First, necessary background and previous research is highlighted. Specifically, the development of photon sieve theory from underlying diffractive optic and FZP concepts will be described. Information concerning chromatic aberration effects in traditional and diffractive imaging systems, typical corrective methods, and aberration correction through holography is also included in this section. Second, the paper will cover the basic methods used in the project, including a radiometric analysis, sieve and corrector design approaches, and experimental setup. Finally, theoretical and experimental results will be discussed in relation to both characterization of the primary sieve and also evaluation of corrector effectiveness.

II. Background and Relevant Research

This chapter reviews the essential concepts necessary to understand the methods and techniques employed in this thesis. Specifically, the advancement of photon sieve theory from basic diffractive optics theory will be tracked. Benefits at each stage of progression will be considered. Additionally, this chapter explores the problem of chromatic aberration in greater detail as well as current methods being employed to compensate for this issue. In particular, the principles of holography relevant to aberration correction will be investigated.

Diffractive Optics

Diffractive Optics Overview.

As with all optics, the use of diffractive elements primarily involves wavefront manipulation (30:1). Optical devices may be constructed such that they adjust portions of an incident wavefront (through a phase or amplitude change) as needed to achieve a desired result (30:1-2). This effect is easy to observe in the design of certain diffractive optics in particular. For example, a FZP (which will be discussed shortly) blocks portions of a wavefront in a calculated way that results in focusing of the transmitted light. Wavefront error analysis is employed heavily in this thesis as the primary method of measuring system aberration and correction effectiveness. Traditional geometric ray analysis is also occasionally considered for purposes such as configuration design (in Zemax) and determining expected locations of images throughout the optical system

(30:2). Zone plates, photon sieves, and holograms (to include binary, computer-generated holograms) are all considered diffractive optics (30:2).

Diffractive Optics Benefit.

Diffractive optics offer several advantages over traditional lenses. First, high dispersion is a property of diffractive optics that can be leveraged when used to counteract oppositely-oriented dispersion elsewhere in a system. Greater effort may be required to achieve the same net dispersion with traditional optic combinations (30:76). Diffractive optics can also be small, providing size and weight benefit (7:1427). Lastly, they can be flat, making them easier to employ in certain applications, such as space-based imaging where three-dimensional optics are more challenging to set up (1:2976; 5:1; 9:1).

FZP Theory

FZP Concept.

Simply stated, the basic concept of a FZP is to use a binary structure of opaque and transparent rings to transmit light that will interfere constructively at the focus while blocking light that interferes destructively (34:294). To understand how the device operates, Fig. 4 depicts a wavefront segmented into a similar set of transparent and opaque rings (30:9).

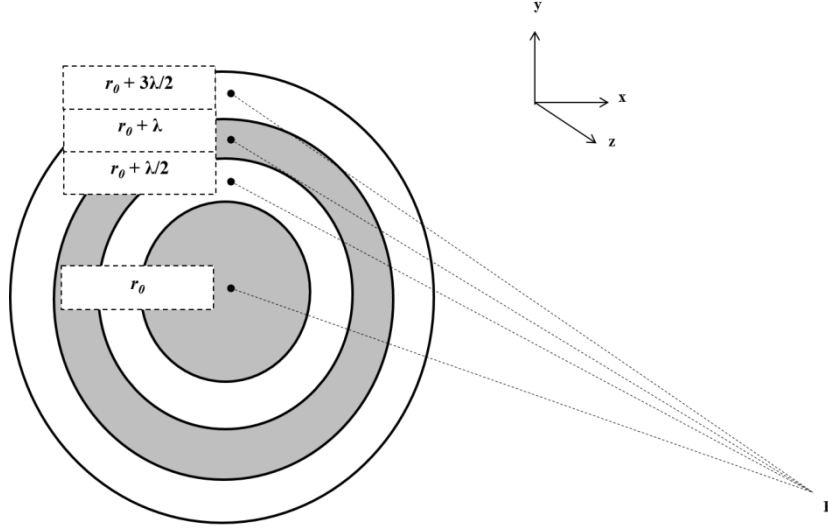


Figure 4. FZP Zone Geometry. The diagram, adapted from Ref. 30, illustrates a two-dimensional depiction of a spherical wavefront divided into alternating opaque (gray) and clear (white) rings. The ring edges correspond to a $\lambda/2$ increase in distance from an observation point (P) normal to the wavefront.

The rings (called Fresnel zones) may be considered part of a two-dimensional spherical wavefront divided into regions such that the distance from each zone edge to an observation point (P) is $\lambda/2$ greater than the distance from the preceding zone's edge (30:9). The Huygens-Fresnel principle states that each point on a wavefront radiates secondary wavelets which propagate (causing a phase change) and then interact with each other (21:444). As such, each ring in Fig. 4 will be the source of secondary wavelets which start in-phase but later interfere at P with new phase values (34:394; 21:486-487).

The phase change of a wave is given by

$$\delta = k \cdot \Delta\text{OPL} = \frac{2\pi}{\lambda} \cdot \Delta\text{OPL} \quad (3)$$

and is a function of wavenumber, k , and the difference in optical path length (ΔOPL) (21:283). Because the OPL (distance from the wavefront to the observation point) changes from one ring to the next, the phase of the secondary wavelets at the observation point will be varied. In Fig. 4, ΔOPL from one zone to the next is $\lambda/2$, and the resultant

phase change is π , suggesting that light from one zone is out-of-phase with light from an adjacent zone.

Consider that a wavelet from the axial position can be represented with the expression $Ae^{i\varphi}$, where φ is the phase of a wave and A is the amplitude. A wavelet from the adjacent (first off-axis) zone (with $\delta = \pi$) will be given by $Ae^{i\varphi+\pi} = -Ae^{i\varphi}$. The amplitude of the off-axis wavelet is opposite the original wave and thus cancels (21:487-488, 495).

Conversely, skipping a zone results in a change in OPL of λ such that $\delta = 2\pi$, indicating that light from one zone is in-phase with light from a zone two rings away. Allowing transmission from every other ring consequently results in constructive interference from the in-phase light. Fig. 5 depicts the central 2 mm of a 3-cm FZP.

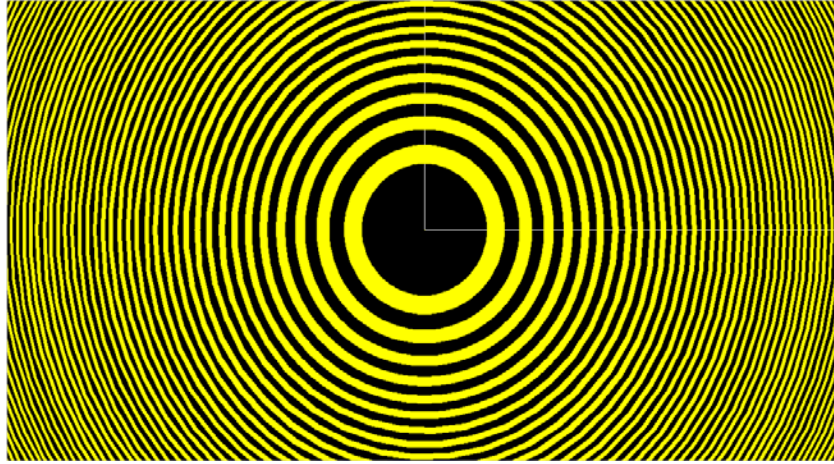


Figure 5. Fresnel Zone Plate Rendering. The central 2 mm of a 30-mm FZP is depicted. The plate has a designed focal length of 23 mm.

FZP Benefit.

A FZP has the same advantages as other diffractive optics in that energy is gathered, focused, and intensified as with a lens; however, the device can be much lighter and compact. Additionally, another benefit of a FZP that will be discussed in detail later

is that it can be constructed to behave physically like a hologram which, as will be shown, may lend itself to practical application (36:591). Fig. 6 illustrates a final possible benefit to using a FZP (21: 497). Light incident on a FZP results in both positive (converging wave) and negative (diverging wave) diffraction orders (21:496-497). As will be demonstrated later, the particular system designed to reduce chromatic aberration in this experiment employs each of these orders independently for different purposes, indicating flexibility of the device.

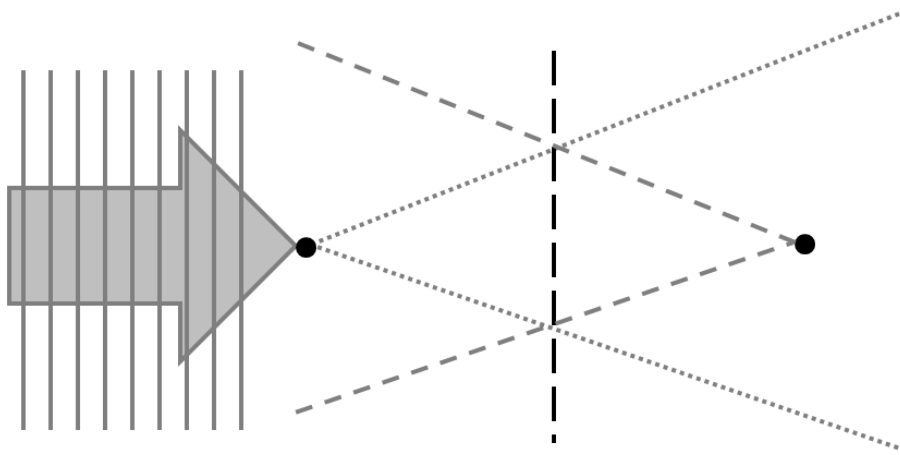


Figure 6. FZP Positive and Negative Diffraction Orders. The diagram is adapted from Ref. 21 and shows both a diverging wave (negative diffraction) and a converging wave (positive diffraction) from a FZP. An incident plane wave is converged by the FZP to form a real image. The FZP also causes divergent light such that a negative virtual image is produced behind the optic.

Photon Sieve Theory

A photon sieve essentially operates via the same principles as a FZP (1:2976). Rather than using opaque rings to block the light from various zones, a sieve employs holes in a ring pattern to allow light to pass through (1:2976). Fig. 7 is a microscopic image of the interior rings of an actual photon sieve.

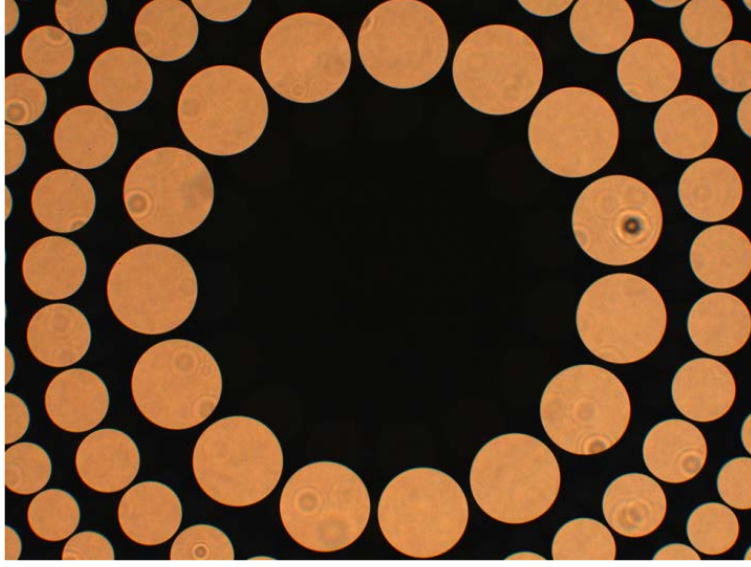


Figure 7. Microscopic Image of Photon Sieve Center. The circular areas on this 10-cm diameter, $f = 0.5$ m photon sieve are clear apertures on a chrome-coated quartz plate.

Fresnel Zone Position.

The radial position of a hole is unique to each ring and is centered on an underlying Fresnel zone. This position can be determined geometrically and by using linear superposition field theory. The geometric approach will be discussed first (21:495-496; 23:185; 34:394). Fig. 8 depicts light originating from an axial point a distance ρ_0 to the left of a photon sieve and traveling through the sieve to another axial point r_0 to the right of the sieve (21:496). For the light to focus (interfere constructively) at r_0 , all of the secondary wavelets from the original wavefront arriving at this point must exhibit a $2\pi n$ phase shift, where n is an integer. Note that only one ray is depicted. As described in the previous section, a $2\pi n$ phase shift corresponds to a change in OPL of $n\lambda$. Referring to Fig. 8, this condition is equivalent to the statement,

$$\Delta\text{OPL} = n\lambda = (\rho_n + r_n) - (\rho_0 + r_0) . \quad (4)$$

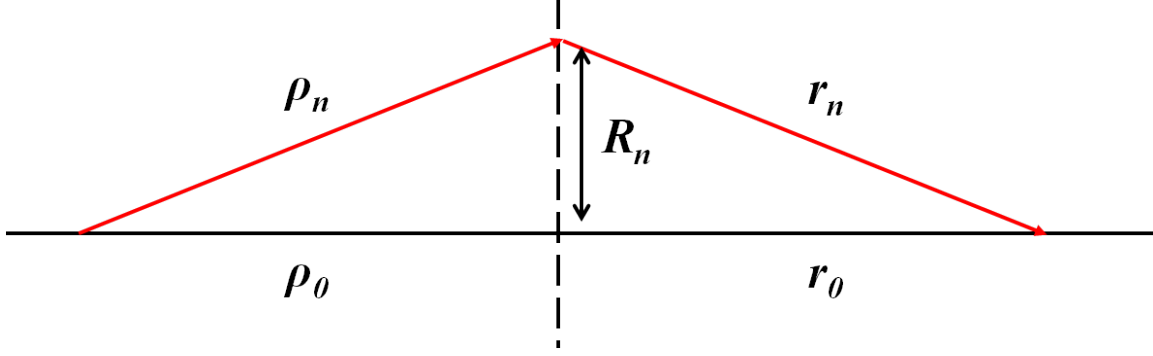


Figure 8. Fresnel Zone Position Geometry. Light travels from a point source through the photon sieve holes to an image plane. The point will be in-focus (first order) in the image plane at the location where all of the wavelets which passed through the sieve interfere constructively. The figure is adapted from Ref. 21.

When the sieve is illuminated with a plane wave, $\rho_0 = \rho_n = \infty$, and the only difference in path length comes from the post-sieve travel such that $r_n = r_0 + n\lambda$, (see Eq. 4). Note that $r_0 = f$ for infinite-conjugate imaging and that

$$r_n = \sqrt{R_n^2 + r_0^2} \quad (5)$$

by the Pythagorean theorem. An expression for the position of the n th ring (R_n) in terms of n , λ , and f can be derived:

$$R_n^2 = 2n\lambda f + n^2\lambda^2 \approx 2n\lambda f. \quad (6)$$

The same type of argument can be applied if the sieve is illuminated by a point source (as is the case in this experiment). In this situation, however, $\rho_0 = r_0 = 2f$ for one-to-one (referring to magnification size) imaging, and the change in path length, $n\lambda$, receives equal contributions from travel on both sides of the sieve:

$$\rho_n = \rho_0 + \frac{n\lambda}{2} \quad r_n = r_0 + \frac{n\lambda}{2}. \quad (7)$$

Combining Eqs. 5 and 7 again yields an expression for the center of each ring which is approximately the same as that for a sieve illuminated by a plane wave:

$$R_n^2 = 2n\lambda f + \frac{n^2\lambda^2}{4} \approx 2n\lambda f. \quad (8)$$

Fresnel Zone Size.

As is the case with the radial location, the size of each zone can also be determined geometrically. It has already been noted that the path length difference between the top and bottom of a zone to an observation point must be $\lambda/2$ (12:2389).

Referring to Fig. 9, Eq. 4 can be rewritten as

$$\Delta\text{OPL} = \frac{\lambda}{2} = (\rho_{n+} + r_{n+}) - (\rho_{n-} + r_{n-}), \quad (9)$$

where the subscripts $n+$ and $n-$ refer to the top and bottom edges of the n th zone, respectively.

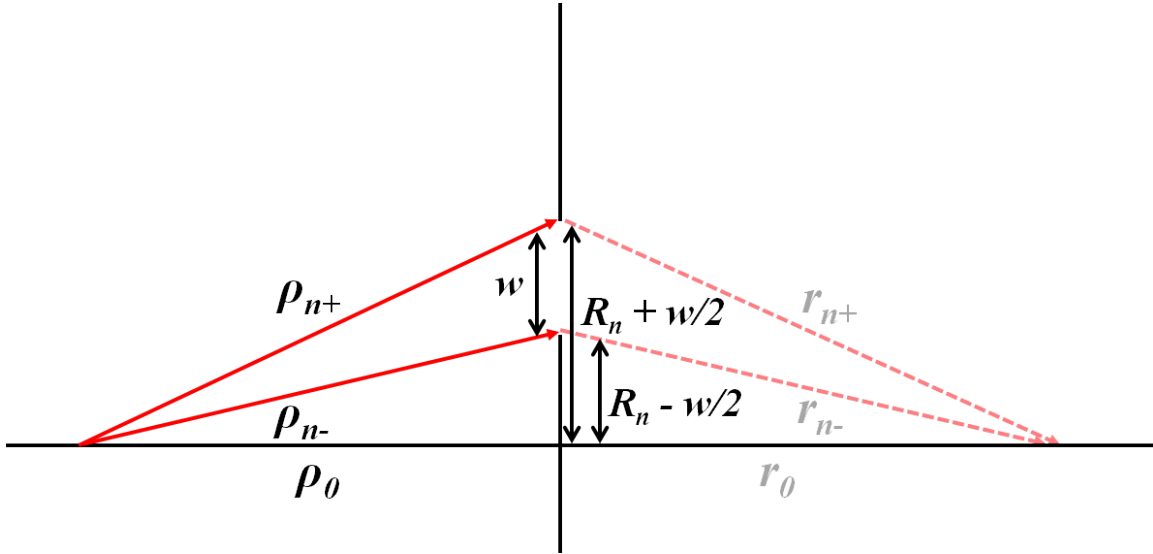


Figure 9. Fresnel Zone Size Geometry. Note that the right side geometry is subdued for clarity in the figure but is equally important when considering the zone size. w is the size of a Fresnel zone.

Once again applying the Pythagorean theorem, and additionally defining w as the width of a Fresnel zone,

$$\begin{aligned}\rho_{n+} &= \sqrt{\rho_0^2 + \left(R_n + \frac{w}{2}\right)^2} \\ \rho_{n-} &= \sqrt{\rho_0^2 + \left(R_n - \frac{w}{2}\right)^2},\end{aligned}\tag{10}$$

with similar expressions for r_{n+} and r_{n-} . Series expansions can be applied to each term

($\rho_{n-} \approx \rho_0 + \frac{1}{2\rho_0}\left(R_n - \frac{w}{2}\right)^2 + \dots$) (12:2389). Substituting the expanded versions of

Eq. 10 into Eq. 9 yields the desired expression for the width of a Fresnel zone:

$$w = \frac{\lambda f}{2R_n}.\tag{11}$$

The sieve holes are placed on top of these zones. Selecting the size of the hole such that as much of this underlying zone as possible is transmitted requires diffraction theory and is the subject of the next section.

Photon Sieve Field Theory.

Cao and Jahns present another method for obtaining the radial positions of the zones and also the sizes of the holes. Their method is based on diffracted field analysis and is both more general and more complicated. The highlights of their argument will be discussed; for a comprehensive review, see Refs. 10-12. The derivation begins by defining the field at the focus as the sum of the fields diffracted by each individual hole,

$$U_{FOCUS} = \sum_{n=1}^N U_n,\tag{12}$$

where N represents the total number of holes and n identifies the particular hole

(12:2387). Next, they apply the Fresnel diffraction integral to determine the individual

diffracted fields (U_n) that propagate from each hole to the focal plane:

$$U_n = \frac{1}{\lambda f} \iint_{-\infty}^{\infty} V_n(x, y) \exp \left[jk \frac{(X - x)^2 + (Y - y)^2}{2f} \right] dx dy. \quad (13)$$

The uppercase coordinates (X, Y) represent the focal plane, the lowercase coordinates (x, y) represent the sieve plane, the term V_n is an amplitude term dependent on the wave incident on the sieve, and they have neglected a phase factor in the expression which should vanish when converting to an intensity distribution (12:2387). Applying several coordinate transforms and approximations, they simplify Eq. 13 to an expression for the axial image-plane field of an individual hole under point-source illumination:

$$U_n(0, 0) = 2A_n N_f \exp \left[jk \left(\frac{R_n^2}{2f} \right) \right] J_{inc} \left[\frac{k \left(\frac{d}{2} \right)}{f} R_n \right], \quad (14)$$

where d is the diameter of the hole, $N_f = \pi d^2 / 4\lambda f$ is the Fresnel number, and A_n represents an amplitude term (12:2389). The maximum field intensity ($|U_n(0, 0)|^2$) will occur physically when the hole is centered on the zone and mathematically when the individual terms of Eq. 14 are maximized (12:2389). Accordingly, the exponential term in Eq. 14 is maximized to 1 when its argument equals 2π (12:2389). Setting this argument to 2π and solving for R_n^2 again yields the first term of Eq. 8, demonstrating an alternate method to determine the radial positions of the Fresnel zones. Note that, by starting with the Fresnel diffraction integral, Cao and Jahns had already made the paraxial approximation which is why the squared term in Eq. 8 is not present in this case. The validity of this approximation in terms of this experiment is discussed in Chapter III.

Photon Sieve Hole Size.

From Fig. 10 it is evident that a ring of non-overlapping holes will not completely fill the underlying Fresnel zone, reducing transmission and overall device efficiency.

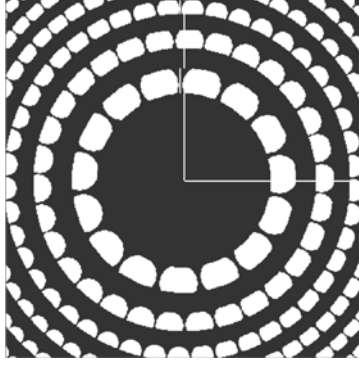


Figure 10. Photon Sieve Efficiency. A FZP is laid on top of a corresponding photon sieve. Notice that the holes do not completely fill the zones, indicating a loss of transmission efficiency between a FZP and sieve.

Analysis published by Kipp's group addresses this issue and suggests increasing underlying zone transmission by increasing the associated hole diameters such that their diameters are actually greater than the width of the zone (23). Fig. 11 illustrates this approach but also indicates that this scheme, while permitting more coverage of the transmission zones, allows light from opaque (destructive) zones through as well.

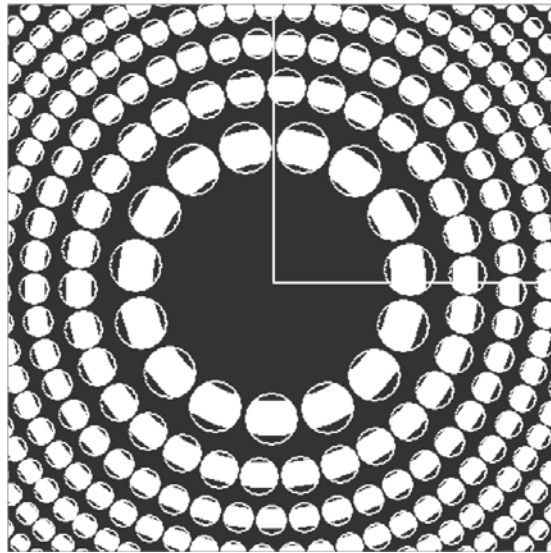


Figure 11. Hole-Zone Width Comparison. A photon sieve is laid on top of a corresponding FZP (opposite of Fig. 10). Notice that while more of the underlying zone is transmitted by expanding the hole diameter, some of the light from the "dark" (destructive) zones is also transmitted.

Kipp notes that the ratio of hole diameter to zone width (d/w) has a somewhat oscillatory effect on the focal field amplitude (23:185). As d/w is increased, the

amplitude increases to a maximum value at $d/w \approx 1.5, 3.5, 5.5$. At some point, however, enough light is passed from dark zones to completely cancel the light from the bright zones. This effect is observed at $d/w \approx 2.4, 4.4, 6.4$ (23:186). For this reason, the size of each photon sieve hole is typically (see Ref. 1:2976) set such that

$$\frac{d}{w} = 1.53, \quad (15)$$

the position of the first intensity maximum (see Fig. 12).

To understand this effect, it is necessary to revisit the Cao and Jahns analysis. Hole size information can be extracted from the *Jinc* term in Eq. 14 by combining it with Eq. 11 and noting again that $\exp\left[jk\left(\frac{R_n^2}{2f}\right)\right] = 1$ for a hole centered on the underlying zone (12:2389-2390). Their final expression,

$$U_n(0,0) \propto \frac{d}{w} J_1\left[\frac{\pi d}{2w}\right], \quad (16)$$

is plotted in Fig. 12, which clearly displays the variable nature of the field amplitude over a range of d/w values.

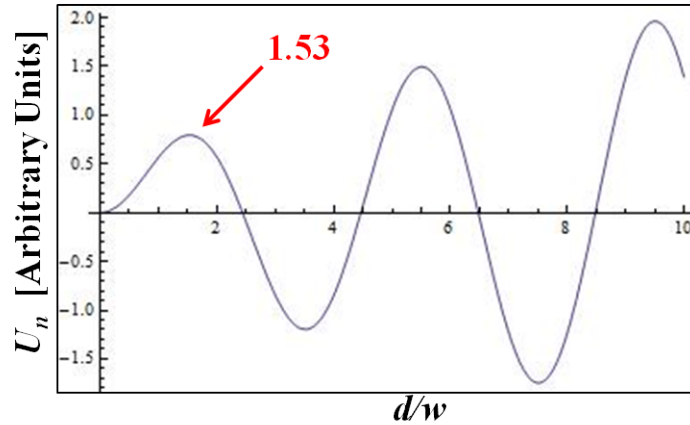


Figure 12. Variation of Field Amplitude as a Function of d/w . As the ratio of hole size to underlying zone is varied, the field amplitude in the image plane changes. The hole size can be increased beyond the underlying zone size ($d/w > 1$) with increasing amplitude until too much dark zone contribution results in a reduction of amplitude and ultimate complete cancellation of the field.

Photon Sieve Benefit.

As a diffractive optic element, the benefits over traditional optics already discussed also apply to photon sieves. Additionally, there are several unique advantages to using this particular element. First, sieves allow the control of higher diffraction orders (11:566; 23:184-185). Next, a FZP requires either a substrate or some other form of binding element to hold the separated rings together, a problem that is not an issue for a photon sieve (1:2976; 5:1). To be fair, because the rings of a photon sieve are formed by making holes that are interconnected, there is still some form of material between the transmission regions. Additionally, note that for this experiment the photon sieve was constructed by printing the hole pattern in chrome on an underlying quartz substrate. This choice was made for durability and cost reasons and need not be a limiting factor in actual sieve development (as with the FalconSAT-7 membrane sieve). In other words, an actual sieve may not require a mounting plate.

Andersen notes a third benefit of using a sieve: “Apodization is easily incorporated into a photon sieve simply by modifying the number of holes” and is useful for unique space-based missions (1:2976; 5:1). Finally, overall resolution of the optic is a factor of smallest Fresnel zone. Kipp’s group demonstrated that because the size of pinholes can be constructed smaller than rings of a FZP, it is possible to achieve better resolution with a sieve (23:184-186).

Chromatic Aberration

Traditional Optics.

The concept of chromatic aberration is most easily understood within the framework of traditional lens optics. Because the index of refraction of a material (n) can be generally defined as a function of wavelength, the focal length of a lens of this material will also be a function of wavelength according to the familiar relation

$$\frac{1}{f} = [n(\lambda) - 1] \left(\frac{1}{R_1} - \frac{1}{R_2} \right), \quad (17)$$

where R_1 and R_2 are the radii of curvature of the lens surfaces (21:268). Solving for f and substituting this variable focal length into the imaging equation from geometric optics makes it evident that the image distance (s_i) will also be varied for different wavelength values:

$$s_i = \frac{s_o f(\lambda)}{s_o - f(\lambda)}. \quad (18)$$

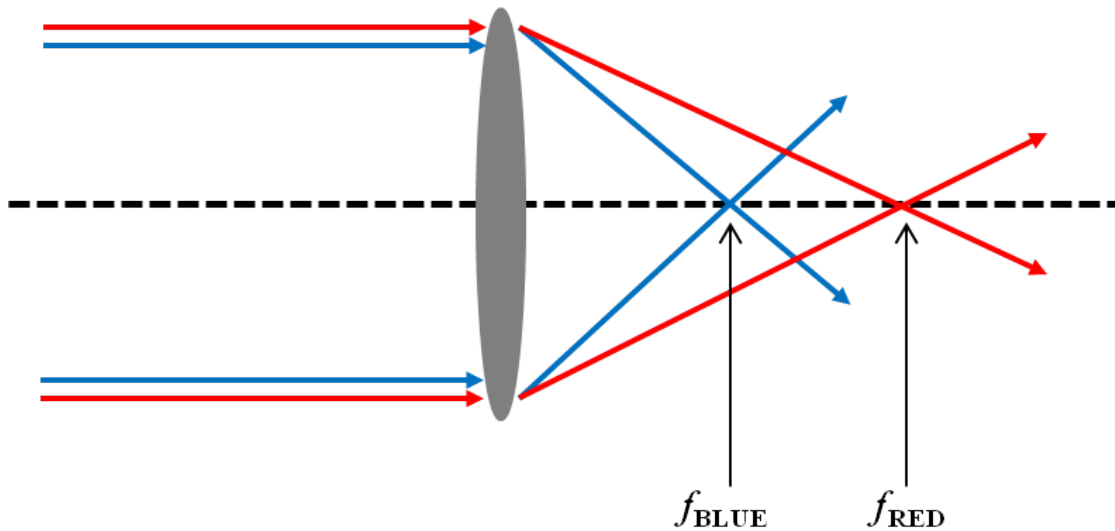


Figure 13. Chromatic Aberration. The colors of a polychromatic plane wave are dispersed such that the individual wavelengths focus at different locations along the optical axis.

Eq. 18 makes it clear that light of different colors will form focused images at different locations. When a source is polychromatic, the resultant image will be distorted as the various wavelengths of light are “smeared” across a range of image planes. Fig. 13 demonstrates this concept as the blue light is focused closer to the lens than the red light. An image composed of these two colors would consequently be blurred.

Diffractive Optics.

In the previous example, the focal length was indirectly a function of wavelength (through the index of refraction). In the case of diffractive optics, this effect is more directly apparent and magnified well-beyond the dispersion of traditional glass lenses (30:76). For example, by solving Eq. 8 for f , it is evident that the focal length of a photon sieve is directly, and very much, dependent on wavelength and will thus be subject to chromatic aberration (21:496):

$$f = \left[R_n^2 - \frac{n^2 \lambda^2}{4} \right] / 2n\lambda . \quad (19)$$

Measurement.

Chromatic aberration can be quantified for an optical system in several ways. First, it may be measured by comparing the difference in focal length between light of two different wavelengths, a value Hecht refers to as Axial Chromatic Aberration (ACA) (21:268). ACA may be calculated using:

$$ACA = \Delta f = f_{\lambda_2} - f_{\lambda_1} . \quad (20)$$

No convention is specified as to which direction is considered positive ACA; however, the method adopted for this thesis is to consider focal movement away from the imaging optic as positive and movement back toward the optic as negative. For example, if the

focus occurs at 10 cm for an optic at its primary wavelength but focuses at 15 cm at a second wavelength, the second wavelength would show positive ACA of 5 cm. In Fig. 14, the left image was formed using a photon sieve at 741 nm with the image magnifier in the focal plane corresponding to 740 nm. In other words, at 740 nm the image would be clear, but at 741 nm it is blurred due to chromatic aberration. The image magnifier was then moved toward the sieve until the number became focused. The distance moved was approximately -2.5 mm and is the difference in image location at 740 nm and 741 nm. The difference in focal length can be determined from this change in image location (discussed later), allowing calculation of ACA from Eq. 20. Note that when specifically addressing chromatic aberration, ACA is the type referenced throughout this thesis.

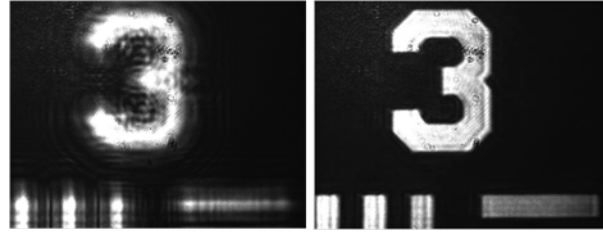


Figure 14. Wavelength-Dependent Focal Distance Changes. Both images were formed by a 10-cm photon sieve using a Ti:Sapphire laser at 741 nm. The left image was captured in the 740-nm image plane. The right image was captured in the 741-nm image plane and is in focus. The difference between the image planes was -2.5 mm. No diffuser was used to form these images.

A variation of the ACA measurement described by Eq. 20 is defined in terms of lens power: $\phi = 1/f$. In this case, the aberration is measured as a difference in power rather than focal length (and is primarily a convenience in certain applications):

$$\Delta\phi = \phi_{LONG\lambda} - \phi_{SHORT\lambda} = c(n_{LONG\lambda} - n_{SHORT\lambda}), \quad (21)$$

where c represents the lens curvature (30:61). In a laboratory setting, however, it is still necessary to measure the image position, so Eq. 20 is used throughout this thesis.

Still another manner in which to view chromatic aberration is in terms of Lateral Chromatic Aberration (LCA). Eq. 18 illustrates a dependence of s_i on wavelength. Because s_i is used to determine vertical magnification, the vertical size of an image will also change at each wavelength in addition to the in-focus location. This difference in height of images at two different colors is LCA (21:268).

Aberration Correction

Traditional Method.

Traditional correction of chromatic aberration has involved constructing a system of lenses that compensate for each other: “Chromatic aberration can be corrected by combining lenses whose total power is equal to the required power, but whose total dispersion is zero” (30:62). An achromatic doublet, for example, combines a positive and a negative lens such that rays refracted first by the positive lens are refracted in the opposite direction by the negative lens in a manner that allows different colors to focus at the same point (21:269). It is important to note, however, that the designs of these compensators are optimized for particular wavelengths and will thus still show chromatic aberration at other colors and even imperfect correction at the chosen colors (21:269; 30:61). A quantity known as the Abbe number (V_d) is typically published as a way of listing how well a lens performs over a polychromatic range and is based on the method of aberration measurement described by Eq. 21. Higher numbers indicate less chromatic aberration (30:61):

$$\frac{\Delta\phi}{\phi_{CENTER\ \lambda}} = \frac{1}{V_d}. \quad (22)$$

Diffractive Optics Methods.

Diffractive optics may also be used instead of lenses to fix chromatic aberration (30:63). One major advantage of using these devices is that, as previously mentioned, the high dispersion of diffractive optics means that “only a small amount of diffractive power is required to correct a chromatic lens” (30:76). Furthermore, as illustrated in Fig. 6, some optics of this type may produce both the positive and negative diffraction orders, allowing for flexibility depending on which direction of corrective dispersion is required.

Several techniques have already been demonstrated to provide diffractive optic-based chromatic aberration correction. For example, a diffraction grating can be used to help offset spectral dispersion (28:2440). Holography has also been employed to correct general aberrations in an optical system (see Refs. 5; 7; 27; 28; 36) and also as a manner in which to address chromatic aberration specifically (see Refs. 4 and 22). In particular, Ref. 5 claims a 47-nm effective bandwidth for a sieve employing holographic correction (5:6). While the concept of holography will be detailed below, Ref. 36 discusses the key principle governing the use of holograms in this manner:

The hologram thus constructed behaves like a diffraction grating, producing a zero order and a pair of first-order diffracted waves. One of the first-order waves is of the form $a_0 a_1 e^{j(\alpha u - \phi)}$; this term contains a phase defect, $e^{-j\phi}$, that is the conjugate to the one which the lens produces, and can therefore be used to correct the aberration. (36:589)

In theory, a FZP (or photon sieve) can be used as a hologram and should therefore also be able to compensate for primary optic aberrations. The equivalence of these diffractive optics to holograms is the subject of the next section.

Holograms

Traditional Holograms.

Traditional holographic elements may be used for aberration correction by essentially storing information about how an optic causes aberration in an image and then using this information to reconstruct an unaberrated version of the desired image (19:297, 386). Fig. 15 illustrates the basic concept of holographic correction (7:1428). In its simplest form, a wavefront is focused by an aberrated optic, and in the process, the wavefront is also distorted by the aberrations in the element. The aberrated wavefront is then interfered with a controlled reference wavefront, and the resulting pattern is recorded as a hologram on film (7:1427-1428). The hologram is placed in position after the primary optic and corrects the wavefront by imparting “complementary” aberration to cancel the problems with the primary (26:4).

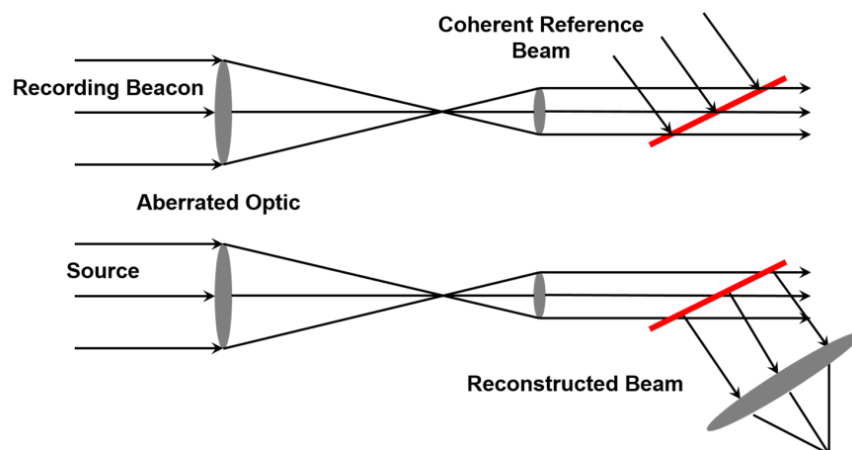


Figure 15. Hologram Recording Geometry. Adapted from Ref. 7, this diagram shows the basic recording and reconstructing geometry of a hologram. Aberrations imparted to the wavefront by the primary optic are recorded on the hologram which is then used as a corrector to remove the aberrations from a new wavefront showing the same problems.

Computer-Generated Holograms.

The method described in the previous section can also be accomplished synthetically through a process described in Ref. 19. Using Fig. 15 as an example, it would be necessary to first simulate the interference of the object and reference fields at the hologram location and mimic this interference pattern synthetically. Next, the synthetic hologram would have to be produced for use (19:355). As Goodman suggests, one of the benefits to using this type of element is that the problems associated with manually forming a hologram (including the requirement to actually have the object being recorded) are negated (19:355).

Binary Holograms.

Lee highlights a particular subset of computer-generated holograms in which the mathematical (computer-generated) function that describes the hologram is reduced to a set of binary values (24:1677-1678). The hologram is thus a set of points that are “on” or “off” and consequently affect both amplitude and phase of an incident wavefront (24:1677; 25:3663). A benefit of a binary hologram suggested by Goodman is that the binary nature is easier to print for application as opposed to a more fluid spectrum (grayscale) of phase and amplitude changes (19:366). Of course, Lee notes that the other side to this argument is that the “on” and “off” nature limits the information in the hologram to binary approximations only (24:1677).

FZP or Photon Sieve as a Hologram.

The main property of binary holograms relevant to this research is that they can represent interference patterns (25:3661). This result is not unexpected as traditional holograms are interference patterns recorded on film. What is interesting, however, is

that a FZP (or a photon sieve) is itself a binary hologram which can be used in aberration correction (36:591).

Fig. 16 helps illustrate this idea (24:1680). Lee conducted an experiment in which a binary hologram was imaged with a lens using two incident plane waves such that both the +1 and -1 diffraction orders were reconstructed by the hologram and combined (interfered) in the image plane.

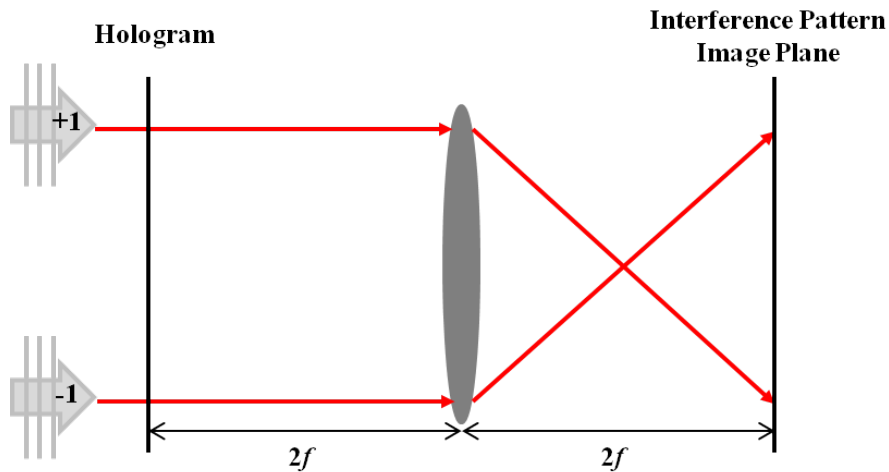


Figure 16. Hologram Modeled by Interference Pattern. Adapted from Ref. 24, a hologram is imaged with a lens, and the resulting image is itself a FZP.

The interference pattern (which is essentially an image of the +1 and -1 holograms combined) was of the same form as a FZP (see Ref. 24:1679-1680). In other words, the experiment demonstrated that a FZP based on the resultant image is essentially equivalent to the original hologram.

The key point of emphasis is that a FZP, or a photon sieve by extension, can be used as a holographic corrector. Because both the locations of the holes as well as the diameters can be manipulated, this method offers a flexible correction technique.

Furthermore, the process of filming a hologram, and its associated difficulties, is avoided (40:109).

Chapter Summary

This chapter offered a review of the primary imaging concepts as well as the proposed correction methods applicable to this research. First, the application of photon sieves in visual imaging was discussed using both geometric and field theory analysis. Next, correction techniques were reviewed with a focus on reduction of aberration effects using holography. Lastly, the relationship between a hologram and a FZP (or photon sieve) was developed such that either device could theoretically be utilized to reduce chromatic aberration.

III. Methodology

This chapter discusses the experimental methods and techniques applied to the major phases of this project. First, the results of the radiometric analysis, performed to determine a bandwidth target for a corrector system, will be presented. Next, overall design considerations for both the primary and secondary photon sieves will be detailed. Finally, the laboratory setup, equipment used, and general experimental procedures will be addressed.

Radiometry

USAFA Analysis.

In order to determine an approximate bandwidth goal for this experiment, a radiometric study of the problem was necessary. In 2012, the USAFA conducted a similar analysis using the primary sieve characteristics from the current FalconSAT-7 design (32). For this thesis, they requested that another analysis be conducted for an optical system using a 30-cm, f/4 photon sieve (versus the current 20-cm, f/2 optic) (9:6). In contrast to the USAFA report, this analysis specifically targeted the imaging bandwidth required given a set integration time and no binning (32:9-10). The goal was to determine the signal-to-noise ratio (SNR) incident on a single pixel during photon sieve Earth-imaging across several bandwidth ranges. Specifically, the main objective was to find the bandwidth required to achieve an SNR of 6 (32:9). In addition to referencing the USAFA study and a similar analysis by Captain Myers, the essential theory governing the calculations below was derived primarily from Ref. 14.

Notional Bandwidth Analysis.

The following characteristics represent values and assumptions utilized throughout the problem. The optical system (photon sieve and detector array) orbits the Earth at a distance of $r_{E-SV} = 450$ km (32:8). The sieve has a diameter $d_{SV} = 30$ cm with a focal length of $f = 1.2$ m such that collimated (distant) incident light is focused on the detector placed a distance f behind the optic. The transmission ($T = 0.1$) of the sieve and quantum efficiency of the detector ($\eta = 0.4$) are assumed to be the same as those utilized in the USAFA analysis (32:8-9). The length of a square pixel is $d_P = 4.65 \mu\text{m}$ (29:84).

The first task was to determine the field-of-view (FOV) of an individual detector pixel. Fig. 17 illustrates the setup of this problem which assumes that the surfaces of the Earth, sieve, and detector are all parallel. Furthermore, it is noted that the portion of the Earth imaged onto the detector is much smaller (by a factor of $\sim 10^7$) than the diameter of the Earth, making the curvature of the Earth negligible. Using the geometric optics relationship between the size of an object and the size of its image, the height of a square portion of the Earth's surface (d_E) that is imaged onto one pixel is given by (14:19):

$$d_E = \frac{r_{E-SV}}{r_{SV-P}} d_P. \quad (23)$$

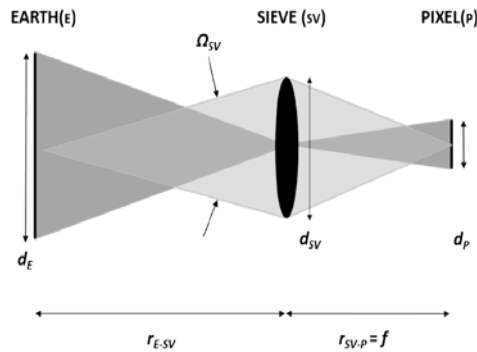


Figure 17. Radiometric Analysis Geometry. Energy is collected by the photon sieve from the portion of the Earth within a single-pixel FOV.

It is useful to rewrite Eq. 23 in terms of surface area, noting that $r_{SV-P} = f$, and that the area is simply the height squared:

$$A_E = \left(\frac{r_{E-SV}}{f} \right)^2 A_P . \quad (24)$$

The flux collected by the sieve from this area of the Earth is determined using

$$\Phi_{SV} = L_E A_E \Omega_{SV}, \Omega_{SV} = \frac{A_{SV}}{r_{E-SV}^2}, \quad (25)$$

where L_E [W/m² sr] is the radiance of the Earth (calculated later), A_E [m²] is the area of the square on the Earth imaged by the pixel, and Ω_{SV} [sr] is the solid angle subtended by the sieve (14:50, Eq. 2.25).

Using the paraxial optics approximation, Ω_{SV} is defined by

$$\Omega_{SV} = \frac{A_{SV}}{r_{E-SV}^2}, \quad (26)$$

and, when combined with Eqs. 24 and 25, yields (14:39)

$$\Phi_{SV} = L_E \frac{A_P}{f^2} A_{SV}. \quad (27)$$

Eq. 27 represents the power in energy per second [J/sec] collected by the sieve. To convert this quantity to number of photons collected per second (Φ_P), divide Eq. 27 by the approximate energy of each photon ($hc/\lambda_{H\alpha}$) (29:84), giving

$$\Phi_P = L_E \frac{A_P}{f^2} A_{SV} \left(\frac{\lambda_{H\alpha}}{hc} \right), \quad (28)$$

where $\lambda_{H\alpha} = 656.28$ nm is the center of the bandwidth range used in the USAFA analysis (32:5). To convert the number of photons collected by the sieve to the number of electrons incident on one detector pixel (N_e) during a set camera integration time (t), multiply Eq. 28 by this time as well as T and η (32:8), yielding

$$N_e = L_E \frac{A_P}{f^2} A_{SV} \frac{\lambda_{H\alpha}}{hc} T t \eta . \quad (29)$$

All of the quantities in Eq. 29 are known except L_E which is a result of the radiance of the Sun (L_S) reflected off of the Earth. Treating the Sun as a blackbody, L_S is determined using Planck's blackbody integral (14:56, 66, Table 2.4, Eq. 2.79),

$$L_S = \int_{\lambda_1}^{\lambda_2} \frac{2hc^2}{\lambda^5 (e^{\frac{hc}{k\lambda T}} - 1)} d\lambda . \quad (30)$$

To determine the irradiance (E_E) on the Earth, it is necessary to view the Sun as an extended source and use

$$E_E = \pi \sin^2 \theta L_S = \frac{A_S}{r_{E-S}^2} L_S = \Omega_S L_S , \quad (31)$$

where θ is the half-angle between the center of the Earth and the edge of the Sun (14:54-55, Fig. 2.21, Eq. 2.38). Eq. 31 uses the small angle approximation, $\sin \theta \approx \frac{r_{SUN}}{r_{E-S}}$, where the radius of the Sun (r_{SUN}) is 6.96×10^8 m and the distance between the Earth and the Sun (r_{E-S}) is 1.52×10^{11} m. The exitance (M_E) of the Earth is the reflectance (R) multiplied by E_E :

$$M_E = R \frac{A_S}{r_{E-S}^2} L_S . \quad (32)$$

Finally, assuming the Earth is Lambertian and applying

$$M_E = \pi L_E , \quad (33)$$

the radiance is written as (14:47, Eq. 2.18):

$$L_E = \frac{1}{\pi} R \frac{A_S}{r_{E-S}^2} L_S . \quad (34)$$

Combining Eqs. 30 and 34 yields

$$L_E = \frac{1}{\pi} R \frac{A_S}{r_{E-S}^2} \left(\int_{\lambda_1}^{\lambda_2} \frac{2hc^2}{\lambda^5 (e^{\frac{hc}{k\lambda T}} - 1)} d\lambda \right), \quad (35)$$

and, when inserted into Eq. 29, gives the total number of electrons incident on a pixel:

$$N_e = \frac{R}{\pi} \frac{A_S}{r_{E-S}^2} \left(\int_{\lambda_1}^{\lambda_2} \frac{2hc^2 d\lambda}{\lambda^5 (e^{\frac{hc}{k\lambda T}} - 1)} \right) \frac{A_P}{f^2} A_{SV} \left(\frac{\lambda_{H\alpha}}{hc} \right) T t \eta. \quad (36)$$

The energy of each photon is considered nearly constant across the bandwidth, allowing the inverse of this term ($\lambda_{H\alpha}/hc$) to remain outside the integral. For consistency, SNR is determined using the same assumptions and expression as the USAFA (32:9, 29:85):

$$\text{SNR} = \frac{N_e}{\sqrt{N_e + n_{READ}^2}}, \quad (37)$$

where the read noise, n_{READ} , was assumed to be 10 electrons (32:9).

The final piece of information necessary for analysis is the camera integration time (t). FalconSAT-7 uses an exposure time of 2.3 msec (9:7). Without derivation, the integration time selected for this notional sieve-based system was 1.5 msec. Evaluating Eq. 37 and plotting SNR against bandwidth results in the plots shown in Figs. 18 and 19. A SNR of 6 corresponds to a bandwidth of approximately 8 nm, the value that will thus be used as the target bandwidth for this experiment.

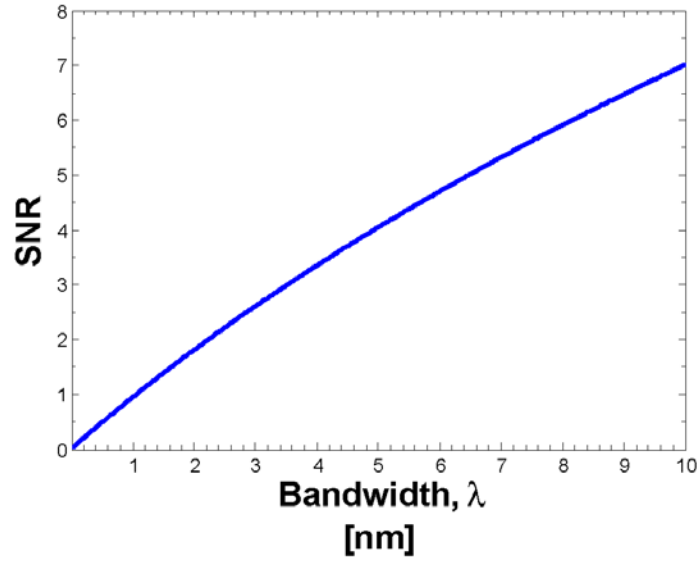


Figure 18. SNR-Bandwidth Correlation. In order to achieve a SNR of 6 with the notional f/4 system and a 1.5-msec integration time, the bandwidth needs to be approximately 8 nm.

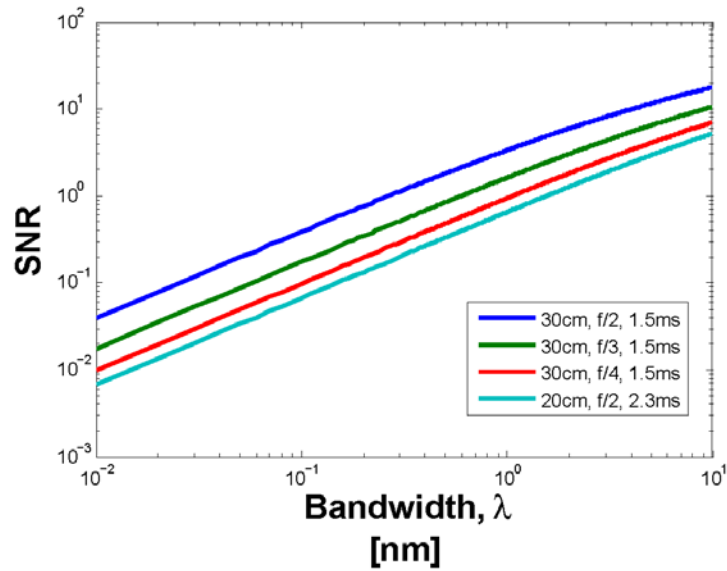


Figure 19. SNR-Bandwidth Correlation across Design Options. Varying the f/# results in different SNR curves. Of interest, the dark blue (second-from-bottom) line compared to the green (bottom) line demonstrates the improvement of the notional system (second-from-bottom) over the current (bottom) design. The figure shows that an SNR of 6 corresponds to a bandwidth of 8 nm in this analysis but could be achieved with a 2 nm bandwidth using a 30-cm f/2 sieve (red, top line).

Design

Primary.

After determining a target bandwidth, a primary photon sieve was constructed and characterized in order to first measure its chromatic aberration and then design a method to correct it. Several parameters had to be considered when creating the sieve in addition to the hole locations and diameters. Some of the considerations that will be discussed include required laboratory space and available equipment, wavelength and desired light source, precision of the sieve (whether the paraxial approximation is valid), and printing resolution concerns.

The available laboratory space and equipment at the Air Force Institute of Technology (AFIT) were primary considerations. First, due to a lack of large collimating optics, a good size (10-cm) sieve could not be designed for infinite conjugate imaging. Instead, point-to-point imaging was required. This restriction, however, was a concern because more table-space was necessary. Rather than requiring only enough space prior to the sieve to collimate a beam and then one focal length after the sieve, a distance of $2f$ was required on both sides to image a point. The optics table was approximately 3.6 m, so it was decided to build the sieve such that $f = 0.5$ m to give adequate space to configure the experiment and include necessary corrector optics.

Additionally, because increased bandwidth in the visible region was the goal, the USAFA requested that the test source likewise be in the visible spectrum. Furthermore, wavelength tuning was required, so a Spectra Physics Model 3900S Ti:Sapphire laser was selected. The laser was pumped by a Coherent Verdi 18W (max power) diode-pumped, frequency-doubled Nd:Vanadate laser and output approximately 5-15% of the

pump setting depending on the wavelength. The pump was only set to 2-8 W during testing. Based on these two requirements, 740 nm was selected as the design wavelength because it was in the visible region and also provided sufficient range to tune the laser and still get a useable output power (see Fig. 20).

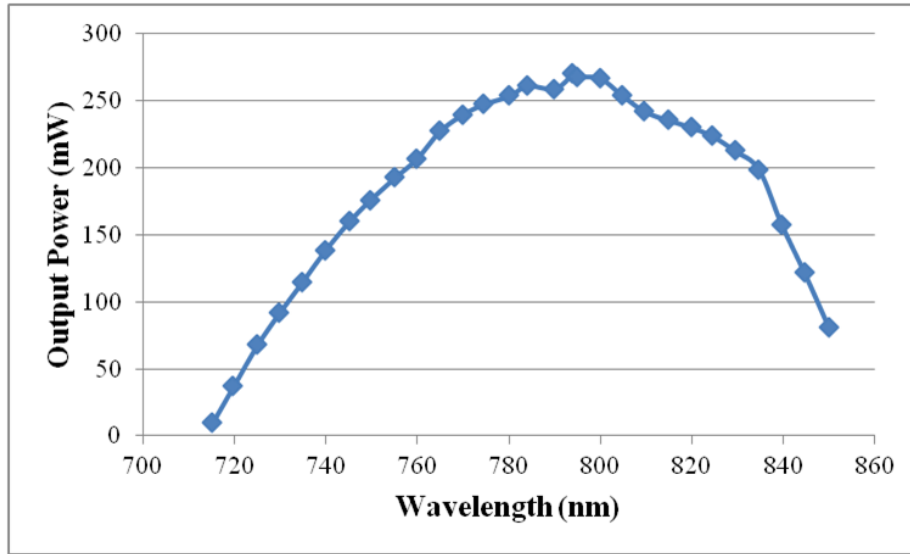


Figure 20. Ti:Sapphire Output Power. 740 nm was chosen as the design wavelength for the primary sieve due to sufficient power output being available in a 20-nm range about the central wavelength. The pump was operated at 3.3 W during testing. The max output of approximately 275 mW thus represents 8.3% of the pump power.

Next, although the full version of Eq. 8 was utilized to determine the radial position of the holes, the shorter (paraxial) version is also valid with this setup. Recall that Cao and Jahns used the Fresnel diffraction integral to determine the radial zone positions. The Fresnel integral employs the paraxial approximation to the Rayleigh-Sommerfeld integral, and with this approximation is an associated error (19:66-67; 10:1006). For this particular experiment, an error of 6.6 radians in making the paraxial approximation is determined by (10:1006):

$$\text{Error} = \frac{2\pi \left(\frac{D_{\text{SIEVE}}}{2} \right)^4}{\lambda 8(2f)^3}. \quad (38)$$

This error can be neglected, as Goodman suggests, if it does not “significantly” alter the outcome of the Rayleigh-Sommerfeld integral (19:69). In this case, the additional 6.6 radians changes the expression insignificantly, allowing use of the paraxial approximation if desired.

Lastly, resolution of the printing process was a major consideration in the primary sieve design. The printing company guaranteed a tolerance of $\pm 0.25 \mu\text{m}$ for hole diameter and required at least $1.5 \mu\text{m}$ of space between features. Because of these restrictions, the radial positions of the holes as well as the lateral number of holes in each ring was adjusted from the ideal configuration.

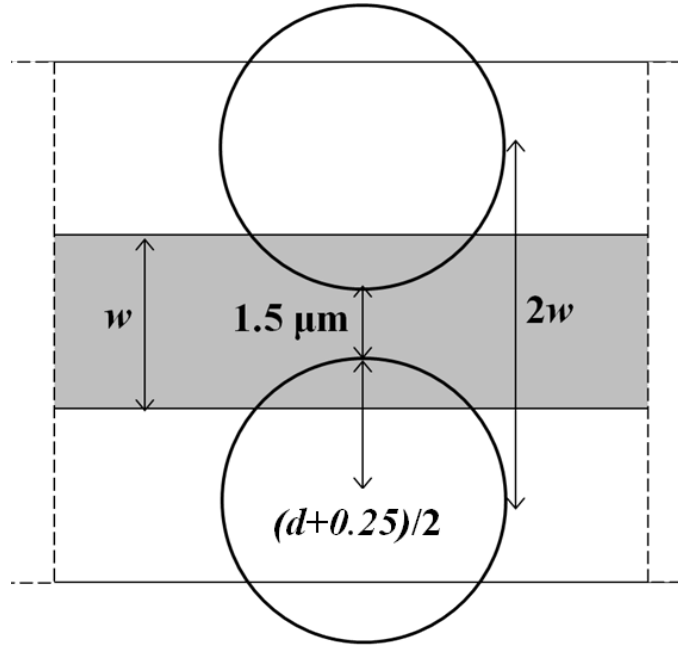


Figure 21. Radial Hole Spacing. The ratio d/w was adjusted such that there would always be the required $1.5 \mu\text{m}$ between holes.

In order to comply with the required radial spacing, the hole diameter was adjusted such that 1.5 μm of space existed between adjacent holes (see Fig. 21). The smallest zone (and therefore minimum spacing between holes) occurs at the outside of a sieve (see Eq. 11). The width of the outermost ring was thus determined by

$$w_{MIN} = \frac{\lambda f}{2R_{MAX}} = 3.7\mu\text{m} . \quad (39)$$

Once the minimum zone size was calculated, a restriction on the largest hole diameter in this ring was found ($d \leq 5.65 \mu\text{m}$) according to

$$\left[2 \times \left(\frac{d + 0.25}{2} \right) \right] + 1.5 \geq 2w . \quad (40)$$

Combining these results yields $d/w = 1.52703$ in the outer ring, which is slightly less than the optimal value of 1.53 already discussed. Fig. 12, however, shows that there should still be constructive interference using this ratio, and Ref. 1 demonstrates a precedent for applying a non-ideal (but acceptable) d/w value for resolution concerns. Accordingly, in rings where the hole separation became less than 1.5 μm , $d/w = 1.52$ was used. Applying this scheme, 99.36% of the sieve was still covered by normal holes, indicating that there was not a significant loss in coverage.

In order to provide at least 1.5 μm of lateral spacing a similar approach was taken. Essentially, the number of holes in each ring was reduced below the maximum number of possible holes in order to provide enough space between the features. Referring to Fig. 22, each hole was linked with the space to the left of it, forming a hole-space pair. The ratio of hole diameter to this hole-space distance was calculated and then multiplied by the maximum number of holes possible in each ring.

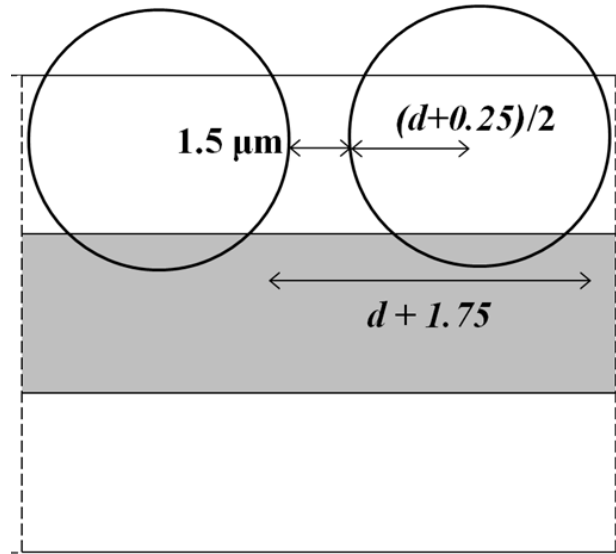


Figure 22. Lateral Hole Spacing. The number of holes per ring was scaled to less than maximum to ensure the required spacing.

This procedure effectively set the number of holes that could fit in the ring given the required spacing and was always less than the maximum number possible. In the actual primary design, the number of holes in the outer rings (where the overlap was most of a concern) was reduced to 72% of the maximum value. In the inner rings, the maximum value was only reduced to 97% (and that was because of an included buffer of 3%). Note that lateral overlapping of holes is not as extreme a problem as radial overlapping. Because the underlying Fresnel zones are rings, lateral overlap simply provides more coverage. Because the point of this project was to test a sieve specifically, however, the separation was necessary.

MATLAB was used to create code which accounted for these considerations and output positions and sizes for each of the 71,715,741 holes incorporated in the primary sieve. The MATLAB code generated a text file of aperture dimensions and positions in Gerber file format for use by the printing company (18; 15; 38). The MATLAB code is

included in the Appendix as well as sample Gerber format text file. Table 1 lists the specifications of the primary sieve designed for this project. Of note, approximately 48% of the sieve surface is covered by holes. While this value is close to the desired 50% coverage of the underlying FZP, the hole diameters are larger than the underlying zones, so actual coverage of the FZP transmission zones by holes is not this high (2). Additionally, Figs. 23 and 24 show photos and additional measurements of the optic.

Table 1. Primary Photon Sieve Characteristics

Wavelength (nm)	740
Focal Length (cm)	50
Diameter (cm)	10
F/#	5
Total Rings	3,376
Total Holes	71,715,741
Minimum Scale Factor (Lateral Separation)	0.72
Maximum Scale Factor (Lateral Separation)	0.97
Area Covered By Standard Hole Size (%)	99.02%
Maximum Hole Diameter (μm)	329.04
Minimum Hole Diameter (μm)	5.65
nMax Lateral Hole Separation (μm)	2.24
Outer Ring d/w	1.52
Area Covered (%)	47.97



Figure 23. Primary Photon Sieve Image. The sieve was created by printing the hole pattern in chrome on a quartz substrate. It has a 10-cm diameter and a focal length of 0.5 m. There are 3,376 rings and 71,715,741 holes with sizes ranging from 329.04 μm (center) to 5.65 μm (edge).

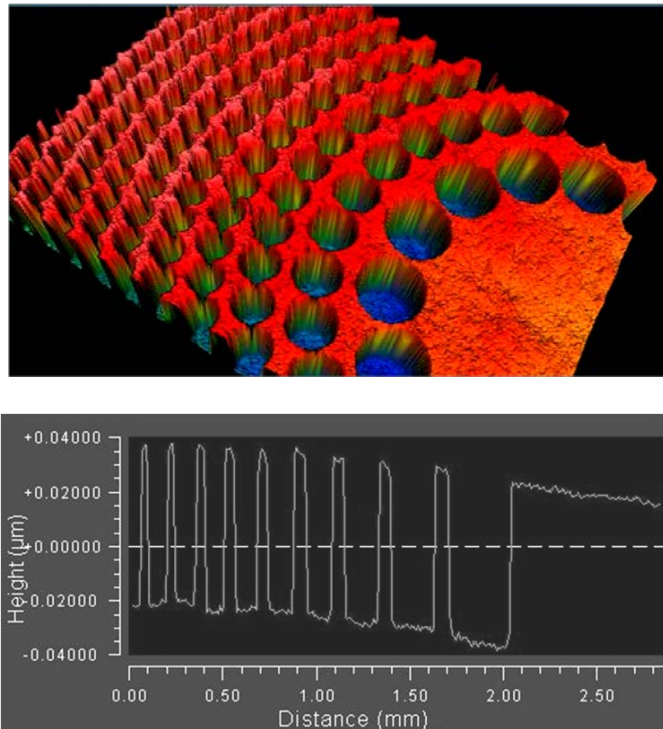


Figure 24. Profilometer Images of Photon Sieve Center. Top: The rendering shows the three-dimensional effect of printing the pattern in chrome on quartz. Bottom: Using a side view of the image, it can be seen that the depth of the holes is approximately 0.06 μm .

Secondary.

This section discusses basic design considerations for the corrector elements. Specifically, the purpose is to review any major differences from the primary design as well as briefly highlight the correction approach. This section does not include examples or comparisons of corrector designs as this is reserved for Chapter IV where the analysis utilized to settle on a final design is detailed. Considerations unique to the optical design software used (Zemax) are also introduced.

Considerations and Assumptions.

First, the basic scheme used for correction in this experiment is the same as that presented in Ref. 22. This method requires that a traditional lens image the primary optic onto the secondary such that the combined system ray matrix does not have a wavelength dependence (and therefore theoretically shows no chromatic aberration) (22). The post-lens beam need not be collimated; however, due to simplicity in modeling the corrector device, a collimated beam was selected (22). The corrector, therefore, was designed for infinite conjugate imaging (as opposed to point-to-point).

Next, as will be discussed in Chapter IV, the size of the beam incident on the corrector was smaller than that incident on the primary (only 2.3 cm in one case as opposed to the 10-cm primary beam). With a collimated, it is not helpful to make a corrector larger than the beam. Consequently, the corrector elements themselves were small.

With small devices, concerns arise regarding the size of the features and the printing resolution. With the primary sieve, the zone size was always larger than the smallest printable feature. With the small corrector, however, the zone (and associated

hole) sizes became smaller than that allowed by the printing resolution. In order to deal with this problem, the hole sizes were set to a minimum value of $1.5\text{ }\mu\text{m}$, a technique adapted from Andersen (1:2976). Again, the d/w was not ideal as d remained constant while w decreased. Using the information in Table 6 (p. 74) and Fig. 12 (p. 20), the d/w values (2.02 and 1.40) were still sufficient to provide some constructive interference. An additional problem arose because the zone sizes kept reducing while the hole size remained constant, leading to decreased radial spacing between holes. To deal with this problem, every other ring in the outer portion of the sieve (and rings in the corresponding FZP) was skipped. While this method solved the problem, the number of holes (and overall sieve efficiency) was heavily decreased (down to 19% coverage in one case).

Zemax Modeling.

Zemax optical design software was used to model the primary photon sieve system and determine an adequate corrector design scheme. Treating a photon sieve as a form of hologram has already been discussed. As such, in Zemax the sieves and zone plates were modeled as holographic elements (2; 8). In particular, the primary photon sieve was simulated as a hologram that provided point-to-point imaging with one-to-one magnification, which occurs when both the object and image distances are $2f$ from the optic (see Eq. 18).



Figure 25. Primary Photon Sieve Ray Fan. A point source placed at a distance $2f$ to the left of the sieve is imaged at a distance $2f$ to the right of the sieve. The image will be inverted but unmagnified.

To simulate a hologram, Zemax allows entry of the coordinates of both the construction (object) and reference sources as well as construction wavelength, aperture

size, and required diffraction order (39:168-169). Fig. 26 illustrates the basic geometry for the general case of object, reference, and reconstruction point sources unrestricted in three dimensions.

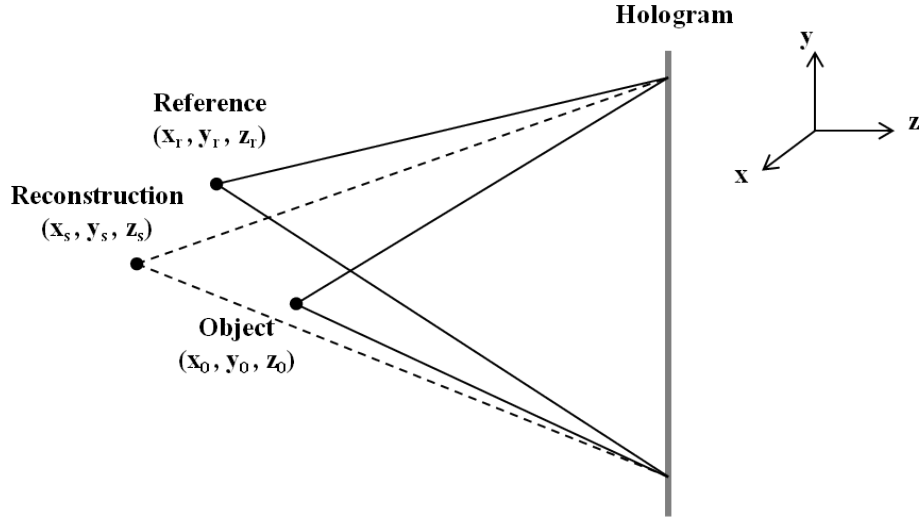


Figure 26. Hologram Geometry. An object and reference beam are interfered to create the hologram. A reconstruction source is then passed through the hologram, producing an image according to Eq. 41.

The location of an image produced by a hologram is given by

$$z_i = \left(\frac{1}{z_s} \pm \frac{\lambda_2}{\lambda_1 z_r} \mp \frac{\lambda_2}{\lambda_1 z_o} \right)^{-1}, \quad (41)$$

where λ_1 and λ_2 refer to the construction and reconstruction wavelengths, respectively, and are equal for the primary sieve in this experiment (19:319, Eq. 9-38). As already noted, the reconstruction source (to be imaged by the sieve) was placed at $z_s = 2f$ to achieve the desired one-to-one imaging. Furthermore, when $z_r = z_o = 2f$, the image location is given by $z_i = \pm 2f$. Modeled in this way, the hologram thus behaves exactly like the designed sieve in that two images (one positive and one negative) are formed at the one-to-one imaging distance, $\pm 2f$.

Correction Scheme Design.

After modeling the primary sieve, the next step was to develop a secondary correction scheme that allowed diffraction-limited performance of this particular sieve across a larger bandwidth than that of the primary alone. As previously noted, two requirements of the secondary system are that 1) the primary sieve needs to be imaged onto the corrector by an achromat (See Ref. 22), and 2) the corrector needs to have dispersion opposite that of the first element. Additionally, a third requirement is that the focal length of the corrector be selected such that the transmitted light does not diverge too fast to be collected and focused (2). Fig. 27 illustrates this setup. Note that the light traveling through the system does not reflect from the second sieve (as would appear in the figure). The light is transmitted and then diverges. Zemax projects this divergent light backward to a virtual source. This technique allows analysis of the point of divergence (or how good the point source is after traversing the optical system) (2).

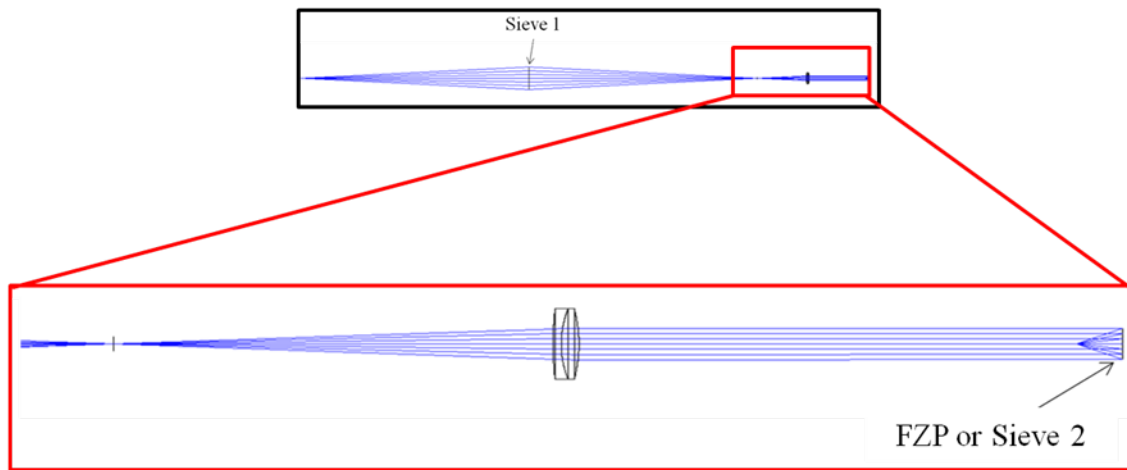


Figure 27. Corrected System Ray Fan. The lower image is a magnified portion of the top. Light from a point source travels through the primary photon sieve and is focused. An achromatic doublet is used to collimate the diverging light. A second photon sieve is placed in this collimated beam at the image location of the primary sieve (imaged by the doublet). Light then diverges (and also converges as both positive and negative diffraction orders are present) after passing through the second sieve. Only the divergent order is pictured and is illustrated as a backward projection of the divergent transmitted light (a virtual source).

The secondary FZP/sieve was modeled in the same manner as the first; however, design parameters were allowed to vary (during optimization) in order to achieve the best correction (as opposed to the primary sieve where both f and λ were set). The diameter of the corrector was determined by the collimated beam size. Several collimating lenses (different focal lengths) were modeled and resulted in different beam sizes (see Chapter IV). For a given lens, however, the beam size was fixed. Consequently, the only variables allowed to change were f and λ of the second FZP/sieve. Once these parameters were optimized, the corrector could be created easily with slight modifications to the MATLAB code already developed (see Appendix).

Zemax has the built-in ability to vary these factors in order to optimize the system for a given parameter. The chosen parameter to minimize was RMS (Root-Mean-Square) Wavefront Error with Respect to Centroid (RWCE) (2; 39:296). According to the Zemax manual, both RMS and centroid references are the most common while performing wavefront optimization (39:274). Note that, throughout this thesis, diffraction-limited performance results are judged according to peak-to-valley (PTV) wavefront error being less than 0.25λ rather than an RMS error threshold. The RWCE routine allows optimization over all sources of error, however, and therefore should yield the best possible wavefront (39:274). Because of this expectation, the RWCE scheme was adopted. The next section discusses further the link between wavelength adjustment and wavefront aberration.

Wavelength Adjustment.

A correlation between the wavelength of the light source and the induced optical system wavefront aberration was observed while conducting laboratory characterization

of the primary photon sieve. During testing it became necessary to tune the laser away from the sieve design wavelength (740 nm) by nearly 9 nm to achieve diffraction-limited performance. It was later determined that the poor performance at 740 nm (where it was expected to be optimal) was because the distance between the point-source and the sieve was not equal to the distance between the sieve and the focus as had been planned. In effect, the system had been unintentionally setup to operate best at 731 nm. This error resulted in a system that exhibited off-wavelength aberration at 740 nm; however, it also suggested a way to remove the aberration (tuning the laser to a new wavelength).

This link between wavelength variation and resultant aberration was immediately applied to design of the secondary. Further research offered an explanation as to why this effect was observed. As previously noted, a hologram (or equivalent element) can be utilized for aberration correction. A hologram, however, is recorded at a unique wavelength and will itself cause wavefront aberration if reconstructed using light of a different color (20:31). In particular, Munch and Wuerker state that “the magnitude of the [system] aberration is recorded as a phase shift at the recording wavelength.” When the hologram is reconstructed at a different wavelength, the phase shift applied to the wavefront may be too large or too small (27:1316). In other words, an off-wavelength hologram could increase or decrease the overall system wavefront aberration. Andersen and Knize note that, in the latter case, there may still be some amount of improvement short of total correction (6:590). While this effect is typically regarded as problematic, the idea of applying less-than-total correction was leveraged in this project where *maximum* correction at the *primary* wavelength was not required but rather *acceptable* (diffraction-limited) correction over a polychromatic *range*.

Accordingly, using Zemax, both focal length and wavelength of the corrector were permitted to vary as part of the program's optimization scheme. First, without varying design wavelength (restricting it to 740 nm and solely varying focal length), diffraction-limited performance was only predicted over a bandwidth of approximately 0.001-0.01 nm. Second, it is demonstrated in Chapter IV that also varying the construction wavelength (by only 1 nm) effectively expanded the predicted diffraction-limited bandwidth approximately 800 times larger than that achieved by varying f alone. This result would suggest that adjusting the design wavelength of a corrector away from the primary wavelength of the system may be beneficial to bandwidth broadening.

Primary and Secondary Characterization

Setup.

Once the primary sieve was designed and constructed, it was necessary to characterize its performance 1) as a baseline for correction effectiveness and 2) as a way to judge how well Zemax modeled it. The method of characterizing the primary photon sieve was essentially the same as that applied in Ref. 5. In fact, some characterization was accomplished during a visit to the USAFA to work with Andersen directly. The results of the characterization study are discussed in Chapter IV; however, the experimental setup is depicted in Figs. 28 and 30. Three tests were conducted to test the performance of the sieve: focal spot analysis, imaging, and interference pattern study.

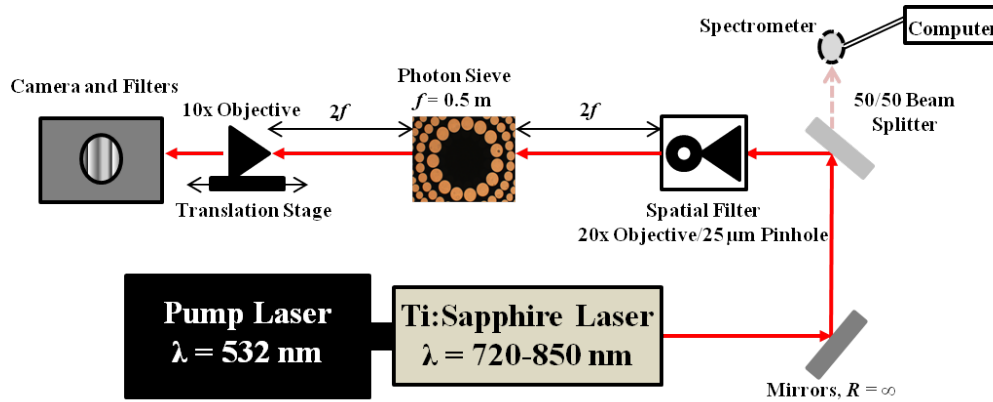


Figure 28. Lab Setup for Focal Spot and Imaging Analysis. Laser light was spatially-filtered by focusing the beam through a 25- μm pinhole using a 20x microscope objective. The light diverged until it was focused by the sieve a distance $2f = 1\text{ m}$ from the optic. A 10x or 20x microscope objective magnified the focus for viewing with a camera. While imaging, the spatial filter was replaced with a test target.

Focal Spot.

Referring to Fig. 28, the primary photon sieve was utilized to create an image of a point source for ACA and spot size analysis. A point source was created in the AFIT laboratory by spatially-filtering light from the tunable Ti:Sapphire laser using a 20x microscope objective to focus the beam through a 25- μm pinhole. The light then diverged and fell incident on the photon sieve at a distance 1 m ($2f$). The sieve focused the light to a point about 1 m away, and a microscope objective (10x or 20x) was placed on a translation stage to magnify the image onto a SBIG STF-8300M camera for viewing. As noted in Chapter I, tuning the laser resulted in varying image plane locations. Using the translation stage to move the magnifying objective, the in-focus spot position at each wavelength was estimated through visual analysis. The distance difference between the reference position at 740 nm and the off-wavelength focus was measured. This difference in image location was converted to a difference in focal length (ACA). A similar setup was used during the trip to the USAFA; however, the equipment parameters

were different. All of the chromatic aberration measurements, however, were taken in the AFIT lab. The spot size at 740 nm was also measured and compared to predictions.

Of note is the fact that the pinhole used to create a point source was likely too large, but no other pinhole was made available at AFIT. As such, the pinhole was not used during some measurements (specifically the size measurement in Fig. 39). Based on the calculations below, it was determined that the pinhole was likely passing most of the incident beam even while being used and was therefore superfluous.

Several different methods are described below for determining the required pinhole size for a spatial filter, but they all point to the need for a significantly smaller pinhole than the 25- μm pinhole used in this experiment. According to the Newport Corporation website, the appropriate diameter for a pinhole is given by

$$D_{PINHOLE} = \frac{f\lambda}{w_1'} = 9.26 \mu\text{m}, \quad (42)$$

where $w_1' = 0.64 \text{ mm}$ is the projected actual $1/e^2$ radius of the laser beam at the pinhole and was calculated using data from the experiment described in Ref. 13 (13, 33). The radius values assume that the spatial filter is approximately 0.7 m from the beam waist.

Another method for determining the pinhole diameter uses the size of an ideal and collimated laser beam incident on the pinhole and is calculated according to (37:78):

$$D_{PINHOLE} = \frac{4}{3} \times 2 \times \frac{f\lambda}{\pi w_1} = 8.82 \mu\text{m}, \quad (43)$$

where $w_1 = 0.57 \text{ mm}$ is the projected ideal beam radius at the pinhole (13). A pinhole is then selected to clip the excess light above this radius (33). Note that Eq. 43 assumes a perfectly Gaussian beam and uses a multiplicative factor of 4/3 to account for lens aberrations (37:78). Perhaps the most accurate method to determine the required pinhole

size is derived in Ref. 13. It still assumes an ideal beam but takes into consideration the beam curvature at the lens ($R_1 = 1.44$ m). This method gives the beam size at the pinhole:

$$D_{PINHOLE} = \frac{4}{3} \times 2 \times \left[\frac{\pi w_1}{\lambda} \left(\frac{1}{f} - \frac{1}{R_1} \right) \right]^{-1} = 8.84 \text{ } \mu\text{m} . \quad (44)$$

In all three cases, the required pinhole size is near $10 \text{ } \mu\text{m}$.

Imaging.

The same experiment described in the previous section was repeated using a ThorLabs Negative USAF 1951 Test Target instead of a point source (see Fig. 29). The target was placed at the location of the spatial filter. Again, in-focus distances of the image were measured to determine chromatic aberration effects. The target also allowed additional determination of diffraction-limited performance via resolution measurements of the resultant image. A spinning diffuser was added to the system such that the laser passed through a ground glass element prior to hitting the test target. The diffuser diminished speckle and resulted in better imaging and more accurate analysis of the sieve performance. Imaging and focal spot measurements were also performed on the FZP used in correction testing. All of the characterization results for both the primary and secondary are detailed in Chapter IV.

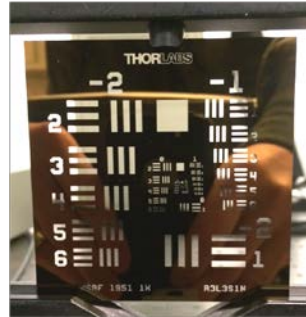


Figure 29. Resolution Chart Image. Each element grouping of the ThorLabs Negative USAF 1951 Test Target is characterized by the bar spacing and size. From this information, along with optical system arrangement data, it is possible to determine the resolution of a system.

Interferometry.

Lastly, it was possible to measure actual wavefront error using interference techniques and fringe analysis software. Fig. 30 represents a schematic of the setup. Point source light was again passed through the sieve and focused; however, divergent light from the focus was collimated using an achromatic lens. A second beam was split from the primary, passed through a spatial filter and also collimated. The second beam did not pass through the sieve and was therefore theoretically free of aberrations. The two collimated beams were interfered, and a picture was taken of the interference pattern. Fig. 31 is representation of one such interference pattern exhibiting high aberration due to an off-wavelength condition described in the previous section (the light that passed through the sieve was near 532 nm while the sieve was designed to operate at 740 nm). Using these images and the fringe analysis software, actual wavefront aberration was determined (see Chapter IV).

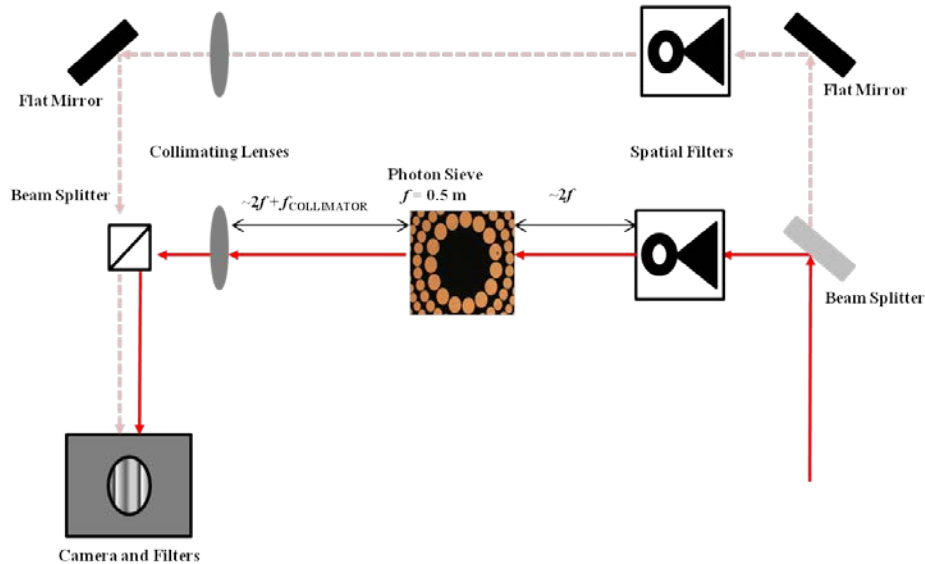


Figure 30. Lab Setup for Interference Pattern Analysis. As in Fig. 28, a point source was imaged by the sieve. The focused light, however, was collimated and interfered with another collimated beam free of aberrations from the photon sieve. The interference pattern was recorded using a camera.

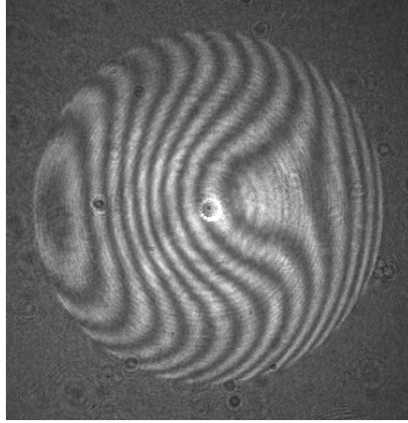


Figure 31. Off-Wavelength Interferogram. As described in the previous section, when light of one wavelength is passed through a hologram designed to operate at a different wavelength, aberration results. Light at approximately 532 nm was passed through a photon sieve designed to operate at 740 nm and then interfered with a theoretically unaberrated reference beam to produce this fringe pattern. If no aberrations were present, the fringes would be straight (2, 5). The curved nature of the fringes depicted here indicates high aberration (off-wavelength) of the system in this case.

Correction Effectiveness

Once a corrector optic was placed in the system, its effectiveness had to be measured. Again, these methods were adapted from Ref. 5. Fig. 32 depicts the correction system geometry. The primary sieve was utilized to image a point source. This focused light was collimated and passed through a corrector device (a second photon sieve or FZP). The device was placed in the plane where “the aberrations of the collector are imaged” (27:1312; 2; 26:4). In other words, the second sieve had to be located at the position where the collimating lens imaged the primary sieve (calculated in Zemax). The second sieve produced both divergent and convergent beams which were collected using a Nikon Nikkor 50-mm, f/1.4 camera lens placed close enough to the corrector to capture all the light (4:3708). The focused point could again be magnified and captured by the camera. Using this setup, the same experiments could be conducted as were done with the primary except now with an additional phase of optics.

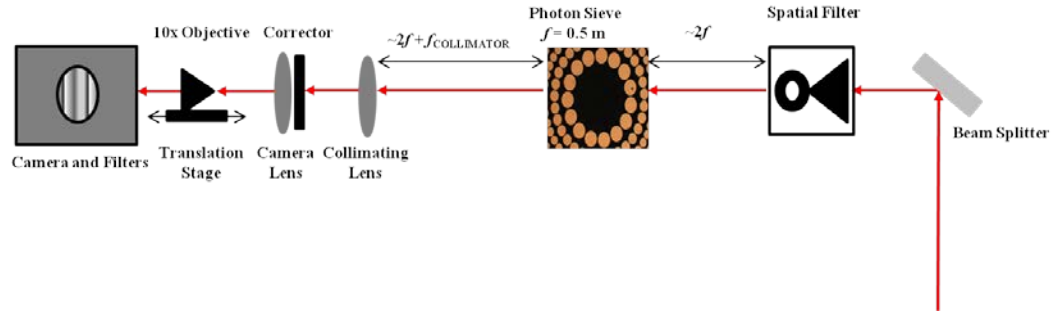


Figure 32. Lab Setup with Corrector. A spatially-filtered laser beam (point source) illuminated a photon sieve and was focused and then collimated. A corrector was placed at the location where the primary sieve was imaged by the collimated lens. The divergent light transmitted by the corrector was captured by a camera lens, focused, and magnified onto a camera for imaging.

Chapter Summary

This chapter discussed the radiometric analysis conducted to determine a target bandwidth required for the secondary design scheme. The 8-nm range neglects any losses due to the corrector but serves as an approximate goal for correction effectiveness. Modeling photon sieves in Zemax as well as basic wavefront error optimization concepts were also introduced. Finally, the experimental setups used to characterize the primary and secondary elements and also determine corrector effectiveness were highlighted. The next chapter details the results of this characterization and provides an in-depth analysis of the different secondary design schemes and their theoretical aberration-reduction effectiveness.

IV. Results and Analysis

Chapter III provided an overview of both the simulation techniques and the experimental methods used throughout this thesis. This chapter details the modeling and laboratory results. First, theoretical predictions of the primary photon sieve performance are presented followed by a discussion regarding how the experimental results compare to this simulated data. Next, modeling analysis of various secondary correction schemes is provided along with discussion as to which systems were chosen and why. Lastly, experimental data from a corrected system is reviewed.

Primary Modeling Predictions

Focal Spot.

Modeling the primary photon sieve in Zemax allowed estimates of the performance of the optic across various spectral bands. Zemax was able to simulate the image produced by a point source placed 1 m from the sieve (see Fig. 25). Fig. 33 illustrates this in-focus spot prediction at seven discrete wavelengths. Although not apparent in the depiction, the outer ring actually consists of two sets of overlaid dots. This ring represents the extreme wavelengths examined (731 nm, 749 nm) and shows that, over this bandwidth, the focal spot should span approximately 2400 μm . Additionally, Zemax predicted a RMS diameter of about 1330 μm . Note that the RMS measurement accounts for contribution from each ray in the focal spot while the edge-to-edge extent only considers the most divergent light. In other words, the RMS measurement is tighter because of a higher ray density near the center (39:78). The

diffraction-limited Airy disk diameter is $18\text{ }\mu\text{m}$ at the primary wavelength which is much smaller than the predicted image, indicating that the primary sieve will not provide diffraction-limited performance across this polychromatic range.

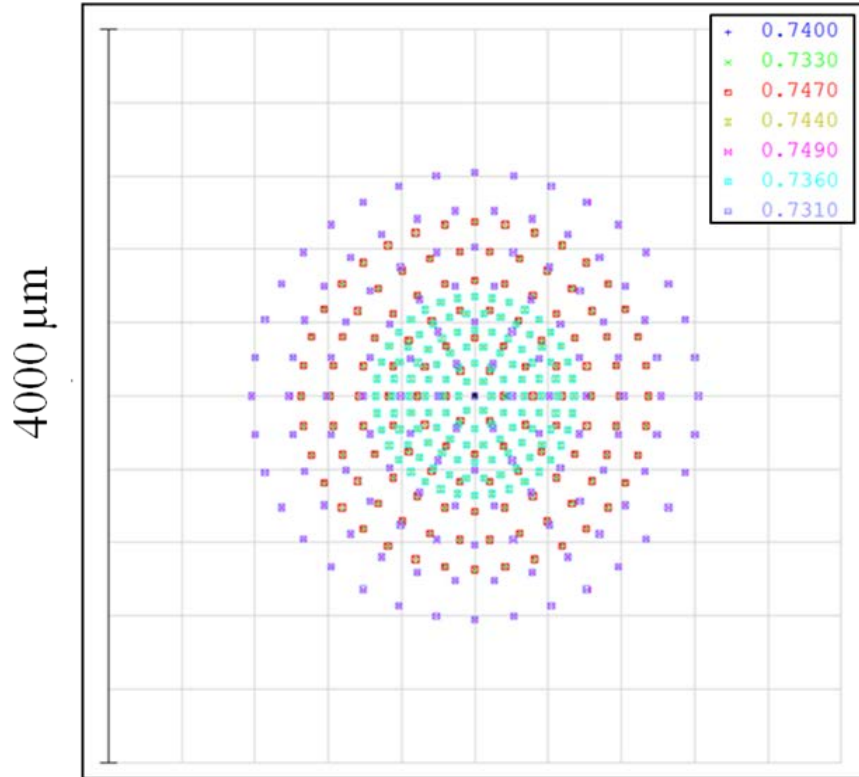


Figure 33. Polychromatic Primary Sieve Focal Spot Prediction. This Zemax-produced figure shows what a polychromatic image of a point source made by the primary photon sieve should look like in the image plane. Seven wavelengths (731 nm, 733 nm, 736 nm, 740 nm, 744 nm, 747 nm, and 749 nm) were considered. The outer ring represents light from the extreme wavelengths. Because the predicted Airy disk at 740 nm is $18\text{ }\mu\text{m}$ in diameter, it is evident that this polychromatic spot is far from diffraction-limited.

Without discussion yet of how the enhancement was achieved, but for comparison purposes, Fig. 34 shows a corrected focal spot over the same 18-nm range. Note that only the extreme and center wavelengths are pictured. Not only is the spot pattern much tighter (nearly $12\text{ }\mu\text{m}$), most of the light is contained near the 3- μm Airy disk (the RMS diameter is about $5\text{ }\mu\text{m}$). The ring pattern in this picture also more closely resembles what would be expected for a diffraction-limited point source and indicates that it is

possible to achieve such performance over an extended bandwidth by employing secondary optics.

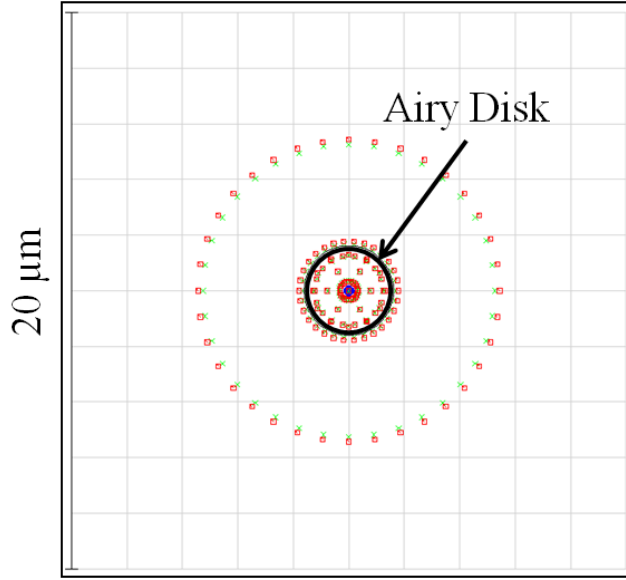


Figure 34. Corrected Focal Spot. A focal spot much closer to that expected for a diffraction-limited optic can be achieved over a wide spectral band by adding secondary optics to correct the wavefront aberration. This figure depicts an RMS diameter (5 μm) very close to the Airy disk diameter (3 μm) over an 18-nm range.

Chromatic Aberration.

Theoretical axial chromatic aberration was also predicted using both geometric analysis and Zemax. First, Eq. 8 can be rewritten to yield the expected focal length of the primary sieve at an off-design wavelength (λ_2),

$$f_{\lambda_2} = \frac{R_{SIEVE}^2 - \frac{n_{SIEVE}^2 \lambda_2^2}{4}}{2n_{SIEVE} \lambda_2}, \quad (45)$$

where $R_{SIEVE} = 0.05$ m and $n_{SIEVE} = 3376$ rings. Noting that $f_{\lambda_1} = 500.04$ mm (the design focal length of the sieve at 740 nm), the ACA between λ_2 and 740 nm can be determined by first applying Eq. 45 and then using Eq. 20. Table 2, Column 7 lists these

predictions which reveal possible ACA up to 2.72 mm across an 8-nm bandwidth.

Comparison to experimental measurements is presented later.

Additionally, Zemax can also be used to predict ACA. As the wavelength is adjusted, the software will provide an image location ($s_{i\lambda_2}$) based on marginal ray height for a point source 1 m away from the sieve. Using the imaging equation from geometric optics,

$$\frac{1}{f_{\lambda_2}} = \frac{1}{s_{o\lambda_2}} + \frac{1}{s_{i\lambda_2}}, \quad (46)$$

where $s_{o\lambda_2} = 2f_{\text{SIEVE}}$, the adjusted focal length (f_{λ_2}) can be determined and inserted into Eq. 20 to determine ACA (note that these values are not shown in Table 2).

Wavefront Error.

The final primary sieve aberration explored using Zemax was peak-to-valley wavefront error. Fig. 35 depicts simulations of the wavefront passed by the sieve at 736 nm, 740 nm, and 744 nm, respectively. As expected, the middle (740-nm) wavefront shows no aberration while the outer cases exhibit approximately 18.35 and 18.15 waves of aberration. These values well-exceed the diffraction-limited condition of 0.25 waves and therefore predict a highly-aberrated wavefront and a poor image. The predicted wavefront error at all seven discrete wavelengths is presented later in Table 7, Row 5.



Figure 35. Primary Wavefront Depiction Prediction at Various Wavelengths. The Zemax-predicted wavefront is shown at 736 nm, 740 nm, and 744 nm (left to right) after passing through the primary photon sieve. The outer wavefronts each show approximately 18 waves of aberration and therefore indicate wavelength-specific performance degradation and a limited bandwidth.

Primary Experimental Results

Focal Spot and Chromatic Aberration.

The previous section noted methods to predict ACA. Experimental measurements were taken that show close agreement with these simulations. Using the setup depicted in Fig. 28, the image location (translation stage micrometer setting) was recorded at each wavelength between 736 nm and 744 nm (see Table 2, Column 2). The difference between this location and that at 740 nm (Δs_i) was calculated (see Table 2, Column 3).

Table 2. Primary Photon Sieve Chromatic Aberration Focal Spot Measurements

λ (nm)	Micrometer Setting (mm)	Δs_i (mm)	f_{EFF} (mm)	Measured ACA (mm)	ACA Error (mm)	Predicted ACA (mm)	Δ ACA (mm)
736	19.96	10.91	502.75	2.71	0.10	2.72	0.01
737	17.15	8.10	502.06	2.02	0.09	2.04	0.02
738	14.32	5.27	501.35	1.31	0.09	1.36	0.04
739	11.70	2.65	500.70	0.66	0.09	0.68	0.02
740	9.05	0.00	500.04	0.00	0.00	0.00	0.00
741	6.26	-2.79	499.34	-0.70	0.09	-0.68	0.02
742	3.80	-5.25	498.72	-1.32	0.09	-1.35	0.03
743	1.24	-7.81	498.08	-1.96	0.10	-2.02	0.06
744	-1.40	-10.45	497.41	-2.63	0.10	-2.69	0.07

Note that the point source (spatial filter) was placed such that $s_0 = 2f_{\text{SIEVE}} \approx 1$ m and was constant throughout the measurements. Furthermore, the sieve was designed such that, at 740 nm, when $s_0 = 2f_{\text{SIEVE}}$, $s_i = 2f_{\text{SIEVE}}$. Accordingly, the difference in the image location of an off-design wavelength (λ_2) and that at 740 nm is given by

$$\Delta s_i = s_{i\lambda_2} - s_{i\lambda_1} = s_{i\lambda_2} - 2f_{\text{SIEVE}}. \quad (47)$$

Applying this information, Eq. 46 becomes

$$\frac{1}{f_{\lambda_2}} = \frac{1}{s_{0\lambda_2}} + \frac{1}{s_{i\lambda_2}} = \frac{1}{2f_{\text{SIEVE}}} + \frac{1}{2f_{\text{SIEVE}} + \Delta s_i}, \quad (48)$$

and, when solved for f_{λ_2} and combined with Eq. 20, yields the desired expression for

ACA:

$$\text{ACA} = \Delta f = f_{\lambda_2} - f_{\text{SIEVE}} = \frac{f_{\text{SIEVE}}}{4f_{\text{SIEVE}} + \Delta s_i}. \quad (49)$$

This ACA (based solely on measured Δs_i) was tabulated and compared to the predicted values (see Table 2, Columns 5 and 7). In all cases, the measured ACA was within 0.1 mm of the predicted ACA. Figs. 36 and 37 graphically illustrate the high agreement between the measured and predicted values.

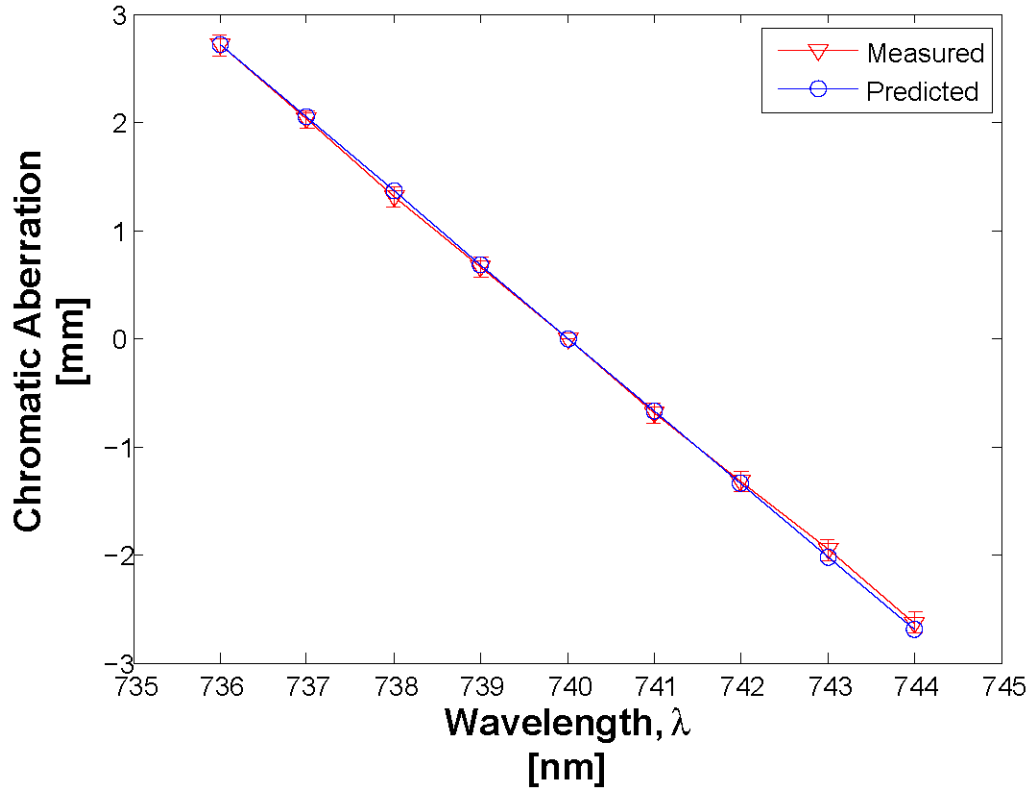


Figure 36. Plot of Measured versus Predicted ACA. The triangles represent the experimentally-measured data listed in Table 2, Column 5 while the circles represent the ACA values predicted using Eqs. 20 and 45 (see Table 2, Column 7).

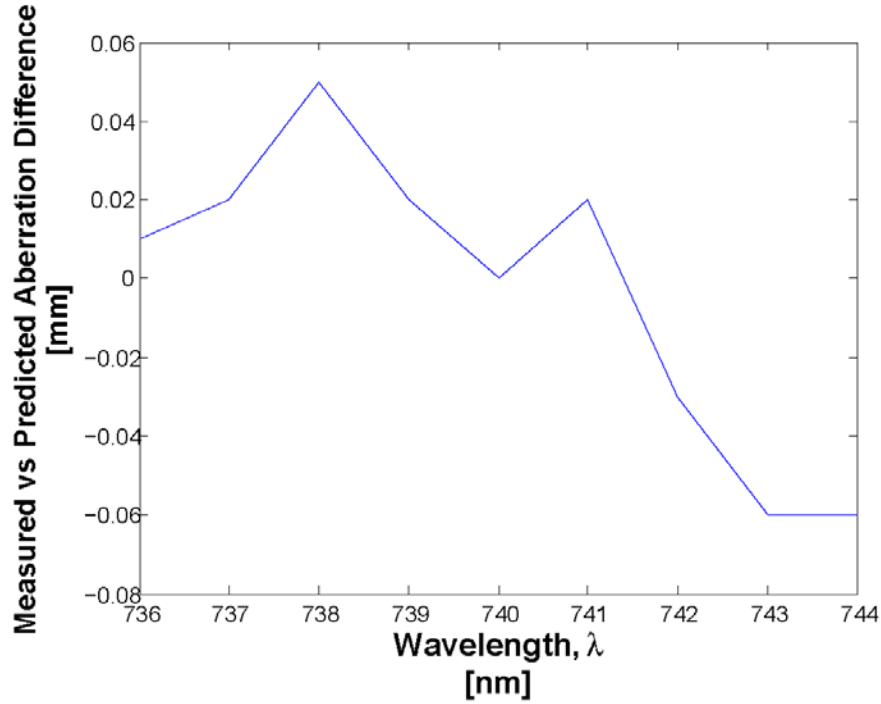


Figure 37. Difference in Measured versus Predicted ACA. This figure is a plot of Table 2, Column 8 versus wavelength and shows that the difference between the experimentally-determined and predicted ACA values is very small (< 0.1 mm).

One source of error in experimentally measuring Δs_i was pinpointing an exact location of the in-focus spot. In Fig. 38, the focused image of the 740-nm spot is depicted (Left). As the laser was tuned by only a small amount, the image became increasingly distorted.

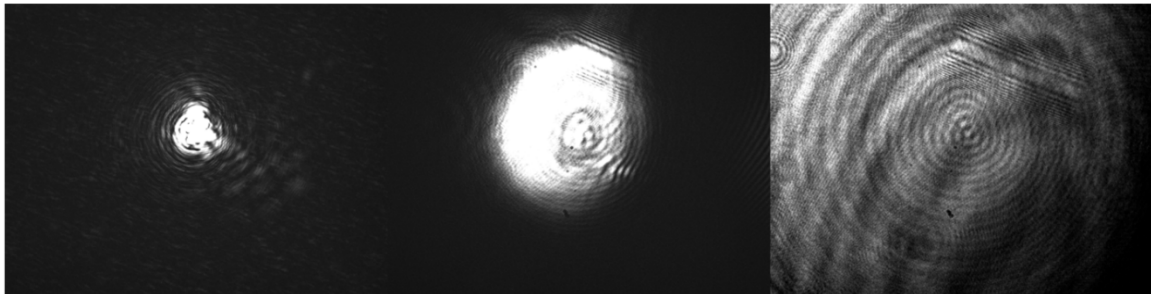


Figure 38. Polychromatic Focal Spot Distortion. The focal spot was imaged at 740 nm, 739 nm, and 736 nm (left to right) in the 740-nm image place. The 740-nm image is the best while the image becomes significantly distorted as the laser is tuned away from 740 nm.

As such, around the focal spot, it was difficult to visualize the smallest and least-distorted image precisely, and a range of possible focal spot values was determined.

First, to account for the error in the reference (740-nm) spot position measurement, three different measurements were taken and an average value (u) calculated. The difference between this average and the furthest measurement was used as the error: $\sigma_u = 0.2$ mm.

Second, to account for the error in the spot position measurements at other wavelengths (v), the edges of what could be considered the focus were measured. Specifically, these limits were determined by when the spot began to expand in either the horizontal or vertical direction. Of the six measurements made, the worst-case offset was used as the error in this quantity: $\sigma_v = 0.325$ mm. Because Δs_i is simply the difference in focused spot location measurements ($\Delta s_i = v - u$), the error in Δs_i is

$$\sigma_{\Delta s_i} = \sqrt{\left(\frac{\partial \Delta s_i}{\partial u}\right)^2 \sigma_u^2 + \left(\frac{\partial \Delta s_i}{\partial v}\right)^2 \sigma_v^2} = \pm 0.38 \text{ mm} . \quad (50)$$

To calculate the total error in ACA, the error in Δs_i had to be propagated through Eqs. 20 and 48. See the Appendix for a full set of calculations, but in general,

$$\text{ACA} = \frac{s_{0\lambda_2}^2 \Delta s_i - s_{0\lambda_2} \Delta s_i f_{\text{SIEVE}} + s_{0\lambda_2}^2 f_{\text{SIEVE}}}{s_{0\lambda_2}^2 + s_{0\lambda_2} \Delta s_i - \Delta s_i f_{\text{SIEVE}}} - f_{\text{SIEVE}} . \quad (51)$$

Note that this expression differs from Eq. 49 because $s_{0\lambda_2}$ was left as a variable (even though it is assumed to be $2f_{\text{SIEVE}}$ for numerical calculations) due to small uncertainty in the exact placement of the point source relative to the sieve that must be accounted for in the total error. This total error is computed by

$$\sigma_{\text{ACA}} = \sqrt{\left(\frac{\partial \text{ACA}}{\partial s_{0\lambda_2}}\right)^2 \sigma_{s_{0\lambda_2}}^2 + \left(\frac{\partial \text{ACA}}{\partial \Delta s_i}\right)^2 \sigma_{\Delta s_i}^2} , \quad (52)$$

where $\sigma_{s_0\lambda_2}$ was measured to be approximately 5 mm. The error ranges from 0.09 mm to 0.10 mm and is reflected by the error bars in Fig. 36 and listed in Table 2, Column 6.

A second check of the sieve performance was determination of whether the observed focal spot size was consistent with theoretical predictions. For a diffraction-limited system, the spot size is given by (21:468-470):

$$d_f = \text{Focal Spot Diameter} = 2.44 \times \frac{\lambda}{D} (2f). \quad (53)$$

Fig. 39 shows an enlarged picture of the actual spot magnified from the image plane by a 20x microscope objective.

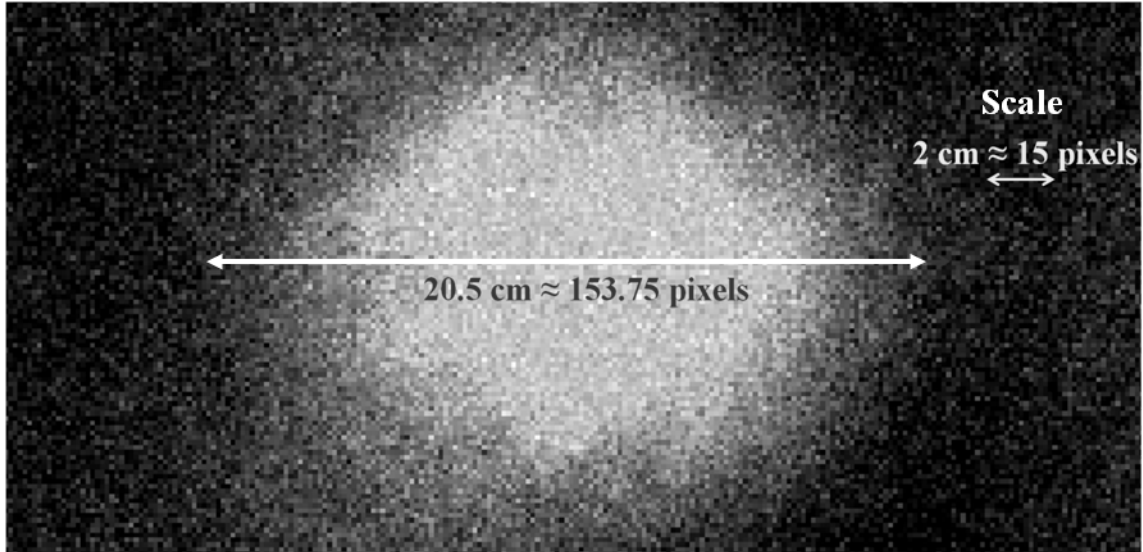


Figure 39. In-focus Spot Measurement. The depicted spot contains approximately 153.75 pixels. At $5.4 \mu\text{m}$ per pixel, the spot diameter measures about $830 \mu\text{m}$ which is close to the diffraction-limited prediction of $846 \mu\text{m}$.

Using Eq. 53 and adjusting for magnification, the diameter of a diffraction-limited spot on the camera should be approximately $846 \mu\text{m}$. Several measurements were taken using the photo in Fig. 39 in which the number of pixels across the spot was estimated and multiplied by the camera pixel size, $5.4 \mu\text{m}$. Determining the first minimum in the

photo precisely was difficult, yielding diameter estimates ranging from 775 μm to 944 μm . The most confident measurement (depicted in the figure) suggests an Airy disk diameter of 830 μm which is close to the theoretical value. In any case, however, the predicted value falls within the range of measured values, indicating sieve performance at least close to diffraction limited.

Lastly, Fig. 40 is an image taken at the USAFA of the spot produced by the primary sieve. This high quality image shows an Airy pattern consisting of a solid center surrounded by a lower-intensity ring. Furthermore, the image displays a fairly round center. While no computational measurements were performed using this particular image, it is included because of its basic agreement with expectations of how the image of a diffraction-limited point source should appear (21:469).

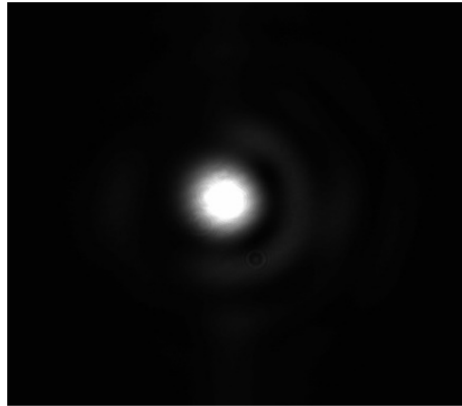


Figure 40. Primary Photon Sieve Spot Image at 731 nm. This image conforms highly to expectations of how a diffraction-limited point source should appear. The image was taken at 731 nm because that was the position of best focus due to the misplacement of the sieve in relation to the point source at the USAFA (see Chapter III).

Imaging.

To test the imaging capability of the primary sieve, an image was made of a resolution test target (again according to the method illustrated in Fig. 28). Fig. 41 shows images formed while using a spinning diffuser at two wavelengths while Fig. 42 shows a

comparison between images taken with and without the diffuser. The distortions apparent in Fig. 42 (Right) are the result of speckle which resulted because a coherent laser was used to illuminate the chart, causing interference and degradation (20:40-41).

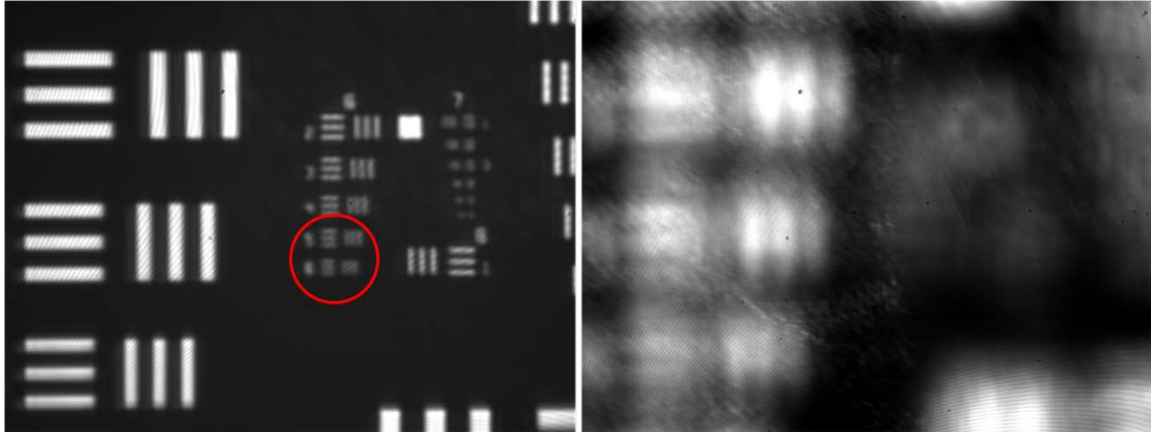


Figure 41. Diffraction-Limited Image of Resolution Chart from Primary Sieve. Left: The red circle indicates the smallest resolvable group. A group is identified by its column and row number. Note that the “6-1” group is actually at the bottom of the column labeled “7.” The “6-5” to “6-6” groups should be resolved for a diffraction-limited system and are resolved in the figure. Right: A picture of the same area was taken at 739 nm. None of the groups are resolvable, showing a very narrow diffraction-limited range.

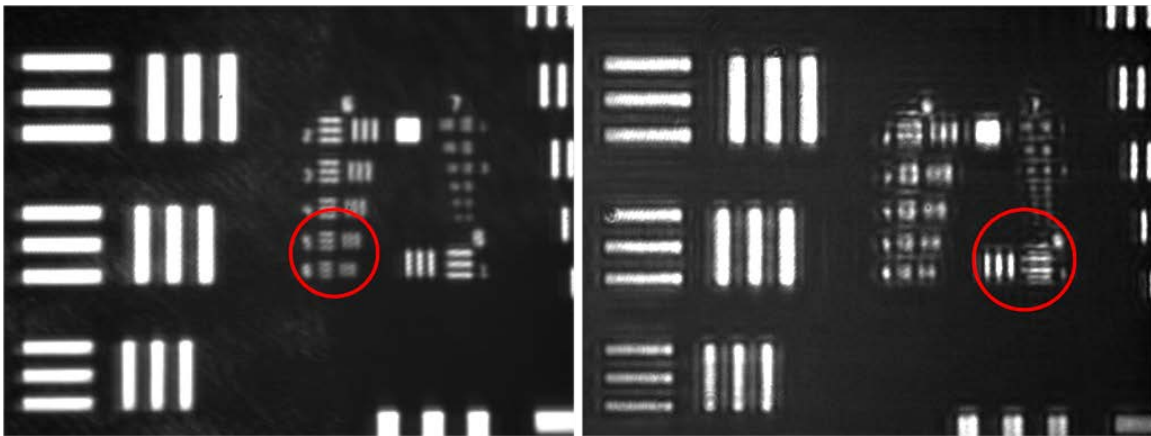


Figure 42. Image of Resolution Chart with and without Diffuser. The left image is of the 6/7 columns of a resolution target at 740 nm using a diffuser. The right image is of the same area without a diffuser. The resolution in the right image is not as good due to the effects of laser speckle.

The red circles in each picture indicate the smallest resolvable grouping. A grouping is resolved when the lines in both directions can be distinguished and the number of lines determined (35:3). In order to gauge sieve performance, it was necessary

to determine theoretically which grouping should be resolved for a diffraction-limited device. The Rayleigh criterion for resolution is given by

$$\delta = \text{Min Resolvable Image Separation} = 1.22 \times \frac{z_i \lambda}{D} \quad (54)$$

where $z_i = 2f$ is the image distance and D is the diameter of the optic. Using the parameters unique to this setup, $\delta = 0.009028$ mm. This result implies that to resolve the bars, the centers need to be approximately $9 \mu\text{m}$ apart. In other words, the width of a line-space pair in the smallest resolvable group would be $9 \mu\text{m}$. Because the bars in each grouping are the same width as the space between them, each bar in the smallest resolvable group would be about $4.5 \mu\text{m}$. From Table 3, it is evident that $4.5\text{-}\mu\text{m}$ bars would occur between groups 6-5 and 6-6. A diffraction-limited system should therefore be able to resolve those lines. This is the case in Fig. 41, so the sieve is diffraction-limited at 740 nm. Speckle is likely contributing to the blurring in Fig. 42 (Right) which does not show diffraction-limited performance. The smallest resolvable group is 6-1.

Table 3. Resolution Chart Data (35)

Block		Lines/mm	Line Thickness (μm)
3	1	8.00	62.50
	5	50.80	9.84
5	6	57.02	8.77
	1	64.00	7.81
6	2	71.84	6.96
	3	80.63	6.20
	4	90.51	5.52
	5	101.59	4.92
	6	114.04	4.38
	7	128.00	3.91
	1	128.00	3.91

As a quick check of the ACA measurements made using the focal spot positions, the experiment was repeated using the number “3” column header on the resolution chart

without a diffuser (one was not available at the time of the measurement). The in-focus position of the number “3” seemed easier to visually determine than the spot position. The same procedure employed for spot ACA measurements (described in the previous section) was again utilized. These measurements were taken from 741 nm to 744 nm, and the values obtained are listed in Table 4.

Table 4. Primary Photon Sieve Chromatic Aberration Resolution Chart Measurements

λ (nm)	Micrometer Setting (mm)	Δs_i (mm)	f_{EFF} (mm)	ACA (mm)
740	18.26	0.00	500.04	0.00
741	15.77	-2.49	499.42	-0.62
742	12.84	-5.42	498.68	-1.36
743	10.14	-8.12	498.00	-2.04
744	7.00	-11.26	497.21	-2.83

Fig. 43 shows a comparative plot between the values for ACA determined using spot measurements and those obtained using the resolution target. The proximity of the lines indicates good agreement between the methods and consistency of results.

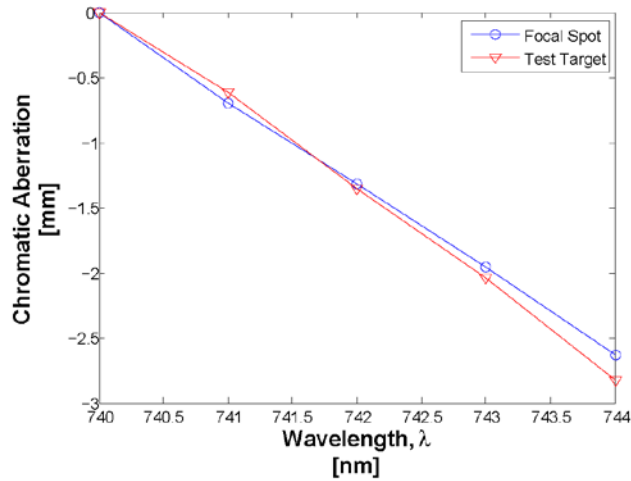


Figure 43. Comparative ACA Measurement. The circles represent ACA measurements made by comparing spot (point source) image locations. The triangles represent ACA measurements made by comparing in-focus locations of the number “3” on the resolution target.

Interferometry (Wavefront Error).

Interferometry testing was conducted at the USAFA. Using the procedure illustrated in Fig. 30, the primary photon sieve was illuminated with a point source at 731 nm. The transmitted beam was collimated and interfered with a theoretically-unaberrated reference beam (also at 731 nm) to produce the fringe pattern in Fig. 44.

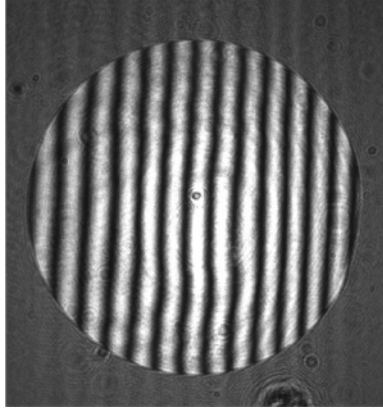


Figure 44. Interferogram of Primary Sieve with a Reference Beam. This figure is an image of the interference between an unaberrated reference beam and the aberrated wavefront transmitted by the sieve.

As noted, the sieve was designed to focus 740-nm light at a distance $2f = 1$ m from the optic. During testing setup, the distance between the source and the sieve was inadvertently changed from 1 m, thereby introducing off-wavelength aberration in the system. Because the optics were already aligned properly, however, it was decided that the laser would simply be tuned to the wavelength of best performance (731 nm in this case) to measure the aberration of sieve.

Using fringe analysis software, the peak-to-valley wavefront error was calculated to be 0.2227 waves (adjusted to 740 nm performance). While this value is much higher than the predicted value of 0 (a perfect optic), it is below the diffraction-limited value of 0.25 waves. This result is important because it demonstrates that the primary photon sieve functions properly and is diffraction-limited. Any further error in the resulting

image is therefore due to other factors, such as chromatic aberration. Care was taken during setup to try and minimize aberration due to alignment and positioning of the optics and thereby eliminate sources of aberration other than dispersion.

Efficiency.

While not directly linked to determining chromatic aberration, an efficiency measurement was taken to further characterize the primary sieve. The power incident on the sieve was calculated and compared to the power measured in the in-focus spot. The Ti:Sapphire laser was pumped at 8 W, giving an expected output power of approximately 0.8-1.2 W which was subsequently decreased by a 50-50 beam splitter, two mirrors, and a spatial filter. A ThorLabs D3MM power meter was used. The measurement surface had a diameter of approximately 9 mm. When placed in front of the sieve, the meter registered 10.7 ± 0.5 mW of incident power. Assuming that the sieve was illuminated evenly, the total power incident on the sieve was 330.3 mW using the middle of the range (2). The meter was transferred to the image plane where 10.1 ± 0.6 mW of power was measured. Using these values, the sieve efficiency was calculated to be 2.8-3.4% with a median efficiency of 3.1%. Note that this value may be high because no filter (to block any additional light diverging from the sieve) was used while making the second power measurement, but it is near the expected value of 3-4% (2).

Zemax Modeling and Optimization

Optimization.

As discussed in Chapter III, the Zemax RWCE optimization routine was used to determine both a focal length and wavelength for the secondary corrector. This routine

minimizes wavefront error over the specified bandwidth. During modeling, different wavelength ranges were entered into the software, optimization performed, and the wavefront analyzed. If the error exceeded the diffraction-limited value (0.25λ), the bandwidth was adjusted and the optimization performed again.

As a side note, Zemax offers an optimization routine (AXCL) based on the axial image distance between two wavelength values (39:280). This routine seemed promising because the axial difference in focus between the colors of a polychromatic source was what the correction scheme was being designed to minimize. What was determined, however, was that while the predicted value of Δs_i using the AXCL function was approximately equal to the value achieved using the RWCE function, the wavefront aberration was much higher using the former and well beyond the diffraction limit (see Table 8). As such, the AXCL optimization routine was not used.

Design Comparisons.

Multiple corrector designs were investigated. During the process, several factors had to be considered when selecting a design. First, the divergent light transmitted by the secondary had to be collected and focused to form an image. A camera lens was used for this task and had to have a diameter large enough to gather all of the diverging light. The farther away from the corrector that the lens was placed, the larger the lens would need to be. It was determined that a reasonably-priced Nikon f/1.4 lens could be purchased. The diameter of this lens therefore limited the largest diameter of the beam incident on the second optic to approximately 35 mm.

Working backwards through the optical system, this maximum beam size drove a second parameter: the focal length of the lens used to collimate the light from the primary

sieve. Because the collimating lens was placed at a distance equal to its focal length from the primary sieve's image plane, a larger focal length would result in a larger beam. Consequently, the limit on beam size resulted in limits on the collimating lens focal length. As an additional note, the type of collimating lens (achromatic doublet) was selected such that it did not introduce significant chromatic aberration into the imaging system (see Ref. 22). Again, availability and cost of these higher-quality lenses were factors considered in design.

Table 5 lists three lenses determined acceptable for collimating the light in this correction scheme and shows the optimized corrector parameters (wavelength and focal length) determined by Zemax when including these lenses. When using a collimating lens with a 220-mm focal length, for example, Zemax suggested that the corrector be designed to operate at 739 nm with a 23-mm focal length to achieve optimal wavefront performance across a particular bandwidth (which will be discussed later). The last row lists the beam diameter at the secondary, which is less than the required 35 mm in all cases. Only the first two lenses, an OptoSigma 026-1495 220-mm achromatic doublet and a ThorLabs AC508-300-B 300-mm near-IR achromat, were purchased for experimental testing.

Table 5. Optimized Design Parameters

	OptoSigma 220 mm Collimator (A)	ThorLabs 300 mm Collimator (B)	ThorLabs 350 mm Collimator (C)
Required Wavelength (nm)	739	739	739
Required Focal Length (mm)	23.077	43.762	59.959
Required Diameter (mm)	22.026	29.964	34.936

Final System Design.

Using the Zemax-determined parameters for lenses A and B in Table 5, corrector sieves were designed and fabricated in the same way as the primary. Table 6, Columns 2 and 4 list the parameters of these devices. As discussed in Chapter III, because these sieves were small in diameter, every other ring near the edges of the sieves was skipped. As a result, the total area covered by holes (and therefore the total transmission of the sieve) was decreased to well-below the desired 50% (see Table 6, Row 14).

Table 6. Corrector Element Comparison

Element	A-SIEVE	A-FZP	B-SIEVE	B-FZP
Wavelength (nm)	739	739	739	739
Focal Length (mm)	23.077	23.077	43.762	43.762
Diameter (mm)	22.999	22.999	29.999	30.000
Total Rings	2195	2606	2187	2739
Transition Ring	728	1550	978	2082
Total Holes	28795151	N/A	34670938	N/A
Area Covered By Standard Hole/Ring Size (%)	33.12	59.44	44.67	75.98
Maximum Hole/Ring Thickness (μm)	70.64	46.17	97.06	63.44
Minimum Hole/Ring Thickness (μm)	1.50	1.50	1.50	1.50
nMax Lateral Hole Separation (μm)	1.57	N/A	1.57	N/A
nMax Radial Hole/Ring Separation (μm)	1.81	1.81	3.04	3.04
Outer Ring d/w	2.02	N/A	1.40	N/A
Area Covered (%)	18.84	42.90	19.44	41.54

Due to uncertainty as to whether the Ti:Sapphire would have enough power to allow correction measurements with such low transmission, a FZP with the same parameters as each sieve was also constructed. Because the width of the FZP rings equals the width of the underlying Fresnel zone (and not scaled bigger like the holes of a photon sieve), more of the FZP could be covered before outer rings had to be skipped.

Consequently, the zone plates allowed higher transmission (about double). The parameters of these equivalent zone plates are listed in Table 6, Columns 3 and 5.

Secondary Modeling Predictions

Wavefront Error.

Using Zemax, the performance of each of the correctors associated with the various collimating lenses listed in Table 5 (labeled A, B, or C) was simulated to determine both predicted wavefront aberration as well as focus and image characteristics. Table 7 lists the predicted wavefront error for each corrector at each of the seven considered wavelength values. A green (light gray in grayscale) box indicates that the error is well-below the diffraction limit of 0.25 waves. A yellow (white) box indicates that the system is approaching the diffraction limit (yet still below it) while a red (dark gray) box indicates that the limit has been exceeded. The last column lists the bandwidth across which the corrector should theoretically compensate for the primary aberration. Corrector A (the 220-mm collimator) allows diffraction-limited performance across the target 8-nm range.

Recall that it was discussed in Chapter I that the efficiency of the corrector was not considered when determining this target. The decrease in transmitted energy from the secondary would clearly necessitate a higher starting bandwidth. What is evident from Table 7, however, is that a larger bandwidth can be achieved by simply increasing the focal length of the collimating lens. As such, this scheme is adaptable (to the extent that it fits within the engineering constraints of the application). Furthermore, the scheme should provide correction over a desired bandwidth limited only by other factors already

covered (incident beam size, space, or element required to collect the divergent light, for example). The last row in Table 7 lists the uncorrected wavefront aberration, clearly indicating necessity of the secondary optics in any imaging application.

Table 7. Predicted Peak-to-Valley Wavefront Error (Waves)

λ (nm)	731	733	736	740	744	747	749	$\Delta\lambda$ (nm)
A	0.5572	0.4317	0.2446	0.0033	0.2495	0.4375	0.5645	8
B	0.3167	0.2443	0.1406	0.0081	0.1381	0.2421	0.3163	14
C	0.2387	0.1852	0.1093	0.0069	0.1066	0.1850	0.239	18
Primary	41.5696	32.2434	18.3495	0.000	18.1517	31.6377	40.5681	N/A

Fig. 45 depicts Zemax simulations of the wavefront at 736 nm, 740 nm, and 744 nm after passing through the primary sieve-secondary combination (using Corrector A). For comparison, Fig. 35 shows the wavefront at the same three wavelength values but does not include correction optics. Note an apparent contradiction between the figures. In Fig. 35, Zemax predicted an unaberrated wavefront at 740 nm while in Fig. 45, there is clearly some error (approximately 0.003 waves). The small aberration is likely a result of multiple wavelength values being considered during optimization and the resultant corrector design wavelength (739 nm).

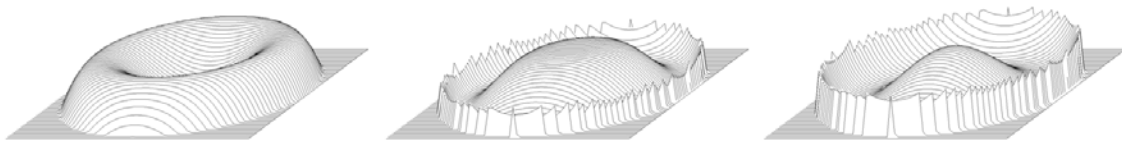


Figure 45. Corrected Wavefront Depiction at Various Wavelengths. The Zemax-predicted wavefront is shown at 736 nm, 740 nm, and 744 nm (left to right) after passing through the primary photon sieve, a 220-mm collimating lens (Corrector A), and the corrector. The outer wavefronts each show approximately 0.25 waves of aberration while the aberration at the center wavelength is minimal although not zero. The non-zero value at 740 nm may be due to a tradeoff between optimal performance at the primary wavelength and acceptable performance at peripheral wavelengths.

Focal Spot and Chromatic Aberration.

As was the case when modeling the primary sieve, Zemax was used to determine the combined system (primary and secondary) image locations using light of various wavelengths. The image distances were compared to the reference distance at 740 nm. The Zemax-predicted values are listed in Table 8. Note that the last row lists the values modeled for the primary sieve alone, showing a clear improvement with correction. To understand the color scheme in Table 8, a discussion of the idea of “depth of focus” is warranted.

Fischer defines depth of focus as “the amount of image defocus which corresponds to [the condition when]...the optical path difference between the real wavefront...and a reference wavefront...is one-quarter of the wavelength of light” (16:58). Because $ACA = \Delta f$, ACA can be viewed in terms of depth of focus by determining how much change in focus results in 0.25λ wavefront aberration. Δf , in turn, can be determined by measuring Δs_i (see Eq. 49, for example). In this particular case, however, the corrected system involved three additional optics, making calculation of Δf much more complicated than with the primary sieve alone. As such, the colors in Table 8 correspond to the change in image location that corresponds to 0.25λ (see Table 7) and consequently exceeds the depth of focus. Green (light gray) indicates Δs_i below the threshold, yellow (white) indicates the limit is approaching, and red (dark gray) annotates Δs_i that has caused a focal spot to exceed the depth of focus at the design wavelength. Note that the anticipated difference in Δs_i between the corrected versus uncorrected systems is approximately two orders of magnitude.

Table 8. Predicted Change in Image Location (mm)

Wavelength (nm)	731	733	736	740	744	747	749
Corrector A	0.071	0.055	0.031	0.000	-0.031	-0.054	-0.069
Corrector B	0.134	0.105	0.059	0.000	-0.059	-0.103	-0.131
Corrector C	0.185	0.143	0.081	0.000	-0.081	-0.141	-0.181
Primary	24.931	19.284	10.929	0.000	-10.695	-18.568	-23.747

Fig. 34 already illustrated the impact a corrector should have on a focal spot size and appearance. Fig. 46 illustrates another effect that is not as relevant to measuring ACA but is an interesting observation regarding the aberration nonetheless. The figure shows the focal spot at various locations (spaced by 5 μm) along the optical axis. In essence, it represents what the focal spot would look like from an observer traveling along the axis starting prior to the focus and passing through it to the other side. As expected, the focal spot size increases to the left and right of the focus. What is interesting, however, is that the increase on either side is due to light of different wavelengths. On the right side, the expansion is primarily seen at 744 nm while on the left side, it is a result of the 736-nm light.

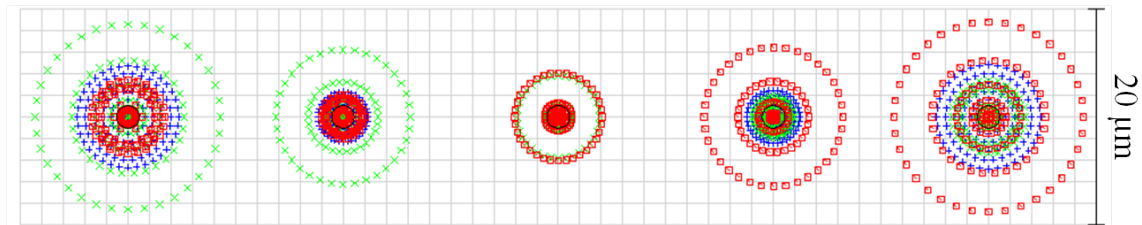


Figure 46. Along-Axis Corrected Focal Spot Predictions. These focal spot “snapshots” are separated by 5- μm increments along the optical axis with the middle image representing the actual focus. The red dots (outer ring in the right spot) represent 744-nm light, and the green dots (outer ring in left spot) represent 736-nm light.

Secondary Experimental Results

Zone Plate Characterization.

Corrector A-FZP (the zone plate designed to work with the 220-mm collimating achromat) was used for the correction effectiveness measurements. During testing, it was suspected that elements of the optical system were misaligned or that the corrector was not functioning fully as expected, leading to a degraded final image (see Figs. 51 and 54). The system alignment was checked and determined not likely to be the cause of the main image problems. The corrector, therefore, was suspected and independently tested by illuminating the FZP with a collimated beam at 739 nm (the design wavelength of the corrector). An adjustable aperture was placed as close as possible (approximately 3 cm) in front of the FZP in order to adjust the effective diameter of the device. This procedure essentially permitted testing of only the central portion of the FZP. Fig. 47 illustrates the focal spot formed by the FZP at various aperture positions. The image on the left was taken with the aperture fully closed (a diameter of approximately 2 mm); the image on the right was taken with the aperture fully open (a diameter of approximately 2 cm); and the central image was taken with the aperture positioned in between.

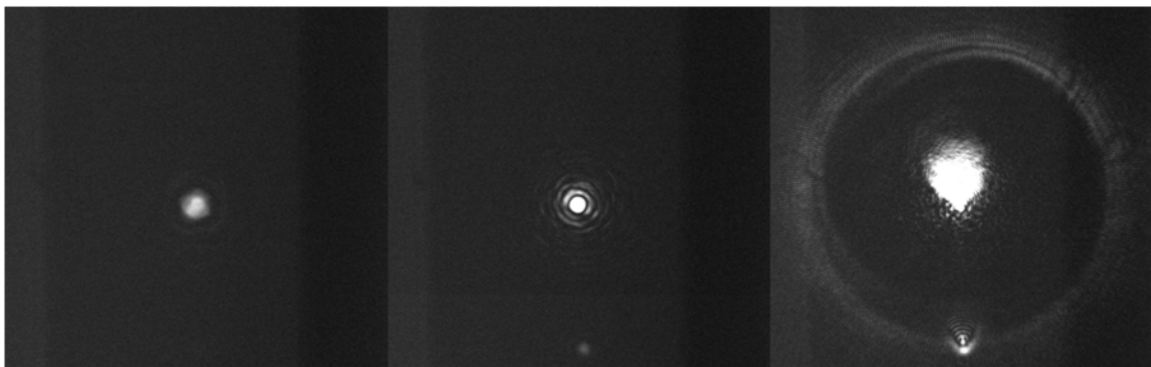


Figure 47. Corrector A-FZP Focal Spot. These images of the focal spot (formed by the $f = 23$ mm FZP corrector) were taken with an adjustable aperture (in front of the FZP) fully closed to approximately 2 mm (left), fully open to approximately 2 cm (right), and in between. The incident 739-nm light was collimated.

Fig. 47 seems to indicate that as more of the FZP is illuminated, the spot image degrades and appears to show a significant amount of aberration when the majority of the corrector is being used. For comparison, the resolution chart was imaged and showed similar behavior. Fig. 48 shows images of the test target with the aperture fully open (Right) and slightly open but not fully closed (Left). Note that when the aperture is fully open, there appears to be a “smearing” effect toward the upper left of the image. In each case, the resolved line grouping seems to be the same, but the image quality is greatly enhanced as the aperture is closed. One additional note is that, under the magnification used to form the images in Fig. 48, it was not possible to observe the expected least-resolvable line group (in the “7” column) to completely quantify the FZP performance.

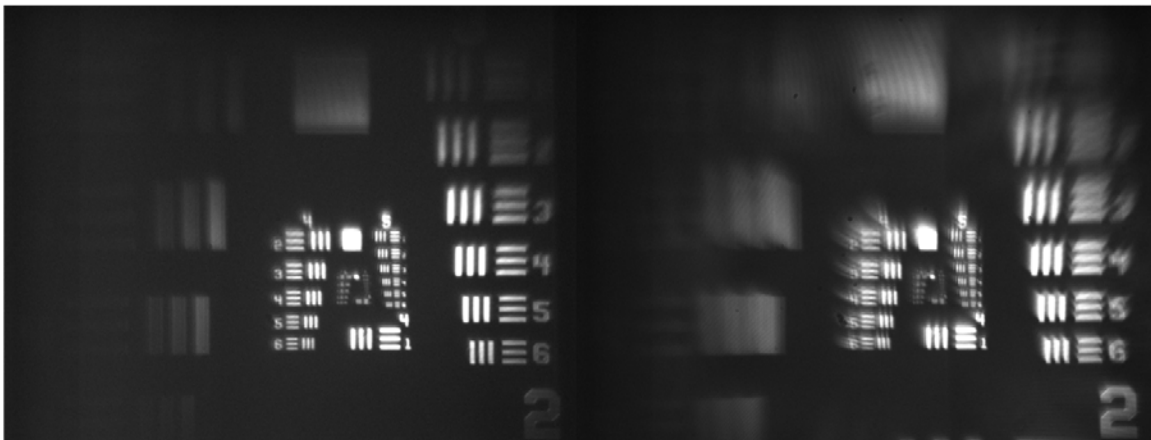


Figure 48. Corrector A-FZP Resolution Chart. These images of the resolution chart were formed by the $f = 23$ mm FZP corrector and were taken with an adjustable aperture in front of the FZP slightly open (left) and fully open (right). The incident 739-nm light was collimated.

These observations are important, however, as they imply that the outer portions of the FZP may not be performing properly, possibly due to design or printing error. The latter is unlikely as the central portion seems to function adequately (and the primary sieve, fabricated by the same process, performs well also). More likely then is that the design of the FZP (specifically the outer rings) needs to be reevaluated. Due to time

constraints, this investigation is left for future work, and the FZP was used in conjunction with an adjustable aperture to limit the illumination to the central 2-4 mm.

Because the system was limited to using the middle section of the FZP, the spot corresponding to this limit (Fig. 47, Left) was measured against the expected size for a diffraction-limited device. Using Fig. 49, the approximate spot diameter (to the first minimum) was measured ($d_f = 22 \text{ cm} \times 7 \text{ pixels/cm} \times 5.4 \text{ } \mu\text{m/pixel} \approx 831.6 \text{ } \mu\text{m}$). The diameter of the Airy disk for a diffraction-limited system (2-mm aperture, $f = 23 \text{ mm}$, $\lambda = 739 \text{ nm}$) was determined to be $20.8 \text{ } \mu\text{m}$ which, when magnified 35.6 times, gives an expected on-camera diameter of $740.5 \text{ } \mu\text{m}$. The measured spot is larger than expected; however, it was difficult to determine the first minimum of the observed Airy pattern, and the result is within 12% of the expected value. Consequently, the central portion of the FZP, while not definitively performing in a diffraction-limited manner, seems to be working well enough to conduct correction effectiveness analysis.

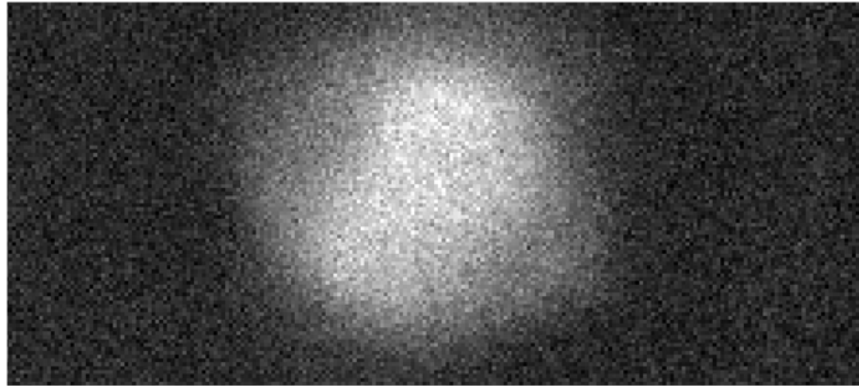


Figure 49. Corrector A-FZP Spot Measurement. The depicted spot contains approximately 154 pixels. At $5.4 \text{ } \mu\text{m}$ per pixel, the spot diameter measures about $832 \text{ } \mu\text{m}$. The magnified (36 \times) diffraction-limited predicted size is $741 \text{ } \mu\text{m}$.

Corrected Focal Spot and Chromatic Aberration.

The FZP was placed after the primary photon sieve to evaluate the correction effectiveness. With the available equipment, it would be difficult to directly measure ACA in the corrected system in the same way as was done with the primary. The predicted Δs_i for the corrected system (see Table 8) is much less than the error in measurement of Δs_i of the primary (see Eq. 50). Future work may be able to address this issue.

Thus, to analyze the corrector effectiveness, the system was set up according to Fig. 32 using the 220-mm collimating lens (Table 5, Collimator A) and Corrector A-FZP (Table 6). Note that the sieve-equivalent to this corrector was damaged beyond use and consequently not tested. Theoretically, the sieve and FZP should operate similarly with the benefit that the FZP offers additional transmission. The light from the spot imaged by the primary sieve was collimated by the lens, and the corrector was placed at the location where the primary sieve was imaged by the achromat (26.76 cm). The camera lens was then positioned at the maximum distance from the corrector such that the front of the lens could collect all of the divergent light from the FZP (approximately 1.4 cm).

In order to observe the corrected spot, it was first necessary to locate it. Because the system consisted of two diffractive elements, multiple spots (resulting from combinations of the various diffraction orders) were visible. Each element produced multiple orders, of which five from the primary were analyzed: the +1 and +3 (converging) orders, the 0 (undiffracted) order, and the -1 and -3 (diverging) orders. Combining these orders with the +1, 0, and -1 orders from the FZP, 15 combinations generated by the second optic were possible (2). Fig. 50 depicts the system geometry

along with the appropriate distances and focal lengths needed to apply the imaging formula (Eq. 46) and determine the spot locations. Table 9 lists where each order was expected to focus based on this geometry. The last column lists the imaging distance from the back vertex of the camera lens. Green (light gray) indicates spots believed to be observed; yellow (white) indicates spots that could be observed but were not (either by choice to not look for them or possibly due to low light); and red (dark gray) indicates virtual, unobservable spots. Note that the locations of the front and rear camera lens principal planes were estimated (17).

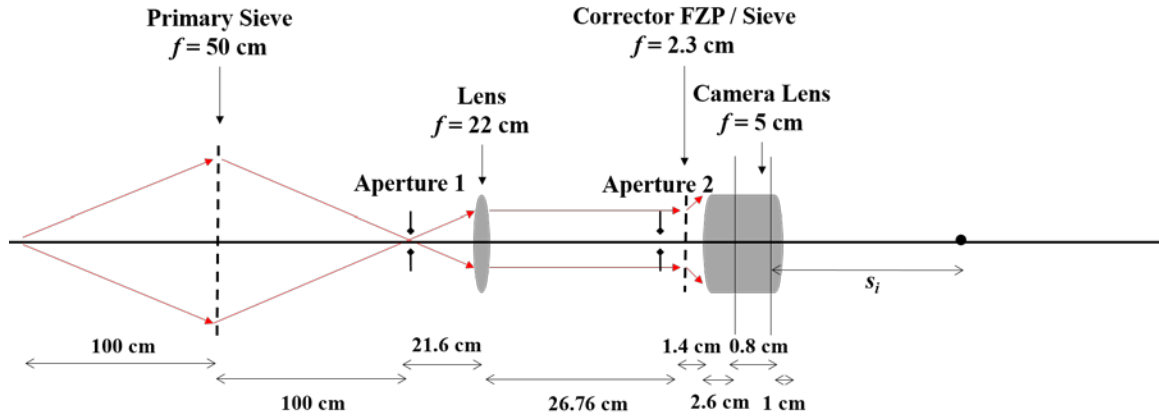


Figure 50. Corrected Focal Spot Location. A point source is imaged by the primary sieve. Aperture 1 was used to limit the light from the zero-order diffraction from the sieve. The light is collimated and passed through Aperture 2 and then a corrector element. Aperture 2 limited the light incident on the corrector FZP due to suspected issues with the outer rings. The transmitted light is then collected by the camera lens, and several focal spots are formed (resulting from the multiple diffraction orders).

Table 9. Expected Focal Spot Locations

DIFFRACTION ORDER (SIEVE / FZP)		SIEVE IMAGE (cm)	LENS IMAGE (cm)	FZP IMAGE (cm)	CAMERA IMAGE (cm)
0	+1	N/A	24.42	152.80	3.84
	0	N/A	24.42	N/A	22.72
	-1	N/A	24.42	-1.16	161.51
+1	+1	100.00	-1188.00	2.30	-3.57
	0	100.00	-1188.00	N/A	4.02
	-1	100.00	-1188.00	-2.30	23.30
+3	+1	20.00	28.08	0.84	-9.60
	0	20.00	28.08	N/A	-6.77
	-1	20.00	28.08	3.10	-2.10
-1	+1	-33.33	25.64	-2.18	25.19
	0	-33.33	25.64	N/A	213.95
	-1	-33.33	25.64	-0.75	-97.13
-3	+1	-14.29	26.25	-0.66	-68.57
	0	-14.29	26.25	N/A	-47.03
	-1	-14.29	26.25	-0.42	-38.92

In total, six spots were observed. The first two are believed to correspond to the 0 / +1 and +1 / 0 orders respectively as they are in the expected locations and respond appropriately when the primary zero-order light is removed (Aperture 1 was placed at the location of the first-order primary image such that approximately only the +1 order was transmitted). Two additional areas of apparent focused light were also observed near 8.7 cm and 12.5 cm. These spots did not correspond to any expected spots, and further investigation is needed to determine their origin. Based on the calculations in Table 9, it is assumed that neither of these spots could be the desired +1 / -1 order, and they were presently neglected. The remaining two observed spots are believed to be 0 / 0 and +1 / -1 spots, again because of their agreement with expected location and response

characteristics. Fig. 51 shows an image of what is believed to be the +1 / -1 spot, which was observed at approximately 21.5 cm from the back of the camera lens.

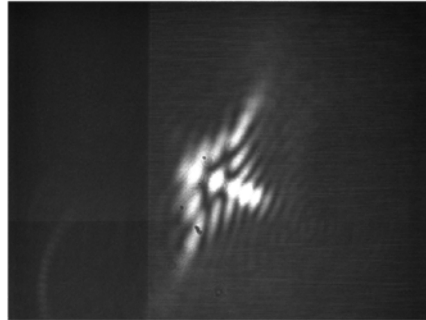


Figure 51. Corrected Spot. The image shows what is assumed to be the spot produced by the primary sieve +1 and the corrector FZP -1 orders.

While this spot does not appear to be sharp, there are several reasons why it was concluded that it is the most likely (of the spots observed) to be the desired +1 / -1 order:

1. The spot is near the expected location, and the other nearby spot is affected by the size of Aperture 1 (the +1 / -1 order should not be affected).
2. The spot is only visible when the primary sieve's zero-order is removed (using Aperture 1). The transmission of the zero-order is expected to be much higher than the other orders, indicating that it would dominate (2). Furthermore, it may be possible that the camera lens was not completely gathering all of the light diverging from the corrector (due to positioning error and lens curvature), additionally reducing the focused light.
3. When the image is defocused (either by moving the magnifying objective or by tuning the laser), a diffraction pattern emerges similar to what would be expected for a focal spot (see Fig. 52, Left).
4. The poor quality of the spot may be a result of additional diffraction orders that could not be fully removed, other unidentified light transmitted by the FZP and

captured by the camera lens, and/or aberration due to system alignment or FZP design (which is what is suspected based on analysis of the FZP independently).

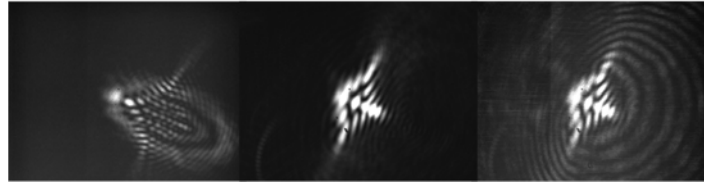


Figure 52. Corrected Spot Characteristics. Left: As the laser is tuned below 740 nm, an image typical of a defocused point is observed. Center: Using less filter (referring to the light incident on the camera), a set of concentric rings is observed to the lower right of the central spot, indicating possible aberration or interference. Right: With the aperture fully open (allowing the primary zero-order through), a set of concentric rings (with curvature opposite the Center image) is observed.

5. When the resolution chart was used instead of the point source, an image appeared in the same location (see Fig. 54) with similar characteristics.

This spot is thus the best candidate to represent the desired $+1 / -1$ order. One additional test was performed using this spot to evaluate its response to changing wavelength. Fig. 53 shows images taken at seven discrete wavelengths (731 nm, 736 nm, 739 nm, 740 nm, 741 nm, 744 nm, and 749 nm). While the image clearly changes across the 8-nm range of expected good performance, it does not appear to change much 1 nm to either side of 740 nm. If this is the correct spot, this observation is promising because, without correction, the expected bandwidth was much smaller than 2 nm.

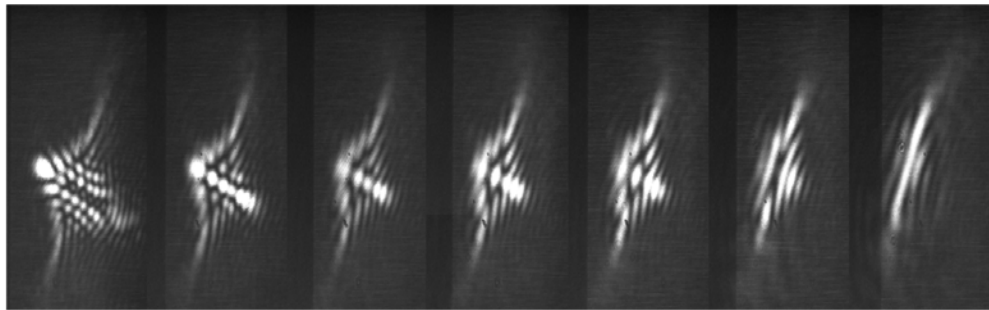


Figure 53. Corrected Spot Wavelength Variation. The images of the corrected spot were taken (left to right) at 731 nm, 736 nm, 739 nm, 740 nm, 741 nm, 744 nm, and 749 nm. Note that the images do not change appreciably over the 2-nm central range, indicating possible effectiveness of the corrector element if this spot does in fact represent the correct order.

Time constraints prevented any additional attempts to remove the diffraction orders and further isolate the correct spot. Instead, the remaining time was used to test the resolution target and to qualitatively and quantitatively investigate correction effectiveness (see below). Future work, however, should be able to confirm this is indeed the correct spot as well as sharpen the image such that testing using interferometry can be performed. Also, note that measurements of the spot size are not presented as they would likely be inaccurate due to the issues discovered with the FZP which were compensated for during testing of the resolution chart but not when viewing the focus.

The left image in Fig. 54 (formed by the primary-secondary combination) shows the test target's column "3" header. The image shows a similar "smeared" behavior as the spot in Fig. 51 and even suggests a possible double image. These observations would seem to align with the hypothesis that the outer rings of the FZP may be performing differently than the inner section. Furthermore, as the aperture in front of the FZP was closed (Fig. 54, Left to Right), the image quality improved in the same manner as did the spot during characterization of the FZP (see Fig. 47). Accordingly, this aperture was positioned such that only the central 2-4 mm of the corrector plate was illuminated.

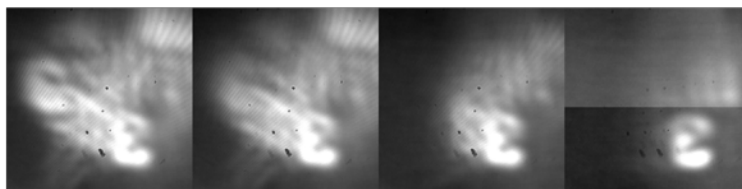


Figure 54. Aperture Adjustments to Corrected Image. This image of the resolution chart's "3" header was formed at 740 nm using the combined primary-secondary system. As the size of the aperture in front of the corrector FZP was reduced, the image quality improved (left to right). The horizontal line across the right image was not identified but is suspected to be an issue with the camera during image capture.

To qualitatively observe the behavior of the corrected system, images of the number "3" (with Aperture 2 sized such that the clearest corrected image was produced)

were taken at various wavelengths and compared to images taken with the primary alone (uncorrected at the same wavelengths). From Fig. 55, it is evident that the corrected “3” can be identified over a much broader range than the uncorrected case.

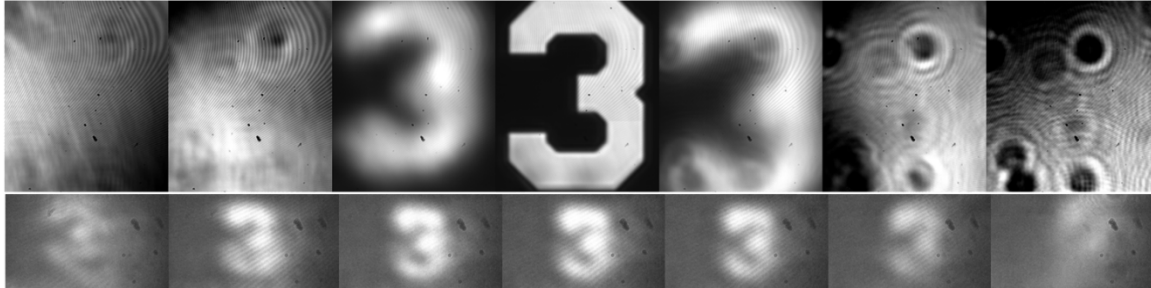


Figure 55. Corrected 3 Comparison. Top: The images of the uncorrected “3” were taken (left to right) at 731 nm, 736 nm, 739 nm, 740 nm, 741 nm, 744 nm, and 749 nm using only the primary sieve (with a diffuser positioned prior to the resolution target). Bottom: The images of the corrected “3” were taken at the same corresponding wavelengths, again with a diffuser.

More quantitative analysis involved analyzing the resolution target’s line groupings. It was determined that the “3-1” group was the smallest resolvable set by the corrected system at 740 nm (the primary system wavelength). Fig. 56 shows images of this grouping, both uncorrected (Top) and corrected (Bottom) across the target 8-nm bandwidth.

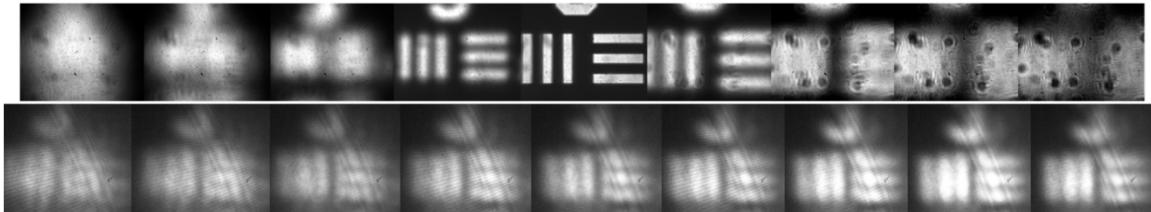


Figure 56. Corrected Line Group Comparison. Top: The images of the uncorrected “3-1” line group were taken (left to right) at 736 nm, 737 nm, 738 nm, 739 nm, 740 nm, 741 nm, 742 nm, 743 nm, and 744 nm using only the primary sieve (with a diffuser positioned prior to the resolution target). Bottom: The images of the corrected “3-1” group were taken at the same corresponding wavelengths, again with a diffuser.

Note that the corrected lines can be resolved all the way to the 744-nm right limit. They do not seem to be resolved beyond 736-737 nm on the left side; however, the correction still marks improvement over the uncorrected bandwidth. Additionally, although not

pictured, the grouping was still resolvable beyond 744 nm on the right side. Fig. 56 clearly shows an improved bandwidth (close to the target 8 nm) with the corrector.

One question, however, is the benefit of the correction when the primary sieve was able to resolve the “6-5” line grouping (4.92 μm between bars), and the corrected system, although it has an improved bandwidth, can only resolve the much larger “3-1” grouping (62.50 μm between bars). This resolution is almost 13 times the resolution of the primary alone. Because only the central 2-4 mm of the FZP was used for correction (due to Aperture 2 in front of the FZP), only a small portion of the sieve was actually used as well. When a 2-mm FZP is imaged back through the achromat, the portion of the sieve actually “seen” by the corrector is the central 0.75 cm. If Eq. 54 is again applied using this “smaller” sieve, the minimum resolvable spacing between the lines should be 60.2 μm , which is closest to the “3-1” grouping (35:8). If the aperture in front of the FZP were opened to 4 mm, the smallest resolvable group by the sieve should be the “4-1” set. The actual size of the aperture was estimated to be between 2 mm and 4 mm but likely within the 2-3 mm range. This analysis indicates that with the stopped-down aperture, the corrected system should only be able to resolve lines close to the “3-1” group, suggesting that the system is working as it should when only the central portion of the corrector is used.

One final observation is depicted in Fig. 57. The images of the “3-1” line grouping were formed at 738 nm using only the primary photon sieve. The left image was captured with a diffuser in front of the test target while no diffuser was used on the right. From these images, it seems like the diffuser actually limited the uncorrected bandwidth as the bars on the right side are still resolvable. The diffuser, however, was

necessary to observe diffraction-limited performance of the sieve. It was therefore included for all the correction comparison measurements and the resulting analysis.

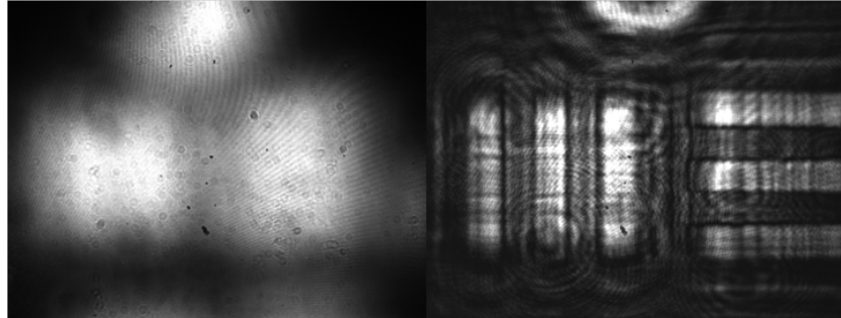


Figure 57. Diffuser Influence on Bandwidth. Both images of the “3-1” line grouping were formed at 738 nm using only the primary photon sieve. The left image was formed with a diffuser in front of the resolution target while there was no diffuser present in the right image.

Chapter Summary

This chapter covered primary and secondary sieve performance. First, the primary sieve operation was predicted and compared to results from laboratory characterization. The experimental results confirmed diffraction-limited performance of the primary sieve and also validated the Zemax models used to predict ACA and simulate a photon sieve. Second, several correction schemes were presented based on this modeling. It was shown that ACA could theoretically be removed over an expanded bandwidth using a corrector FZP or second sieve. Experimentally, correction effectiveness was measured using a FZP and showed an improved bandwidth over the uncorrected system when limitations were placed on the corrector size. Further investigation is necessary to determine why the corrector is not performing as desired and whether similar resolution, with regards to the “6-5” grouping visible to the primary alone, is achievable.

V. Conclusion

The purpose of this chapter is to provide an overview of the major tasks accomplished and the results achieved throughout this research project. Specifically, it will evaluate the thesis with regard to the four objectives outlined at the beginning: establishing a realistic target bandwidth; designing and characterizing an imaging photon sieve; creating a bandwidth-broadening correction scheme for this particular sieve based on a FZP (or corresponding second photon sieve); and demonstrating effectiveness of this correction process. Ideas for continuing this research and starting new endeavors will be discussed.

Conclusion

First, a radiometric analysis was conducted on a system consisting only of a notional photon sieve with no additional correction. The bandwidth required to allow an appropriate amount of energy to be collected by this sieve was determined to be 8 nm. This value provided an order-of-magnitude target for similar sieve-based imaging and thus satisfied the first objective.

Next, a functional primary photon sieve was designed and fabricated. While this device was built specifically for use in the AFIT laboratory environment, the physical principles governing its operation are representative of many systems using a similar optic. Diffraction-limited performance and imaging capability of the sieve was demonstrated at the primary wavelength. Additionally, the chromatic aberration effects across an 8-nm range were experimentally characterized, satisfying the second objective.

The experimental data showed strong agreement with both geometrically-predicted values as well as Zemax simulations. The computer modeling confirmed that the software was correctly simulating both the system and the photon sieve performance. Zemax could thus be reliably used to model a corrector. Accordingly, a flexible correction scheme was developed that allowed variation in collimating optic focal length to achieve a particular bandwidth, satisfying the third objective.

Correction scheme models showed diffraction-limited performance over a much greater bandwidth range than the primary alone. The useable bandwidths ranged from 8 nm to 18 nm, demonstrating improvement over the uncorrected system. Furthermore, the upper value of 18 nm is a factor of the 350-mm collimating lens used and can be adjusted by simply changing the lens focal length. Secondary photon sieves and corresponding FZPs based on these parameters were designed and fabricated for two of the correction (achromat) options. Experimental testing of one of the FZP corrector optics was accomplished and demonstrated bandwidth enhancement over the primary sieve alone. This corrected system did not achieve the same resolution when compared to the design-wavelength capability of the primary sieve. This effect was likely due to the design and performance of the outer portion of the corrector. When the reduced size of the corrector (and corresponding reduced size of the primary) was considered, however, the system did exhibit performance close to what was expected over the nearly 8-nm target bandwidth (an improvement over the primary sieve alone), satisfying the fourth objective. Additionally, because the experimental characterization of the primary sieve so closely matched the predictions, there is presently no reason to doubt that, if

constructed properly, a corrector FZP (or sieve) would yield experimental data much different than the theoretical data examined.

In summary, experimental testing of the primary sieve demonstrated that Zemax could adequately model the system and thus be used to design a corrector and forecast correction effectiveness. Simulations involving this secondary optic demonstrated that a FZP or second photon sieve should be able to be usefully employed to correct for chromatic aberration and effectively expand the bandwidth of a sieve-based (primary) imaging system. Experimentally, the FZP could not be tested as intended most likely due to problems with the outer rings (design or fabrication). With the reduced diameter of the FZP, the system demonstrated correction over a nearly 8 nm bandwidth at a resolution of approximately 13 times that of the primary sieve. However, this resolution, while worse than that of the primary, does represent nearly diffraction-limited performance when the fact that the stopped-down FZP effectively limits the useable diameter of the primary sieve is considered. Thus, in conclusion, an effective correction scheme based on the use of a FZP was demonstrated.

Future Work and Action

Several modifications could be made to this particular project to enhance the results. First and foremost, the corrector must be analyzed and likely redesigned (possibly as a photon sieve) to be able to use the full extent of the device. Constraints on the printing process restricted the design of the FZP, and the methods used to compensate for these restrictions may be responsible for the ineffectiveness of the outer portion. Additionally, unidentified system alignment issues may also be causing problems.

Once the corrector has been analyzed, diffraction orders must be adequately separated to correctly identify the spot for analysis and then conduct testing based on interferometry to more precisely determine the corrector effectiveness. Because of laboratory equipment constraints, measuring ACA (using image location measurements) in the corrector system would not be possible. In order to accomplish this task, a larger translation stage with a more sensitive micrometer would be needed. Additionally, image-analysis software would likely be required to help determine the location of the focus (smallest spot).

A new radiometric analysis could be conducted that more closely models the desired system. Now that a practical correction scheme has been determined, the parameters of this scheme could be added to the analysis to give a more accurate idea of the required bandwidth. The correction scheme could then be adjusted as necessary.

Moving forward, the next step would be to work on constructing a system for use in an actual application, such as a future variation of the FalconSAT payload. Engineering constraints would no longer be neglected, and the system would have to be developed to meet certain size and weight criteria. Additionally, more research would be necessary to determine other factors requiring consideration that are unique to a specific application.

Appendix

Radiometry MATLAB Code

This script computes and plots the SNR as a function of bandwidth when using a photon sieve to conduct Earth imaging. It uses a variety of sieve parameters (labeled “Iteration A, B, C, or D”).

```
clear all
clc

%Constants
c=3e8; %Speed of light [m]
h=6.626e-34; %Planck's constant [J*s]
k=1.38e-23; %Boltzmann constant [J/K]
Temp=5778; %Blackbody (Sun) temperature [K]
lambda_halpha=656.28e-9; %Center wavelength [m]
As=1.52e18; %Sun area [m^2]
re_s=1.52e11; %Earth-Sun distance [m]

%% Iteration A (parameters set to 30cm sieve (f/4) with 1.5ms integration time)

%Adjustable parameters
dsv=0.3; %Sieve diameter [m]
Asv=pi*((dsv/2)^2); %Sieve area [m^2]
R=0.2; %Earth reflectivity
T=0.1; %Sieve transmission
n=0.4; %Sieve quantum efficiency
f=1.2; %Sieve focal length [m]
dp=4.65e-6; %Pixel size
Ap=dp^2; %Pixel area [m^2]
t=1.5e-3; %Integration time [s]

%Define array sizes
Ls=zeros(1000,1);
Ne=zeros(1000,1);
SNR_A=zeros(1000,1);

%Compute solar radiance using blackbody integral
C1=2*h*c^2;
C2=h*c/(k*Temp);
func=@(x)C1./((x.^5).*(exp(C2./x)-1));
delta_nm=0.01:0.01:10; %Bandwidth (variable) [nm]
delta_nm=delta_nm';
delta=delta_nm.*1e-9; %Bandwidth [m]
for i=1:1000
a=lambda_halpha-delta(i)/2; %Lower integration limit
```

```

b=lambda_halpha+delta(i)/2;      %Upper integration limit
Ls(i)=integral(func,a,b);         %Solar radiance [W/(m^2*sr)]

%Compute electron count per pixel
Ne(i)=(R*As*Ls(i)*Ap*Asv*lambda_halpha*T*t*n)/(2*pi*(re_s^2)*(f^2)*h*c);

%Compute SNR
SNR_A(i)=Ne(i)/((Ne(i)+100)^(1/2));
end

figure;
plot (delta_nm,SNR_A,'LineWidth',2)
grid on;
xlim([0.01 10]);
xlabel({'Bandwidth, \lambda'; '[nm]'},'FontWeight','bold', 'FontSize', 18);
ylabel({'SNR'},'FontWeight','bold', 'FontSize', 18);
set(gca,'XMinorTick','on','YMinorTick','on');

%% Iteration B (parameters set to 20cm sieve (f/2) with 2.3ms integration time)

%Adjustable parameters
dsv=0.2;                        %Sieve diameter [m]
Asv=pi*((dsv/2)^2);            %Sieve area [m^2]
R=0.2;                          %Earth reflectivity
T=0.1;                          %Sieve transmission
n=0.4;                          %Sieve quantum efficiency
f=1.2;                          %Sieve focal length [m]
dp=4.65e-6;                    %Pixel size
Ap=dp^2;                       %Pixel area [m^2]
t=2.3e-3;                      %Integration time [s]

%Define array sizes
Ls=zeros(1000,1);
Ne=zeros(1000,1);
SNR_B=zeros(1000,1);

%Compute solar radiance using blackbody integral
C1=2*h*c^2;
C2=h*c/(k*Temp);
func=@(x)C1./((x.^5).*(exp(C2./x)-1));
delta_nm=0.01:0.01:10;        %Bandwidth (variable) [nm]
delta_nm=delta_nm';
delta=delta_nm.*1e-9;          %Bandwidth [m]
for i=1:1000
a=lambda_halpha-delta(i)/2;    %Lower integration limit
b=lambda_halpha+delta(i)/2;    %Upper integration limit
Ls(i)=integral(func,a,b);      %Solar radiance [W/(m^2*sr)]

%Compute electron count per pixel
Ne(i)=(R*As*Ls(i)*Ap*Asv*lambda_halpha*T*t*n)/(2*pi*(re_s^2)*(f^2)*h*c);

%Compute SNR

```

```
SNR_B(i)=Ne(i)/((Ne(i)+100)^(1/2));
end
```

%% Iteration C (parameters set to 30cm sieve (f/2) with 1.5ms integration time)

% Adjustable parameters

```
dsv=0.3; %Sieve diameter [m]
Asv=pi*((dsv/2)^2); %Sieve area [m^2]
R=0.2; %Earth reflectivity
T=0.1; %Sieve transmission
n=0.4; %Sieve quantum efficiency
f=0.6; %Sieve focal length [m]
dp=4.65e-6; %Pixel size
Ap=dp^2; %Pixel area [m^2]
t=1.5e-3; %Integration time [s]
```

% Define array sizes

```
Ls=zeros(1000,1);
Ne=zeros(1000,1);
SNR_C=zeros(1000,1);
```

% Compute solar radiance using blackbody integral

```
C1=2*h*c^2;
C2=h*c/(k*Temp);
func=@(x)C1./((x.^5).*(exp(C2./x)-1));
delta_nm=0.01:0.01:10; %Bandwidth (variable) [nm]
delta_nm=delta_nm';
delta=delta_nm.*1e-9; %Bandwidth [m]
for i=1:1000
a=lambda_halpha-delta(i)/2; %Lower integration limit
b=lambda_halpha+delta(i)/2; %Upper integration limit
Ls(i)=integral(func,a,b); %Solar radiance [W/(m^2*sr)]
```

% Compute electron count per pixel

```
Ne(i)=(R*As*Ls(i)*Ap*Asv*lambda_halpha*T*t*n)/(2*pi*(re_s^2)*(f^2)*h*c);
```

% Compute SNR

```
SNR_C(i)=Ne(i)/((Ne(i)+100)^(1/2));
end
```

%% Iteration D (parameters set to 30cm sieve (f/3) with 1.5ms integration time)

% Adjustable parameters

```
dsv=0.3; %Sieve diameter [m]
Asv=pi*((dsv/2)^2); %Sieve area [m^2]
R=0.2; %Earth reflectivity
T=0.1; %Sieve transmission
n=0.4; %Sieve quantum efficiency
f=0.9; %Sieve focal length [m]
dp=4.65e-6; %Pixel size
Ap=dp^2; %Pixel area [m^2]
t=1.5e-3; %Integration time [s]
```

```

%Define array sizes
Ls=zeros(1000,1);
Ne=zeros(1000,1);
SNR_D=zeros(1000,1);

%Compute solar radiance using blackbody integral
C1=2*h*c^2;
C2=h*c/(k*Temp);
func=@(x)C1./((x.^5).*(exp(C2./x)-1));
delta_nm=0.01:0.01:10;      %Bandwidth (variable) [nm]
delta_nm=delta_nm';
delta=delta_nm.*1e-9;        %Bandwidth [m]
for i=1:1000
a=lambda_half-delta(i)/2;    %Lower integration limit
b=lambda_half+delta(i)/2;    %Upper integration limit
Ls(i)=integral(func,a,b);     %Solar radiance [W/(m^2*sr)]

%Compute electron count per pixel
Ne(i)=(R*As*Ls(i)*Ap*Asv*lambda_half*T*t*n)/(2*pi*(re_s^2)*(f^2)*h*c);

%Compute SNR
SNR_D(i)=Ne(i)/((Ne(i)+100)^(1/2));
end

%% Plot composite figures
figure;
plot (delta_nm,SNR_A,delta_nm,SNR_B,delta_nm,SNR_C,delta_nm,SNR_D,'LineWidth',2);
grid on;
xlim([0.01 0.1]);
xlabel({'Bandwidth, \lambda'; '[nm]'},'FontWeight','bold', 'FontSize', 18);
ylabel({'SNR'},'FontWeight','bold', 'FontSize', 18);
set(gca,'XMinorTick','on','YMinorTick','on');
legend('30cm, f/4, 1.5ms','20cm, f/2, 2.3ms','30cm, f/2, 1.5ms','30cm, f/3, 1.5ms')

figure;
plot (delta_nm,SNR_A,delta_nm,SNR_B,delta_nm,SNR_C,delta_nm,SNR_D,'LineWidth',2);
grid on;
xlim([0.01 10]);
xlabel({'Bandwidth, \lambda'; '[nm]'},'FontWeight','bold', 'FontSize', 18);
ylabel({'SNR'},'FontWeight','bold', 'FontSize', 18);
set(gca,'XMinorTick','on','YMinorTick','on');
legend('30cm, f/4, 1.5ms','20cm, f/2, 2.3ms','30cm, f/2, 1.5ms','30cm, f/3, 1.5ms')

```


Primary Photon Sieve Design MATLAB Code

This script identifies the sizes and position of the photon sieve holes and exports the information in Gerber format for processing. It is adapted from the code created by Andersen (3). It ignores any considerations relating to fabrication resolution.

```
clear all
clc

%%% Set user defined values
lambda=740e-9;           % Wavelength [m]
f=0.5;                   % Focal length [m]
svdiam=.1;               % Desired sieve diameter [m]
scalefactor=0.9;         % Fraction of max number of holes per ring

%%% Calculate additional constants from user input
fnumber=f/svdiam;        % f/#
rmax=svdiam/2;           % Max radius [m]
nmax=floor((-4*f+2*sqrt(4*f^2+rmax^2))/lambda); % Outermost ring

%%% Open the Gerber File for editing and write header/parameters applicable to the entire file
GerberFile=fopen('C:\Users\Chris\Desktop\tulip_photonsieve_no_resolution.gbr','w+');
fprintf(GerberFile,'G75*\r\n'); % Set Multi Quadrant Mode; \r for Notepad viewing
fprintf(GerberFile,'%FSLAX35Y35*%\r\n'); % Set coordinate Format Specification to omit
Leading zeros, use Absolute notation, set number of integer positions in X,Y coordinates to 3 and decimal
positions to 5
fprintf(GerberFile,'%IPPOS*%\r\n'); % Set image polarity to "positive"
fprintf(GerberFile,'%LPD*%\r\n'); % Set layer polarity to "dark"
fprintf(GerberFile,'%MOMM*%\r\n'); % Set units to [mm]

tic;
%%% Create aperture for each ring
for j=1 nmax
    n=j;
    rn=sqrt(2*n*lambda*f+(n^2)*(lambda^2)/4); % Ring radius [m]
    w=lambda*f/(2*rn); % Fresnel zone size at rn [m]
    d=1.53*w; % Hole diameter [m]
    if n<2;
        maxdiam=d;
    end
    diam=1000*d; % Hole diameter [mm]
    apnum=j+9; % Aperture number (>10)
    fprintf(GerberFile,'%ADD% dC,%.5f*%\r\n',apnum,diam);
end

%%% Position apertures
area=0;
totholes=0;
for j=1 nmax
    phi=2*pi*random('unif',1); % Random starting angle
```

```

n=j;
rn=sqrt(2*n*lambda*f+(n^2)*(lambda^2)/4);
w=lambda*f/(2*rn);
d=1.53*w;
diam=1000*d;
apnum=j+9;
fprintf(GerberFile,'D%d*\r\n',apnum);           %Identifies which aperture to place
C=asin(d/2/rn);
numholes=floor(scalefactor*(2*pi/(2*C)));        %Max number of angular holes scaled
totholes=totholes+numholes;                      %Total number of holes
holegap=(2*pi-numholes*2*C)/numholes;            %Angular gap between holes [rad]
area=area+numholes*pi*(d/2)^2;                  %Total area covered by holes
for i=1 numholes                                 %Position each hole at an x,y coordinate
    x=100000000*rn*cos(phi);                     %x coordinate [um]
    y=100000000*rn*sin(phi);                     %y coordinate [um]
    fprintf(GerberFile,'X%.0fY%.0fD03*\r\n',x,y);
    phi=phi+2*C+holegap;                         %Reset hole center
end
end
areacoverage=100*area/(pi*rn^2);                 %Total area covered by holes [%]
holesep=(2*C+holegap)*rn-d;                     %Outer ring hole separation [m]

%% Terminate and close Gerber File
fprintf(GerberFile,'M02*');                      %End Gerber File
fclose(GerberFile);
toc;

%% Display useful information
ReadFile=fopen('C:\Users\Chris\Desktop\tulip_photonsieve_no_resolution.txt','w+');
fprintf(ReadFile,'Photon Sieve Specifications\r\n');
fprintf(ReadFile,'Incident Wavelength: %.0f [nm]\r\n',lambda*1e9);
fprintf(ReadFile,'Focal Length: %.2f [m]\r\n',f);
fprintf(ReadFile,'Target Diameter: %.2f [m]\r\n',svdiam);
fprintf(ReadFile,'Actual Diameter: %.2f [m]\r\n',2*rn+d/2);
fprintf(ReadFile,'F Number: %.1f\r\n',fnumber);
fprintf(ReadFile,'Total Rings: %.1f\r\n',nmax);
fprintf(ReadFile,'Total Holes: %.1f\r\n',totholes);
fprintf(ReadFile,'Max Hole Size: %.2f [um]\r\n',maxdiam*1e6);
fprintf(ReadFile,'Min Hole Size: %.2f [um]\r\n',d*1e6);
fprintf(ReadFile,'Min Zone Size: %.2f [um]\r\n',w*1e6);
fprintf(ReadFile,'nmax Hole Separation: %.2f [um]\r\n',holesep*1e6);
fprintf(ReadFile,'nmax d/w: %.2f\r\n',d/w);
fprintf(ReadFile,'File Generation Time: %.2f [min]\r\n',toc/60);
fprintf(ReadFile,'Area Covered: %.2f%%\r\n',areacoverage);

```

High Precision Primary Photon Sieve Design MATLAB Code

This script identifies the sizes and position of the photon sieve holes and exports the information in Gerber format for processing. It is again adapted from the code

created by Andersen (3). The method considers the resolution of the printing process which specifies both an error in the feature size and a minimum separation distance (radial and lateral). The d/w ratio is adjusted to prevent radial overlap. The lateral scale factor is adjusted for each ring such that the maximum number of holes is scaled below maximum to prevent lateral overlap.

```
clear all
clc

%% Set initial user-defined values
lambda=740e-9; % Wavelength [m]
f=0.5; % Focal length [m]
svdiam=.1; % Desired sieve diameter [m]
minholesep=1.5e-6; % Minimum hole separation [m] (set by printing requirements)
reserror=0.25e-6; % Error in feature size [m]

%% Calculate additional information from user input
fnumber=f/svdiam; % f/#
rmax=svdiam/2; % Approximate max radius [m] (based on
desired sieve diameter)
nmax=floor((-4*f+2*sqrt(4*f^2+rmax^2))/lambda); % Outermost ring # (rounded down)
rmax=sqrt(2*nmax*lambda*f+(nmax^2)*(lambda^2)/4); % Max radius [m] (based on nmax)
wmin=lambda*f/(2*rmax); % Min zone size (outer ring) [m]
dmax=2*wmin-(reserror+minholesep); % Largest d can be to ensure specified radial
sep [m]
d_over_w=floor((dmax/wmin)*100)/100; % d/w value that gives max diameter (rounds
down to nearest second decimal as buffer)
wtrans=(minholesep+reserror)/(2-1.53); % Hole size using d/w=1.53 that results in
less than min sep [m]
rtrans=lambda*f/(2*wtrans); % Radius where transition zone occurs [m]
trans_ratio=rtrans/rmax; % Ratio of sieve covered by "normal" sized
holes to total sieve
ntrans=floor(trans_ratio*nmax); % First ring of "non-standard" holes
(rounded down)

%% Open the Gerber File for editing and write header/parameters applicable to the entire file
GerberFile=fopen('C:\Users\Chris\Desktop\tulip_photonsieve_resolution.gbr','w+');
fprintf(GerberFile,'G75*\r\n'); % Set Multi Quadrant Mode; \r for Notepad viewing
fprintf(GerberFile,'%%FSLAX35Y35*%\r\n'); % Set coordinate Format Specification to omit
Leading zeros, use Absolute notation, set number of integer positions in X,Y coordinates to 3 and decimal
positions to 5
fprintf(GerberFile,'%%IPPOS*%\r\n'); % Set image polarity to "positive"
fprintf(GerberFile,'%%LPD*%\r\n'); % Set layer polarity to "dark"
fprintf(GerberFile,'%%MOMM*%\r\n'); % Set units to [mm]

tic;
%% Create aperture for each ring
```

```

for j=1 ntrans-11                                     %Variable diameters until ntrans-10 (start 10 rings
early for buffer)
    n=j;
    rn=sqrt(2*n*lambda*f+(n^2)*(lambda^2)/4);          %Ring radius [m]
    w=lambda*f/(2*rn);                                %Fresnel zone size at rn [m]
    d=1.53*w;                                           %Hole diameter [m]
    if n<2;
        maxdiam=d;                                    %Max hole size occurs in first ring
    end
    diam=1000*d;                                        %Hole diameter [mm]
    apnum=j+9;                                          %Aperture number (>10)
    fprintf(GerberFile,'% %ADD%dC,%.5f*% %\r\n',apnum,diam);
end
for j=ntrans-10:nmax                                  %Second loop to adjust d/w for outer ring radial
separation
    n=j;
    rn=sqrt(2*n*lambda*f+(n^2)*(lambda^2)/4);
    w=lambda*f/(2*rn);
    d=d_over_w*w;
    diam=1000*d;
    apnum=j+9;
    fprintf(GerberFile,'% %ADD%dC,%.5f*% %\r\n',apnum,diam);
end

%%% Position apertures
area=0;
totholes=0;
for j=1 ntrans-11
    phi=2*pi*random('unif',1);                         %Random starting angle
    n=j;
    rn=sqrt(2*n*lambda*f+(n^2)*(lambda^2)/4);
    w=lambda*f/(2*rn);
    d=1.53*w;
    diam=1000*d;
    apnum=j+9;
    fprintf(GerberFile,'D%d*\r\n',apnum);               %Identifies which aperture to place
    C=asin(d/2/rn);
    scalefactor=1-(minholesep/(d+reserror+minholesep))-03; %Fraction of max number of holes per ring
    minus 3% buffer (ensures radial spacing)
    if n<2;
        maxscale=scalefactor;                          %As n inc, d dec, and scalefactor dec
    end
    numholes=floor(scalefactor*(2*pi/(2*C)));            %Max number of angular holes scaled
    totholes=totholes+numholes;                          %Total number of holes
    holegap=(2*pi-numholes*2*C)/numholes;                %Angular gap between holes [rad]
    area=area+numholes*pi*(d/2)^2;                       %Total area covered by holes
    for i=1 numholes                                     %Position each hole at an x,y coordinate
        x=100000000*rn*cos(phi);                        %x coordinate [um]
        y=100000000*rn*sin(phi);                        %y coordinate [um]
        fprintf(GerberFile,'X%.0fY%.0fD03*\r\n',x,y);
        phi=phi+2*C+holegap;                             %Reset hole center
    end
end
for j=ntrans-10:nmax

```

```

phi=2*pi*random('unif',1);
n=j;
rn=sqrt(2*n*lambda*f+(n^2)*(lambda^2)/4);
w=lambda*f/(2*rn);
d=d_over_w*w;
diam=1000*d;
apnum=j+9;
fprintf(GerberFile,'D%d*\r\n',apnum);
C=asin(d/2/rn);
scalefactor=1-(minholesep/(d+reserror+minholesep))-03;
numholes=floor(scalefactor*(2*pi/(2*C)));
totholes=totholes+numholes;
holegap=(2*pi-numholes*2*C)/numholes;
area=area+numholes*pi*(d/2)^2;
for i=1 numholes
    x=100000000*rn*cos(phi);
    y=100000000*rn*sin(phi);
    fprintf(GerberFile,'X%.0fY%.0fD03*\r\n',x,y);
    phi=phi+2*C+holegap;
end
end
areacoverage=100*area/(pi*rn^2); %Total area covered by holes [%]
holesep=(2*C+holegap)*rn-d; %Outer ring hole separation [m]

%% Terminate and close Gerber File
fprintf(GerberFile,'M02*'); %End Gerber File
fclose(GerberFile);
toc;

%% Display useful information
ReadFile=fopen('C:\Users\Chris\Desktop\tulip_photonsieve_resolution.txt','w+');
fprintf(ReadFile,'Photon Sieve Specifications\r\n');
fprintf(ReadFile,'Incident Wavelength: %.1f [nm]\r\n',lambda*1e9);
fprintf(ReadFile,'Focal Length: %.2f [m]\r\n',f);
fprintf(ReadFile,'Target Diameter: %.2f [m]\r\n',svdiam);
fprintf(ReadFile,'Actual Diameter: %.2f [m]\r\n',2*rn+d/2);
fprintf(ReadFile,'F Number: %.1f\r\n',fnumber);
fprintf(ReadFile,'Total Rings: %.1f\r\n',nmax);
fprintf(ReadFile,'Transition Ring: %.1f\r\n',ntrans);
fprintf(ReadFile,'Total Holes: %.1f\r\n',totholes);
fprintf(ReadFile,'Min Scale Factor: %.2f%\r\n',scalefactor);
fprintf(ReadFile,'Max Scale Factor: %.2f%\r\n',maxscale);
fprintf(ReadFile,'Percent Covered by Normal Hole Size: %.2f%%\r\n',100*(ntrans-11)/nmax);
fprintf(ReadFile,'Max Hole Size: %.2f [um]\r\n',maxdiam*1e6);
fprintf(ReadFile,'Min Hole Size: %.2f [um]\r\n',d*1e6);
fprintf(ReadFile,'nmax Hole Separation: %.2f [um]\r\n',holesep*1e6);
fprintf(ReadFile,'Outer Ring d/w: %.4f\r\n',d/w);
fprintf(ReadFile,'Area Covered: %.2f%%\r\n',areacoverage);
fprintf(ReadFile,'File Generation Time: %.2f [min]\r\n',toc/60);

```

Secondary/Corrector Photon Sieve Design MATLAB Code

This script identifies the sizes and position of the photon sieve (corrector) holes and exports the information in Gerber format for processing. It is again adapted from the code created by Andersen (3). This design differs from that of the primary photon sieve in that it is designed to be used with a collimated beam (infinite conjugate) rather than in point-to-point imaging. It also skips every other zone near the edge of the sieve to compensate for a smaller device and decreased radial spacing.

```
clear all
clc

%% Set initial user-defined values
lambda=739e-9; %Wavelength [m]
f=0.023077; %Focal length [m] for use with 220mm collimator
f=0.043567; %Focal length [m] for use with 300mm collimator
svdiam=.023; %Desired sieve diameter rounded up to capture all light [m]
for use with 220mm collimator
svdiam=0.03; %Desired sieve diameter rounded up to capture all light [m]
for use with 300mm collimator
minholesize=1.5e-6; %Smallest printed feature size [m]
minholesep=1.5e-6; %Minimum hole separation [m] (set by printing requirements)
reserror=0.25e-6; %Error in feature size [m]

%% Calculate additional information from user input
fnumber=f/svdiam; %f/#
rmax=svdiam/2; %Approximate max radius [m] (based on
desired sieve diameter)
nmax=2*floor((-f+sqrt(f^2+rmax^2))/lambda)/2; %Outermost ring # (rounded down to
nearest EVEN integer)
rmax=sqrt(2*nmax*lambda*f+(nmax^2)*(lambda^2)); %Max radius [m] (based on nmax)
wmin=lambda*f/(2*rmax); %Min zone size (outer ring) [m]
wtrans=(minholesep+reserror)/(2-1.53); %Hole size using d/w=1.53 that results in
less than min sep [m]
rtrans=lambda*f/(2*wtrans); %Radius where transition zone occurs [m]
trans_ratio=rtrans/rmax; %Ratio of sieve covered by "normal" sized
holes to total sieve
ntrans=2*floor((trans_ratio*nmax)/2); %First ring of "non-standard" holes
(rounded down to nearest EVEN integer)

%% Open the Gerber File for editing and write header/parameters applicable to the entire file
GerberFile=fopen('C:\Users\Chris\Desktop\tulip_photonsieve_corrector_resolution.gbr','w+');
fprintf(GerberFile,'G75*\r\n'); %Set Multi Quadrant Mode; \r for Notepad viewing
fprintf(GerberFile,'%%FSLAX35Y35*%\r\n'); %Set coordinate Format Specification to omit
Leading zeros, use Absolute notation, set number of integer positions in X,Y coordinates to 3 and decimal
positions to 5
```

```

fprintf(GerberFile, '% %IPPOS*% %\r\n');
fprintf(GerberFile, '% %LPD*% %\r\n');
fprintf(GerberFile, '% %MOMM*% %\r\n');

tic;
%% Create aperture for each ring
for j=1 ntrans-1
    n=j;
    rn=sqrt(2*n*lambda*f+(n^2)*(lambda^2));
    w=lambda*f/(2*rn);
    d=1.53*w;
    if n<2;
        maxdiam=d;
    end
    diam=1000*d;
    apnum=j+9;
    fprintf(GerberFile, '% %ADD%dC,%.5f*% %\r\n',apnum,diam);
end
for j=ntrans:2 nmax
    separation (skipping every other zone)
    n=j;
    rn=sqrt(2*n*lambda*f+(n^2)*(lambda^2));
    w=lambda*f/(2*rn);
    d=minholesize;
    diam=1000*d;
    apnum=j+9;
    fprintf(GerberFile, '% %ADD%dC,%.5f*% %\r\n',apnum,diam);
end

%% Position apertures
area=0;
totholes=0;
for j=1 ntrans-1
    phi=2*pi*random('unif',1);
    n=j;
    rn=sqrt(2*n*lambda*f+(n^2)*(lambda^2));
    w=lambda*f/(2*rn);
    d=1.53*w;
    diam=1000*d;
    apnum=j+9;
    fprintf(GerberFile, 'D%d*\r\n',apnum);
    C=asin(d/2/rn);
    scalefactor=1-(minholesep/(d+reserror+minholesep))-0.05;
    minus 5% buffer (ensures radial spacing)
    if n<2;
        maxscale=scalefactor;
    end
    numholes=floor(scalefactor*(2*pi/(2*C)));
    totholes=totholes+numholes;
    holegap=(2*pi-numholes*2*C)/numholes;
    area=area+numholes*pi*(d/2)^2;
    for i=1 numholes
        x=100000000*rn*cos(phi);
        y=100000000*rn*sin(phi);

```

```

%Set image polarity to "positive"
%Set layer polarity to "dark"
%Set units to [mm]

%Variable diameters until ntrans (if ntrans < nmax)

%Ring radius [m]
%Fresnel zone size at rn [m]
%Hole diameter [m]

%Largest hole occurs in first ring

%Hole diameter [mm]
%Aperture number (>10)

%Second loop to adjust d/w for outer ring radial

%Holes set at constant value

%Random starting angle

%Identifies which aperture to place

%Fraction of max number of holes per ring

%As n inc, d dec, and scalefactor dec

%Max number of angular holes scaled
%Total number of holes
%Angular gap between holes [rad]
%Total area covered by holes
%Position each hole at an x,y coordinate
%x coordinate [um]
%y coordinate [um]

```

```

        fprintf(GerberFile,'X%.0fY%.0fD03*\r\n',x,y);
        phi=phi+2*C+holegap; %Reset hole center
    end
end
for j=ntrans:2 nmax
    phi=2*pi*random('unif',1);
    n=j;
    rn=sqrt(2*n*lambda*f+(n^2)*(lambda^2));
    w=lambda*f/(2*rn);
    d=minholesize;
    if j<nmax;
        secondtolast=rn+d/2; %Radial distance to outside of second-to-last ring [m]
    end
    last=rn-d/2; %Radial distance to inside of last ring [m]
    diam=1000*d;
    apnum=j+9;
    fprintf(GerberFile,'D%d*\r\n',apnum);
    C=asin(d/2/rn);
    scalefactor=1-(minholesep/(d+reserror+minholesep))-0.05;
    numholes=floor(scalefactor*(2*pi/(2*C)));
    totholes=totholes+numholes;
    holegap=(2*pi-numholes*2*C)/numholes;
    area=area+numholes*pi*(d/2)^2;
    for i=1 numholes
        x=100000000*rn*cos(phi);
        y=100000000*rn*sin(phi);
        fprintf(GerberFile,'X%.0fY%.0fD03*\r\n',x,y);
        phi=phi+2*C+holegap;
    end
end
areacoverage=100*area/(pi*rn^2); %Total area covered by holes [%]
holesep=(2*C+holegap)*rn-d; %Outer ring hole separation [m]

%% Terminate and close Gerber File
fprintf(GerberFile,'M02*'); %End Gerber File
fclose(GerberFile);
toc;

%% Display useful information
ReadFile=fopen('C:\Users\Chris\Desktop\tulip_photonsieve_corrector_resolution.txt','w+');
fprintf(ReadFile,'Photon Sieve Corrector Specifications\r\n');
fprintf(ReadFile,'Incident Wavelength: %.1f [nm]\r\n',lambda*1e9);
fprintf(ReadFile,'Focal Length: %.2f [m]\r\n',f);
fprintf(ReadFile,'Target Diameter: %.6f [m]\r\n',svdiam);
fprintf(ReadFile,'Actual Diameter: %.6f [m]\r\n',2*rn+d/2);
fprintf(ReadFile,'F Number: %.1f\r\n',fnumber);
fprintf(ReadFile,'Total Rings: %.1f\r\n',(nmax-ntrans)/2+ntrans);
fprintf(ReadFile,'Transition Ring: %.1f\r\n',ntrans);
fprintf(ReadFile,'Total Holes: %.1f\r\n',totholes);
fprintf(ReadFile,'Min Scale Factor: %.2f%\r\n',scalefactor);
fprintf(ReadFile,'Max Scale Factor: %.2f%\r\n',maxscale);
fprintf(ReadFile,'Percent Covered by Normal Hole Size: %.2f%%\r\n',100*(ntrans-1)/((nmax-ntrans)/2+ntrans));
fprintf(ReadFile,'Max Hole Size: %.2f [um]\r\n',maxdiam*1e6);

```



```
fprintf(ReadFile,'Min Hole Size: %.2f [um]\r\n',d*1e6);
fprintf(ReadFile,'nmax Lateral Hole Separation: %.2f [um]\r\n',holesep*1e6);
fprintf(ReadFile,'nmax Radial Hole Separation: %.2f [um]\r\n',(last-secondtolast)*1e6);
fprintf(ReadFile,'Outer Ring d/w: %.4f\r\n',d/w);
fprintf(ReadFile,'Area Covered: %.2f%%\r\n',areacoverage);
fprintf(ReadFile,'File Generation Time: %.2f [min]\r\n',toc/60);
```

Fresnel Zone Plate Design MATLAB Code

This script identifies the sizes and position of the Fresnel zone plate (corrector) rings and exports the information in Gerber format for processing. The method considers the resolution of the printing process which specifies both an error in the feature size and a minimum separation distance (radial). This design is meant to be used with a collimated beam (infinite conjugate). Note that the code uses the Gerber Primitive Macro "Moire" by deleting the cross-hair, setting the total rings to "1," and overlaying many of them to make all the rings. This device can also be designed by writing complete arcs in Gerber format to create the rings (2).

```
clear all
clc
```

%% Set initial user-defined values

```
lambda=739e-9;           %Wavelength [m]
f=0.023077;              %Focal length [m] for use with 220mm collimator
f=0.043567;              %Focal length [m] for use with 300mm collimator
%ptdiam=0.023;           %Desired plate diameter rounded up to capture all light [m]
for use with 220mm collimator
ptdiam=0.03;              %Desired plate diameter rounded up to capture all light [m]
for use with 300mm collimator
minringsize=1.5e-6;       %Smallest printed feature size [m]
reserror=0.25e-6;         %Error in feature size [m]
```

%% Calculate additional information from user input

```
fnumber=f/ptdiam;        %f/#
rmax=ptdiam/2;            %Approximate max radius [m] (based on
desired plate diameter)
nmax=2*floor(((-f+sqrt(f^2+rmax^2))/lambda)/2); %Outermost ring # (rounded down to
nearest EVEN integer)
rmax=sqrt(2*nmax*lambda*f+(nmax^2)*(lambda^2)); %Max radius [m] (based on nmax)
wmin=lambda*f/(2*rmax);   %Min zone size (outer ring) [m]
wtrans=(minringsize+reserror)/(2-1);           %Ring size using d/w=1 that results in less
than min sep [m]
```

```

rtrans=lambda*f/(2*wtrans); %Radius where transition zone occurs [m]
trans_ratio=rtrans/rmax; %Ratio of plate covered by "normal" sized rings to
total plate
ntrans=2*floor((trans_ratio*nmax)/2); %First ring of "non-standard" rings
(rounded down to nearest EVEN integer)

%% Open the Gerber File for editing and write header/parameters applicable to the entire file
GerberFile=fopen('C:\Users\Chris\Desktop\tulip_zoneplate.gbr','w+');
fprintf(GerberFile,'G01*\r\n'); %Set Linear Interpolation Mode; \r for Notepad
viewing
fprintf(GerberFile,'%FSLAX35Y35*%\r\n'); %Set coordinate Format Specification to omit
Leading zeros, use Absolute notation, set number of integer positions in X,Y coordinates to 3 and decimal
positions to 5
fprintf(GerberFile,'%IPPOS*%\r\n'); %Set image polarity to "positive"
fprintf(GerberFile,'%LPD*%\r\n'); %Set layer polarity to "dark"
fprintf(GerberFile,'%MOMM*%\r\n'); %Set units to [mm]

tic;
%% Create each ring as a separate aperture
totarea=0; %Set initial covered area to 0
for j=1 ntrans-1 %Use normal ring calculations
until ntrans
rn=sqrt(2*j*lambda*f+(j^2)*(lambda^2)); %Ring radius (to CENTER of ring)
[m]
w=lambda*f/(2*rn); %Zone size [m]
d=2*rn+w; %Ring diameter (double the radius
plus half of the zone) [m]
totarea=totarea+(3.14*(rn+w/2)^2)-(3.14*(rn-w/2)^2); %Area of ring [m^2]
if j<2;
maxthick=w; %First ring is thickest
end
diam=1000*d; %Conversion (I don't really
understand why tis is the case mathematically, but it is correct when measured in the viewer)
thick=1000*w; %Conversion
fprintf(GerberFile,'%AMRING%d*\r\n',j); %These 2 lines define the Aperture
Macro
fprintf(GerberFile,'6,0,0,%0.5f,%0.5f,0,1,0,0,0*%\r\n',diam,thick);
end
for j=1 ntrans-1
apnum=j+9;
fprintf(GerberFile,'%ADD%DRING%d*%\r\n',apnum,j); %Define the aperture using the
created Macro
end

for j=ntrans:2 nmax %Second loop sets standard ring
thickness to 1.5 um and skips rings for radial spacing
rn=sqrt(2*j*lambda*f+(j^2)*(lambda^2));
w=minringsize;
d=2*rn+w;
if j<nmax;
secondtolast=rn+w/2; %Radial distance to outside of
second-to-last ring [m]
end

```

```

    last=rn-w/2; %Radial distance to inside of last
ring [m]
    totarea=totarea+3.14*(rn+w/2)^2-3.14*(rn-w/2)^2;
    diam=1000*d;
    thick=1000*w;
    fprintf(GerberFile,'% %AMRING%d*\r\n',j);
    fprintf(GerberFile,'6,0,0,%0.5f,%0.5f,0,1,0,0,0*%*\r\n',diam,thick);
end
for j=ntrans:2 nmax
    apnum=j+9;
    fprintf(GerberFile,'% %ADD%dRING%d*%*\r\n',apnum,j);
end

%% Position apertures (all centered)
for j=1 ntrans-1
    apnum=j+9;
    fprintf(GerberFile,'D%d*\r\n',apnum);
    fprintf(GerberFile,'X0Y0D03*\r\n');
end
for j=ntrans:2 nmax
    apnum=j+9;
    fprintf(GerberFile,'D%d*\r\n',apnum);
    fprintf(GerberFile,'X0Y0D03*\r\n');
end

%% Terminate and close Gerber File
fprintf(GerberFile,'M02*'); %End Gerber File
fclose(GerberFile);
toc;

%% Display useful information
ReadFile=fopen('C:\Users\Chris\Desktop\tulip_zoneplate.txt','w+');
fprintf(ReadFile,'Zone Plate Corrector Specifications\r\n');
fprintf(ReadFile,'Incident Wavelength: %.1f [nm]\r\n',lambda*1e9);
fprintf(ReadFile,'Focal Length: %.2f [m]\r\n',f);
fprintf(ReadFile,'Target Diameter: %.6f [m]\r\n',ptdiam);
fprintf(ReadFile,'Actual Diameter: %.6f [m]\r\n',d);
fprintf(ReadFile,'F Number: %.1f\r\n',fnumber);
fprintf(ReadFile,'Total Rings: %.1f\r\n',(nmax-ntrans)/2+ntrans);
fprintf(ReadFile,'Transition Ring: %.1f\r\n',ntrans);
fprintf(ReadFile,'Percent Covered by Normal Ring Size: %.2f%*\r\n',100*(ntrans-1)/((nmax-
ntrans)/2+ntrans));
fprintf(ReadFile,'Max Ring Thickness: %.2f [um]\r\n',maxthick*1e6);
fprintf(ReadFile,'Min Ring Thickness: %.2f [um]\r\n',w*1e6);
fprintf(ReadFile,'nmax Ring Separation: %.2f [um]\r\n',(last-secondtolast)*1e6);
fprintf(ReadFile,'Area Covered: %.2f%*\r\n',100*totarea/(3.14*(ptdiam/2)^2));
fprintf(ReadFile,'File Generation Time: %.2f [min]\r\n',toc/60);

```

Sample Gerber Format Photon Sieve Code

This section provides an example of text used by the printing company to produce a photon sieve. It illustrates proper Gerber specification in accordance with Ref. 18. The first block contains information relevant to the file as a whole. The second block provides an example of how to define an aperture (shape and size). In the third section, each defined aperture is placed at particular coordinates. In the last block, the file is closed.

```
G75*
%FSLAX35Y35*%
%IPPOS*%
%LPD*%
%MOMM*%
.
.
.
%ADD10C,0.10405*%
%ADD11C,0.07358*%
.
.
.
D10*
X10760Y-24984D03*
X19992Y-18448D03*
X25767Y-8721D03*
X27087Y2513D03*
X23723Y13313D03*
X16257Y21811D03*
X5980Y26537D03*
X-5331Y26676D03*
X-15720Y22201D03*
X-23391Y13888D03*
X-27017Y3174D03*
X-25972Y-8090D03*
X-20436Y-17954D03*
X-11367Y-24714D03*
X-332Y-27201D03*
D11*
X31926Y-21465D03*
```

X35593Y-14599D03*
 X37803Y-7136D03*
 X38466Y620D03*
 X37554Y8351D03*
 X35104Y15739D03*
 X31217Y22483D03*
 X26052Y28307D03*
 X19821Y32972D03*
 X12778Y36287D03*
 X5212Y38116D03*
 X-2568Y38385D03*
 X-10242Y37082D03*
 X-17497Y34262D03*
 X-24036Y30038D03*
 X-29590Y24585D03*
 X-33933Y18125D03*
 X-36887Y10923D03*
 X-38331Y3274D03*
 X-38206Y-4509D03*
 X-36516Y-12107D03*
 X-33331Y-19210D03*
 X-28782Y-25526D03*
 X-23055Y-30798D03*
 X-16383Y-34808D03*
 X-9041Y-37393D03*
 X-1329Y-38448D03*
 X6438Y-37928D03*
 X13941Y-35856D03*
 X20873Y-32316D03*
 X26951Y-27452D03*
 .
 .
 .
 M02*

Sample Gerber Format Zone Plate Code

This section provides an example of text used by the printing company to produce a FZP. It is the same as that for a photon sieve except for one additional step. Because Gerber does not have a predefined “ring” shape, the shape had to be constructed as an

“Aperture Macro” (AM) with specific dimensions. Once this was accomplished, the shape could be used to define an aperture and then place each one as before.

```
G01*
%FSLAX35Y35*%
%IPPOS*%
%LPD*%
%MOMM*%
.
.
.
%AMRING1*
6,0,0,0.41554,0.04617,0,1,0,0,0*%
%AMRING2*
6,0,0,0.55502,0.03265,0,1,0,0,0*%
%AMRING3*
6,0,0,0.66643,0.02666,0,1,0,0,0*%
.
.
.
%ADD10RING1*%
%ADD11RING2*%
%ADD12RING3*%
.
.
.
D10*
X0Y0D03*
D11*
X0Y0D03*
D12*
X0Y0D03*
.
.
.
M02*
```

Sample Zemax Photon Sieve Modeling Code

Fig. 47 provides an example of how to model a photon sieve in Zemax (2). It is adapted from the code created by the USAFA (8). Note that “Thickness” refers to the

distance from the selected point to the next, “Semi-Diameter” refers to the radius of the sieve, and “Pars 3” and “6” refer to the axial positions of the beams being interfered to create the hologram. See Eq. 41 and the accompanying text to understand the values employed. Additionally note that “Hologram 2” was used in this case. While it is not readily apparent from Ref. 39 why this is required, selection of this aperture type allowed the system to behave as desired to model the primary sieve. Note also that there are numerous general Zemax parameters that need to be set in addition to the design scheme.

Fig. 48 provides an example of how to model the complete system (primary and corrector) in Zemax (2). It is adapted from the code created by the USAFA (8). Note that “Hologram 1” was used for the corrector. Again, it is not readily apparent why this is required. It does, however, allow the desired system performance.

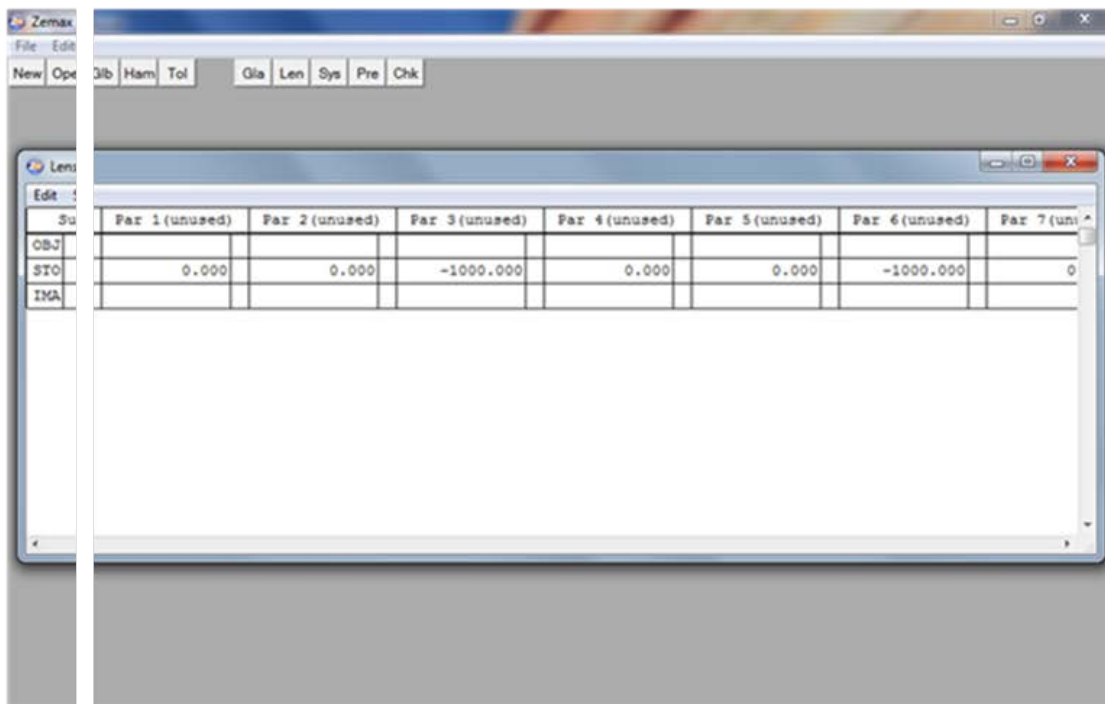
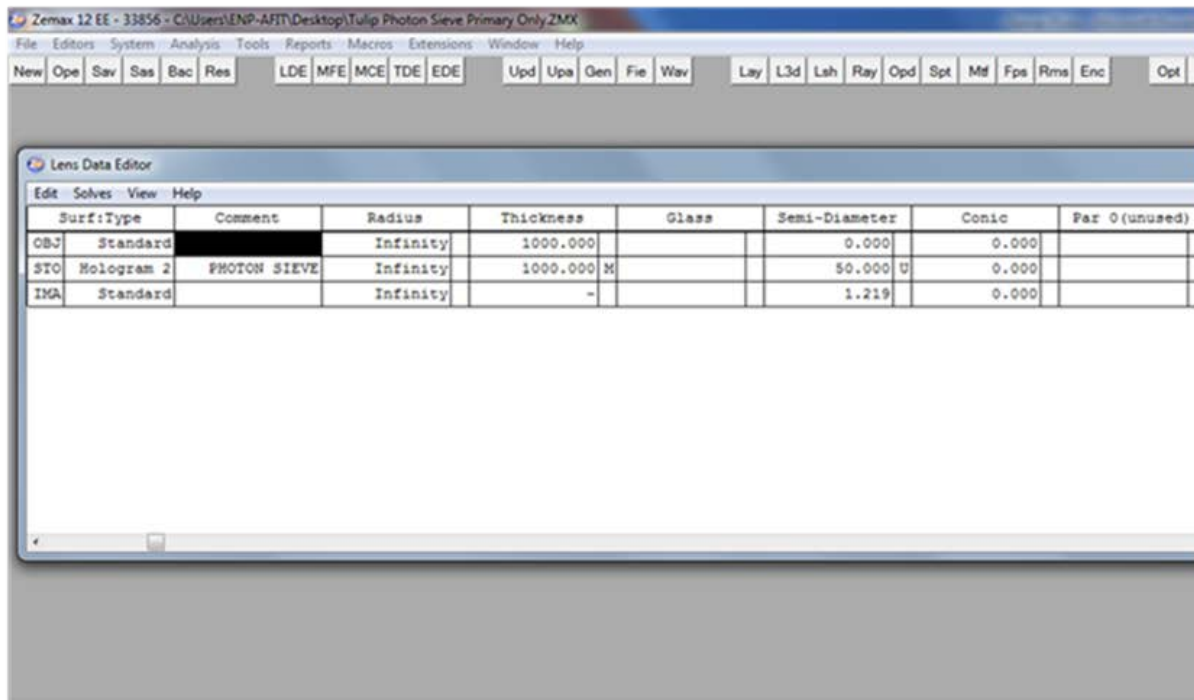


Figure 58. Zemax Photon Sieve Code

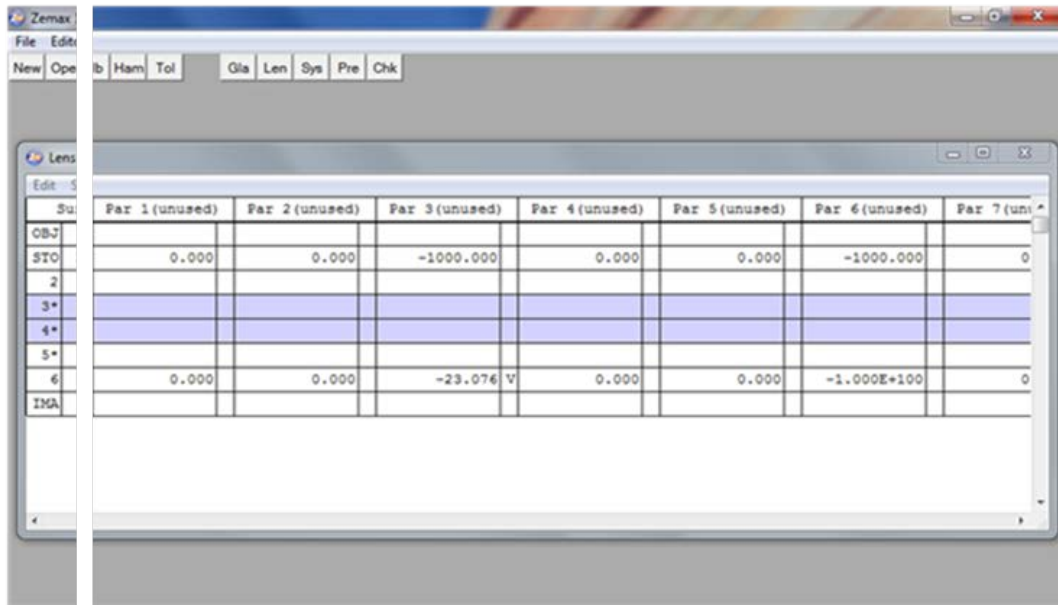
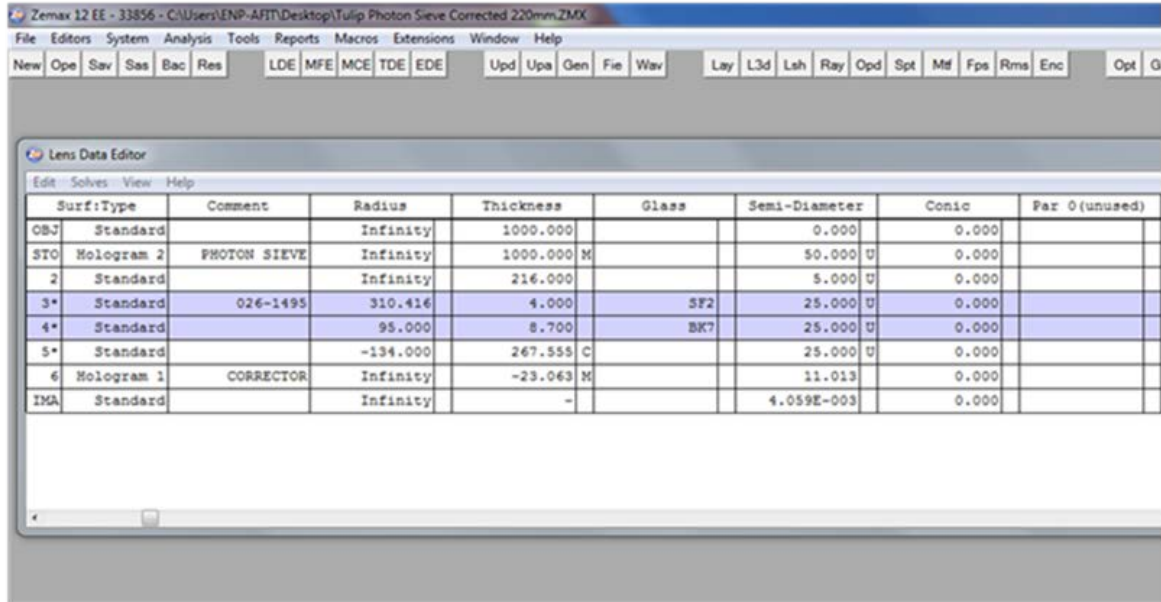


Figure 59. Zemax Corrected System Code.

ACA Error Propagation Analysis

Experimental techniques introduced error in the placement of the point source relative to the photon sieve ($\sigma_{s_0} = 5 \text{ mm}$) as well as in the measurement of the relative

image distance at each wavelength. ($\sigma_{\Delta} = 0.38$ mm). The analysis below covers the propagation of this uncertainty through the formula for determining ACA (Eq. A1).

$$ACA = \Delta f = f_{\lambda_2} - f_{\lambda_1} \quad (A1)$$

Note that f_{λ_1} is simply the design focal length of the primary sieve and is constant.

$$f_{\lambda_1} = f_{740nm} = f_{SIEVE} = f = 500.04 \text{ mm} \quad (A2)$$

Using the familiar imaging equation from geometric optics, f_{λ_2} and $s_{i\lambda_1}$ can be defined in terms of the other equation parameters.

$$\frac{1}{f} = \frac{1}{s_0} + \frac{1}{s_i} \Rightarrow \quad (A3)$$

$$f_{\lambda_2} = \frac{s_{i\lambda_2} s_{0\lambda_2}}{s_{i\lambda_2} + s_{0\lambda_2}} \quad (A3.1)$$

$$s_{i\lambda_1} = \frac{s_{0\lambda_1} f_{\lambda_1}}{s_{0\lambda_1} - f_{\lambda_1}} \quad (A3.2)$$

Δs_i is defined such that it is the difference between the image distance at a non-primary wavelength and the image distance at 740 nm.

$$\Delta s_i = \Delta = s_{i\lambda_2} - s_{i\lambda_1} \Rightarrow s_{i\lambda_2} = s_{i\lambda_1} + \Delta \quad (A4)$$

The object distance remained constant throughout the measurements.

$$s_{0\lambda_1} = s_{0\lambda_2} = s_0 \quad (A5)$$

Substitute Eq. A3.2 into Eq. A4, and then substitute Eq. A4 into Eq. A3.1. Make the notation changes suggested by Eqs. A2 and A5.

$$f_{\lambda_2} = \frac{s_0^2 \Delta - s_0 \Delta f + s_0^2 f}{s_0^2 + s_0 \Delta - \Delta f} \quad (\text{A6})$$

Substitute Eq. A6 into Eq. A1.

$$\text{ACA} = \frac{s_0^2 \Delta - s_0 \Delta f + s_0^2 f}{s_0^2 + s_0 \Delta - \Delta f} - f \quad (\text{A7})$$

The error in ACA is given by

$$\sigma_{\text{ACA}} = \sqrt{\left(\frac{\partial \text{ACA}}{\partial s_0}\right)^2 \sigma_{s_0}^2 + \left(\frac{\partial \text{ACA}}{\partial \Delta}\right)^2 \sigma_{\Delta}^2}. \quad (\text{A8})$$

Take the derivatives in Eq. A8. The algebra is not shown.

$$\frac{\partial \text{ACA}}{\partial s_0} = \frac{2s_0 \Delta - \Delta f + 2s_0 f}{s_0^2 + s_0 \Delta - \Delta f} - \frac{(2s_0 + \Delta)(s_0^2 \Delta - s_0 \Delta f + s_0^2 f)}{(s_0^2 + s_0 \Delta - \Delta f)^2} \quad (\text{A9})$$

$$\frac{\partial \text{ACA}}{\partial \Delta} = \frac{s_0^2 \Delta - s_0 f}{s_0^2 + s_0 \Delta - \Delta f} - \frac{(s_0 - f)(s_0^2 \Delta - s_0 \Delta f + s_0^2 f)}{(s_0^2 + s_0 \Delta - \Delta f)^2} \quad (\text{A10})$$

Set the object distance to approximately twice the focal length of the primary sieve.

$$s_0 \approx 2f \quad (\text{A11})$$

Substitute Eq. A11 into Eqs. A8 and A9 to arrive at the expressions below.

$$\frac{\partial \text{ACA}}{\partial s_0} = \frac{\Delta}{4f + \Delta} \quad (\text{A12})$$

$$\frac{\partial \text{ACA}}{\partial \Delta} = \frac{4f^2}{(4f + \Delta)^2} \quad (\text{A13})$$

Finally substitute Eqs. A12 and A13 into Eq. A8 along with the values for σ_{s_0} and σ_{Δ} to determine the total error in the calculation of ACA.

$$\begin{aligned}
\sigma_{\text{ACA}} &= \sqrt{\left(\frac{\Delta}{4f + \Delta}\right)^2 \sigma_{s_0}^2 + \left(\frac{4f^2}{(4f + \Delta)^2}\right)^2 \sigma_{\Delta}^2} \\
&= \sqrt{\left(\frac{\Delta}{2000.16 \text{ mm} + \Delta}\right)^2 25 \text{ mm}^2 + \left(\frac{10^6 \text{ mm}}{(2000.16 \text{ mm} + \Delta)^2}\right)^2 0.14 \text{ mm}^2}
\end{aligned} \tag{A14}$$

Bibliography

1. Andersen, Geoff. "Large optical photon sieve," *Optics Letters*, 30(22): 2976-2978 (November 2005).
2. Andersen, Geoff. Senior Researcher, Laser and Optics Research Center, United States Air Force Academy, Colorado Springs, CO. Personal Correspondence. 2014.
3. Andersen, Geoff. "Regular Photon Sieve." MATLAB Code. Laser and Optics Research Center, United States Air Force Academy, Colorado Springs, CO, 2014.
4. Andersen, Geoff and Drew Tullson. "Broadband antihole photon sieve telescope," *Applied Optics*, 46(18): 3706-3708 (June 2007).
5. Andersen, Geoff and Drew Tullson. "Photon Sieve Telescope," *Proceedings of SPIE*, 6265: 626523-1-8 (2006).
6. Andersen, G. and R.J. Knize. "Holographically Correct Telescope With Temporal Update," *Proceedings of SPIE*, 4013: 587-594 (2000).
7. Andersen, Geoff, Jesper Munch, and Peter Veitch. "Compact, holographic correction of aberrated telescopes," *Applied Optics*, 36(7): 1427-1432 (March 1997).
8. Andersen, Geoff and Olha Asmovlova. "Broadband Photon Sieve Telescope." Zemax Code. Laser and Optics Research Center, United States Air Force Academy, Colorado Springs, CO, 2014.
9. Andersen, Geoff and others. "FalconSAT-7: A Membrane Photon Sieve CubeSat Solar Telescope," *Proceedings of SPIE*, 8442: 84421C-1-8 (2012).
10. Cao, Qing and Jürgen Jahns. "Nonparaxial model for the focusing of high-numerical-aperture photon sieves," *Journal of the Optical Society of America*, 20(6): 1005-1012 (June 2003).
11. Cao, Qing and Jürgen Jahns. "Comprehensive focusing analysis of various Fresnel zone plates," *Journal of the Optical Society of America*, 21(4): 561-571 (April 2004).
12. Cao, Qing and Jürgen Jahns. "Focusing analysis of the pinhole photon sieve: individual far-field model," *Journal of the Optical Society of America*, 19(12): 2387-2393 (December 2002).
13. Cardoza, Joseph A. and Christopher M. Tulip. "Characterization of the index of refraction of a ZnSe lens from 720 nm to 850 nm using properties of Gaussian beam

- propagation.” OENG 651 Lab Report. Air Force Institute of Technology, Wright-Patterson AFB, OH, 2014.
14. Dereniak, E.L. and G.D. Boreman. *Infrared Detectors and Systems*. Hoboken, NJ: John Wiley & Sons, Inc., 1996.
 15. DiBartolomeo, Steve. “What’s all this about RS274X Anyway?” Artwork Conversion Software, Inc., Santa Cruz, CA, 1995
<http://www.artwork.com/gerber/274x/rs274x.htm>.
 16. Fischer, Robert E. and others. *Optical System Design* (2nd Edition). New York: The McGraw-Hill Companies, Inc., 2008.
 17. Franz, Anthony. Assistant Professor of Physics, Air Force Institute of Technology, Wright-Patterson AFB, OH. Personal Correspondence. 2014.
 18. The Gerber Format Specification. Revision J4. San Francisco: Ucamco, N.V., November 2014.
http://www.ucamco.com/files/downloads/file/81/the_gerber_file_format_specification.pdf?4dd989a3697b8f18bb468a999d4bdc9e.
 19. Goodman, Joseph W. *Introduction to Fourier Optics* (3rd Edition). Englewood, CO: Roberts and Company Publishers, 2005.
 20. Hariharan, P. *Optical Holography: Principles, Techniques, and Applications* (2nd Edition). New York: Cambridge University Press, 1996.
 21. Hecht, Eugene. *Optics* (4th Edition). San Francisco: Addison Wesley, 2002.
 22. Hufnagel, Robert E. (1985). *U.S. Patent No. 4,550,973*. Washington, DC: U.S. Patent and Trademark Office.
 23. Kipp, L. and others. “Sharper images by focusing soft X-rays with photon sieves,” *Nature*, 414:184-188 (November 2001).
 24. Lee, Wai-Hon. “Binary Synthetic Holograms,” *Applied Optics*, 13(7):1677-1682 (July 1974).
 25. Lee, Wai-Hon. “Binary computer-generated holograms,” *Applied Optics*, 18(21):3661-3669 (November 1979).
 26. Leith, Emmett N. and Juris Upatnieks. “Holograms: Their Properties and Uses,” *Optical Engineering*, 4(1): 3-6 (Nov 1965).

27. Munch, Jesper and Ralph Wuerker. "Holographic technique for correcting aberrations in a telescope," *Applied Optics*, 28(7): 1312-1317 (April 1989).
28. Munch, Jesper, Ralph Wuerker, and Lee Heflinger. "Wideband holographic correction of an aberrated telescope," *Applied Optics*, 29(16): 2440-2445 (June 1990).
29. Myers, Sarah J. *Design, Analysis, and Characterization of an Optical Photon Sieve for Space-Based Imaging Systems*. MS Thesis, AFIT-ENP-14-M-02. Graduate School of Engineering and Management, Air Force Institute of Technology (AU), Wright-Patterson AFB OH, March 2014.
30. O'Shea, Donald C. and others. *Diffraction Optics: Design, Fabrication, and Test*. Bellingham, WA: SPIE Press, 2004.
31. Space Physics and Atmospheric Research Center, U.S. Air Force Academy. "FalconSAT-7 Critical Design Review," 7 May 2013.
32. Space Physics and Atmospheric Research Center, U.S. Air Force Academy. "FalconSAT-7 Peregrine Payload Signal-to-Noise Analysis Systems Engineering Report," 17 Aug 2012.
33. "Spatial Filters." *Newport.com*. Retrieved 6 November 2014, from <http://www.newport.com/Spatial-Filters/144910/1033/content.aspx>.
34. Sussman, Milton. "Elementary Diffraction Theory of Zone Plates," *American Journal of Physics*, 28: 394-398 (1960).
35. "T-20 USAF 1951 Chart Standard Layout Product Specifications, Version 1-04," New York: Applied Image, Inc., no date. http://www.aig-imaging.com/mm5/PDF/USAF%201951%20Test%20Target%20T-20_v1-04.pdf.
36. Upatnieks, J., A. Vander Lugt, and E. Leith. "Correction of Lens Aberrations by Means of Holograms," *Applied Optics*, 5(4): 589-594 (April 1966).
37. Verdeyen, Joseph T. *Laser Electronics* (3rd Edition). Upper Saddle River, NJ: Prentice Hall, Inc., 1995.
38. "Write data to text file – MATLAB fprintf." *Mathworks.com*. Retrieved 30 July 2014, from <http://www.mathworks.com/help/matlab/ref/fprintf.html>.
39. Zemax, *Optical Design Program, User's Guide*. Version 10.0. Tucson, AZ: Focus Software, Inc., April 2001.
40. Zhang, Xiaojie, Xu Liu, and Xiaoxi Chen. "Computer-generated holograms for 3D objects using the Fresnel zone plate," *Proceedings of SPIE*, 5636: 109-115 (2005).

REPORT DOCUMENTATION PAGE				Form Approved OMB No. 074-0188	
<p>The public reporting burden for this collection of information is estimated to average 1 hour per response, including the time for reviewing instructions, searching existing data sources, gathering and maintaining the data needed, and completing and reviewing the collection of information. Send comments regarding this burden estimate or any other aspect of the collection of information, including suggestions for reducing this burden to Department of Defense, Washington Headquarters Services, Directorate for Information Operations and Reports (0704-0188), 1215 Jefferson Davis Highway, Suite 1204, Arlington, VA 22202-4302. Respondents should be aware that notwithstanding any other provision of law, no person shall be subject to a penalty for failing to comply with a collection of information if it does not display a currently valid OMB control number.</p> <p>PLEASE DO NOT RETURN YOUR FORM TO THE ABOVE ADDRESS.</p>					
1. REPORT DATE (DD-MM-YYYY) 26-03-2015		2. REPORT TYPE Master's Thesis		3. DATES COVERED (From - To) October 2013 - March 2015	
TITLE AND SUBTITLE Bandwidth Broadening by Reduction of Chromatic Aberration Effects Using Second-Stage Diffractive Optics				5a. CONTRACT NUMBER	
				5b. GRANT NUMBER	
				5c. PROGRAM ELEMENT NUMBER	
6. AUTHOR(S) Tulip, Christopher M., Major, USAF				5d. PROJECT NUMBER	
				5e. TASK NUMBER	
				5f. WORK UNIT NUMBER	
7. PERFORMING ORGANIZATION NAMES(S) AND ADDRESS(S) Air Force Institute of Technology Graduate School of Engineering and Management (AFIT/EN) 2950 Hobson Way WPAFB OH 45433				8. PERFORMING ORGANIZATION REPORT NUMBER AFIT-ENP-MS-15-M-086	
9. SPONSORING/MONITORING AGENCY NAME(S) AND ADDRESS(ES) United States Air Force Academy Space Physics and Atmospheric Research Center 2354 Fairchild Drive, Suite 2A31, USAF Academy, CO 80840 719-333-2460 / matthew mcharg@usafa.edu ATTN: Dr. Matthew G. McHarg				10. SPONSOR/MONITOR'S ACRONYM(S) USAF/DFP	
				11. SPONSOR/MONITOR'S REPORT NUMBER(S)	
12. DISTRIBUTION/AVAILABILITY STATEMENT DISTRIBUTION STATEMENT A. APPROVED FOR PUBLIC RELEASE; DISTRIBUTION UNLIMITED.					
13. SUPPLEMENTARY NOTES This material is declared a work of the U.S. Government and is not subject to copyright protection in the United States.					
14. ABSTRACT A photon sieve is a lightweight diffractive optic which can be useful for space-based imaging applications. It is limited by chromatic aberration and a narrow bandwidth. A Fresnel zone plate is used to counteract this effect in a manner similar to that accomplished with a traditional holographic corrector. First, a radiometric analysis established a target for bandwidth improvement. Next, a sieve was designed, fabricated, and characterized. Third, the bandwidth-broadening correction scheme was developed to correct primary chromatic aberration. Finally, a zone plate was designed, fabricated, and tested. Performance of the corrected system was measured over the target bandwidth. The corrected system resolved the "3-1" group of a resolution target at the primary wavelength and across an 8-nm bandwidth. The uncorrected system resolved the smaller "6-5" group at the primary wavelength but resolved the "3-1" group over only a 2-nm range. The lower resolution of the corrected system at the primary wavelength is suspected to be a result of corrector design flaws which allowed only the central 2-4 mm to be used. When accounting for this reduced diameter, resolving the "3-1" group does indicate nearly diffraction-limited performance over a bandwidth four times greater than the uncorrected system at the same resolution. This result suggests correction is occurring. A redesign of the corrector may increase performance.					
15. SUBJECT TERMS Chromatic Aberration, Photon Sieve, Fresnel Zone Plate, Holographic Correction, Diffractive Optic Elements					
16. SECURITY CLASSIFICATION OF:			17. LIMITATION OF ABSTRACT	18. NUMBER OF PAGES	19a. NAME OF RESPONSIBLE PERSON
a. REPORT	b. ABSTRACT	c. THIS PAGE			Anthony L. Franz, Lt Col, AFIT/ENP
U	U	U	UU	136	19b. TELEPHONE NUMBER (Include area code) (937) 255-6565, ext 4429 anthony.franz@afit.edu